Terahertz scanning tunneling microscopy of metal and superconductor surfaces

by

Howe Simpson

A thesis submitted in partial fulfillment of the requirements for the degree of

Master of Science

Department of Physics
University of Alberta

Abstract

The advent of the terahertz scanning tunneling microscope (THz-STM) brings with it a new method of observing and characterizing the ultrafast dynamics of materials. The sub-nanometer spatial resolution of an ultra-high vacuum scanning tunneling microscope (UHV-STM) coupled with the sub-picosecond time resolution from a terahertz (THz) pulse allows for ultrafast measurements of surface dynamics across varying surface features down to the atomic scale. This thesis explores STM and THz-STM of metal and superconductor surfaces.

High critical temperature superconductivity has been an area of interest since its discovery. $Bi_2Sr_2CaCu_2O_8$ is an excellent candidate to study the superconductive process due to its high critical temperature of 95 K and ease of cleaving. STM and scanning tunneling spectroscopy measurements on the high-temperature superconductor $Bi_2Sr_2CaCu_2O_8$ are performed at 100 K and 55 K.

STM and STS measurements were also performed on the surface of flat Au(111). Given gold's versatility as a substrate for many STM measurements, it is important to ensure that the STM system used in this study can replicate results that coincide with many other studies done on the surface of gold. The characteristics of the substrate such as flatness and cleanliness prior to deposition of other materials were investigated. The herringbone surface reconstruction of Au(111) was imaged and the topography was analysed with good agreement compared to other studies.

Finally, optical-pump/THz-STM-probe measurements are performed on a silver-coated gold surface. These measurements, with tip-sample distances outside of the typical tunneling regime of the THz-STM, use photo-excited electrons from an optical

pump beam to tunnel between the sample and tip. A THz pulse is then focused onto the junction between the sample and tip. The results show an interesting behaviour in the regime where the pump beam is not focused on the junction but elsewhere on the surface of the sample. These preliminary results may help gain a better understanding of the photoemission-based THz waveform measurements, as well as demonstrate a new use of the THz-STM for propagation dynamics of surface excitations.

Preface

This thesis is an original work by Howe Simpson. No part of this thesis has been previously published. The work performed for this thesis was completed between September 2019 to August 2021 under the supervision of Professor Frank A. Hegmann.

Results from chapter 5 were taken with the assistance of J. A. M. Calzada, Y. Luo, and N. B. Refvik. Results from chapter 7 were taken with the assistance of N. B. Refvik.

Dedicated to my grandfather, George Emery, for there was no end to his curiosity.

Acknowledgements

I would like to begin by thanking my supervisor, Dr. Frank Hegmann, for giving me the opportunity to be a part of the team in the ultrafast nanotools lab. His extensive knowledge of physics and approachability were strong assets for me to continue in my studies. The experiences I've had in and out of the lab are all memorable.

I'd also like to thank Yang Luo for teaching me the ways of the THz-STM, and for being very patient with my many questions about the system. A big thank you to Alex Marin for helping me with STM measurements, STM questions, revising my thesis, and always offering a helping hand in and out of the lab. A big shout-out to the other members of the lab: David Purschke for his brilliance in physics, help with general problems, and for being a great roommate; Cameron Hough for his insights into THz pulses and sense of humour; Peter Nguyen for good conversations about THz-STM modelling and sports; Charles Jensen who was always available to help with data analasis, and a good laugh; and Nils Refvik for helping me on the long days of data collection and the longer days the STM wasn't cooperating. And to Christina Strilets, a summer coop student, for operating the ambient STM while I worked with the UHV system, and for teaching me that science doesn't need to be just a black and white powerpoint presentation.

A big acknowledgement to the technical expertise of Greg Popowich and James Chaulk. If not for them, the STM system would probably still be out of order to this day.

Finally, I'd like to thank my finacée Jess and my stepson Evvy for being patient with me on those long nights of data collection, and for staying by me even at my

worst. I owe you both so much. To my mom and brother, for their immense support in and out of school. I'd also like to thank all of my friends back home in Ottawa and at my other home in Halifax who have continued to support me on my choice to continue in school. To the friends I've made all across the world, who pushed me forward and supported me in Spirit. Thank you all!

Table of Contents

List of Tables

List of Figures

Chapter 1

Introduction

The excitement of observing the smallest of objects has been an area of interest for scientists and the general public for centuries. Beginning with the use of polished lenses for eye correction, the idea was extended into the first reported microscope in the late seventeenth century [1]. Since then, microscopy has advanced far beyond the use of light and lenses for imaging. The first transmission electron microscope (TEM), created by Ernst Ruska and Max Knoll in 1931, used electrons and magnetic fields instead of light and lenses for magnification [2]. Soon after in 1936, Erwin Müller demonstrated nanoscale images due to high electric fields and emission of electrons from a sharp tip with his field electron emission microscope [3, 4]. Finally, in 1951 with the creation of the field ion microscope, Müller was able to attain atomic resolution [4, 5].

Near-field nanoscopy began with the invention of scanning near field microscopy (SNOM) in 1972 by E. A. Ash and G. Nicholls [6]. Using a probe, SNOM achieves nanoscale resolution by measuring the intensity of the evanescent field caused by an optical pulse. This bypassed the diffraction limit for the resolution of optical microscopes given the resolution is dependent on the size of the probe and not the wavelength of the optical beam. The idea of using a probe to help in the resolution of nanoscale features on a surface continued with the introduction of the scanning tunneling microscope (STM) in 1982 by Binnig and Roher [7, 8], which proved to be an

invaluable tool in surface science and for which they received the Nobel prize in physics in 1986. The STM proved versatile in its ability to atomically resolve the surface of conductive materials and to explore the energy dependence of the surface properties by varying the bias (potential difference) at the junction. A particular example of the new opportunities that the STM presented was when Binnig et. al. resolved the reconstructed surface of Si(111) in real-space, helping to end many debates on the nature of the reconstructed Si surface [9]. The STM has been adopted worldwide and has been used to probe a variety of materials including metals [10–12], semiconductors [13–15], superconductors [16–18], and even biological systems [19–21].

With the sub-nanometer scale spatial resolution of the STM established, researchers began looking at ways to simultaneously resolve transient dynamics on material surfaces. Typically, an ultrafast laser pulse is used to excite carriers in a system. This excitation is resolved over the duration of the incident pulse, allowing for a temporal map of the excitation dynamics. The first proof-of-concept of optically illuminated STM was performed by van de Walle et al., where they simultaneously illuminated and scanned the surface of GaAs [22]. In order to achieve picosecond time resolution with an STM, Weiss et al. used ultrafast pulses coupled to a photoconductive switch which allowed for 2 ps time resolution and a 5 nm spatial resolution [23]. One of the prevailing issues with these photoassisted measurements is the thermal expansion of the tip due to the energy of the optical pulse [24].

Currently, different methods exist to work around this issue that use varying optical frequencies which are summarized in Table 1.1. These different methods probe different dynamics of the surface. Synchrotron enhanced x-ray STM (SX-STM) measures the chemical contrast of a surface using nanofabricated tips [25, 26]. The fabricated tips are created from an insulator wrapped with a conducting shell to offset electrons being photoexcited and coupling to the tunneling current [25, 26]. Light-Modulated scanning tunneling spectrscopy (LM-STS) uses a chopped, low-power near-UV beam to avoid thermal effects to probe photogenerated surface carriers [27]. Single-molecule

absorption STM (SMA-STM) uses Kretschmann-Raether geometry with a laser in the visible spectrum to avoid thermal expansion effects, and looks at carrier absorption effects [28]. Shaken-pulse-pair-excited STM (SPPX-STM) uses four laser pulses to modulate the delay time of a pump-probe beam, avoiding thermal modulation of the tip of the STM and observing carrier decay much like a pump-probe experiment [29, 30].

The first picosecond resolution in an STM was reported by G. Nunes Jr. and M. R. Freeman in 1993 using junction mixing [32], which uses two photoconductive switched (GaAs) to modulate the voltage of the tip-sample junction on the picosecond timescale, leading to a modulation in the tunneling current that demonstrated time resolution of 10 ps with nm spatial resolution.

Terahertz STM (THz-STM) uses free-space THz pulses to couple to the STM tip. The first THz-STM scan showed the nanoscale spatial resolution and sub-picosecond surface dynamics of an InAs nanodot [35]. The tip-heating effects are negligible in this system given the low-energy of the THz photon (4.14 meV at 1 THz). One of the exciting prospects of THz-STM is that the STM system itself hardly needs to be modified given the free-space THz pulse coupling to the STM tip. THz generation is also simple given advancements in THz generation technology. Since its inception, the THz-STM has been used to image the surface reconstruction of Si(111)-(7x7), bypassing the surface screening effects of silicon and reporting a difference in the THz induced tunnel conductance from normal STM [38], observe the effects of surface edges and defects on the motion and lifetimes of photoexcited electrons [39], image and model scans of metal surfaces across step edges and defects [40], and observe phase-resolution of THz pulses coupled to the tip in order to demonstrate the possibility of spintronic measurements on material surfaces [37].

The THz waveform measured from the current response in the STM junction due to the THz electric field is still under investigation. Looking at the antenna response of the STM tip with the current modulation from photoexcited carriers both in and

PG-STM	Phoconductively-Gated STM: First picosecond time resolution using laser pulses and a photoconductive switch. Requires specialized tips and transmission lines on the sample. Limited due to capacitive coupling. [23, 31]
JM-STM	Junction-Mixing STM: First picosecond time resolution with simultaneous nanometer resolution. Requires the creation of transmission lines on the sample. [32–34]
SX-STM	Synchotron X-ray STM: Uses X-rays to observe the chemical contrast of a sample. Requires nanofabricated tips to avoid tip heating effects. [25, 26]
LM-STM	Laser-Modulated STM: Uses low power chopped laser to illuminate the sample and measure spatially resolved surface photovoltage. The measurement is highly dependent on the bias voltage, especially at low biases. [27]
SMA-STM	Single-Molecule Absorption STM: Uses a modulated laser to excite the sample to image optical absorption. Requires a Kretschmann light-coupling geometry, restricting the types of substrates used in the technique. [28]
SPPX-STM	Shaken-Pulse-Pair-Excited STM: Uses paired laser pulses with a modulated delay time to observe carrier trapping. Careful consideration of the delay time is required to avoid an artifact signal in the decay time measurements. [29, 30]
THz-STM	Terahertz STM: Uses THz pulses coupled to the tip to modulate the tunnel current in order to measure ultrafast dynamics of materials. The shape of the near-field THz-waveform is still under investigation. [35–37]

Table 1.1: Summary of optical STM techniques with experimental considerations.

outside the tunneling regime can be attributed to many different causes such as tip shape, tip and sample material, and field strength [36, 37, 41]. Modeling these THz effects in the tunneling junction has been attempted using RLC circuit models, and use a superposition of the incoming THz pulse with surface propagating waves and scattered fields [37, 41–43].

This thesis will begin by presenting a theoretical introduction to STM including models of the tunneling current and theory of scanning tunneling spectroscopy in chapter 2. An overview of THz generation and detection as well as a basic overview of THz pulse coupling to an STM tip and a review of recent THz-STM experiments are presented in chapter 3. Chapter 4 will summarize the ultra-high vacuum STM system used in the experiments presented in this thesis, including STM tip preparation. STM of the high-T_C superconductor Bi-2212 is presented in chapter 5 with some preliminary results of THz-STM on the surface at 100 K. The Au(111) surface herringbone reconstruction is explored in chapter 6 given its prevalence as a substrate for many STM experiments. Scanning tunneling spectroscopy done on the surface of Au(111) is also performed and compared to previously reported results. Finally, chapter 7 will discuss Ag(111) deposited on Au(111). The surface features are compared to the typical structure of thin Ag(111). Photoemission assisted optical-pump-THz-probe results were taken with interesting results from different optical pump positions on the surface.

Chapter 2

Principles of STM

2.1 Electron Tunneling

The basic theory of operation of the scanning tunneling microscope (STM) is the quantum tunneling of electrons. Classically, a particle cannot penetrate a barrier if the energy of the particle is lower than the height of the barrier. However, quantum mechanics shows that a particle also behaves as a wave. This wave-like behaviour allows a particle with an energy lower than that of the potential barrier will have a non-zero probability of tunneling through the barrier (Fig. 2.1). In the framework of an STM system, a potential barrier exists in the vacuum (or air) gap between a metallic tip and conducting sample, with electrons being the tunneling particles.

An intuitive picture of tunneling can be obtained from a one-dimensional model. Taking an electron of energy E onset to a static one-dimensional potential barrier of width z and energy $U(x)$, and using the time-independent Schrödinger equation, a solution can be found for the wave function of the electron at position x, $\psi(x)$:

$$\frac{-\hbar^2}{2m}\frac{d\psi(x)}{dx} + U(x)\psi(x) = E\psi(x), \tag{2.1}$$

with m the mass of the electron. While within the barrier where $U(x) \neq 0$, the solution $\psi(x)$ is:

$$\psi(x) = Ce^{\pm\kappa x}, \tag{2.2}$$

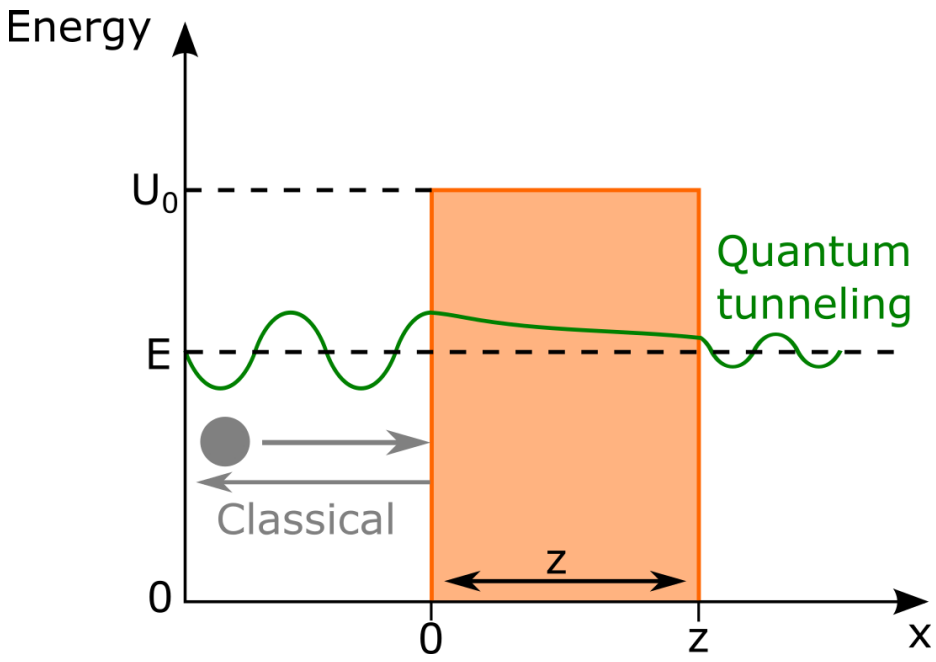

Figure 2.1: One dimensional energy barrier with barrier height energy, U_0, and barrier width, z, with an electron energy of E. Classically, the electron's energy is insufficient to surpass the barrier energy and will simply return along its path (grey arrow). A quantum mechanical treatment gives a non-zero probability of electron transmission through the barrier (green arrow).

with $\kappa = (\sqrt{2m}/\hbar)\sqrt{U(x) - E}$. For a constant barrier height $U(x) = U_0$, one can algebraically solve for the transmission coefficient of the incident electron. However, for arbitrary $U(x)$, the Wentzel-Kramers-Brillouin (WKB) method can be used to approximate the solution. Looking at the wave function at the edge of the barrier $x = z$ and using the WKB approximation the solution becomes:

$$\psi(x = z) = \psi(x = 0) \exp\left[\int_0^z -\frac{\sqrt{2m}}{\hbar}\sqrt{U(x) - E}\, dx\right]. \tag{2.3}$$

The wave function of the electron at $x = z$ is dependent on the initial conditions of the electron at the start of the barrier, $\psi(x = 0)$. While the energy of the electron E is less than the energy of the barrier, $U(x)$, and the transmission factor T is the square of the ratio of the wave functions before and after the tunneling event, then

$$T(E) = \left|\frac{\psi(z)}{\psi(0)}\right|^2 = \exp\left[-\frac{2\sqrt{2m}}{\hbar}\int_0^z \sqrt{U(x) - E}\, dx\right]. \tag{2.4}$$

If the barrier energy is constant over the tunneling distance with $U(x) = U_0$, then the transmission factor simply becomes

$$T(E) = \exp\left[-\frac{2\sqrt{2m}}{\hbar}\sqrt{U_0 - E}\, z\right]. \tag{2.5}$$

Of particular importance is the exponential relationship. The transmission coefficient exponentially decays with an increasing the barrier length, meaning a small change in the length allows for a large change in the transmission coefficient. For an STM, the distance between the tip and the surface of a sample is the barrier length, z. The higher the transmission coefficient, the more electrons will tunnel between the sample and tip, and an increase in current is observed. Given the ≈ 1 nm distance between the sample and tip, a small change in the distance will lead to a readable change in the current. This model also assumes a single point between the tip and sample. Thus, the end of the STM tip has to be as atomically sharp to enable the change in current to be localised to single atoms on the surface.

2.2 Simmons and Bardeen STM Models

Typically, the transmission coefficient of an electron tunneling between a tip and a sample relies on more variables than just the energy of the electron and the potential barrier height. The energy required to eject an electron from the surface of a material, the work function (ϕ), plays an important role in the value of the potential barrier height. Also, a voltage bias (V) introduced by the STM will shift the highest energy level allowed by the material being biased. Assuming the tip is grounded and the sample is biased, the bias voltage will decrease or increase the energy of states of the sample based on a positive bias (electrons are 'injected' into the sample surface from the tip) or negative bias (electrons are 'pulled' from the sample to the tip), respectively (Fig. 2.2).

John G. Simmons arrived at a generalized formula for tunneling between two sim-

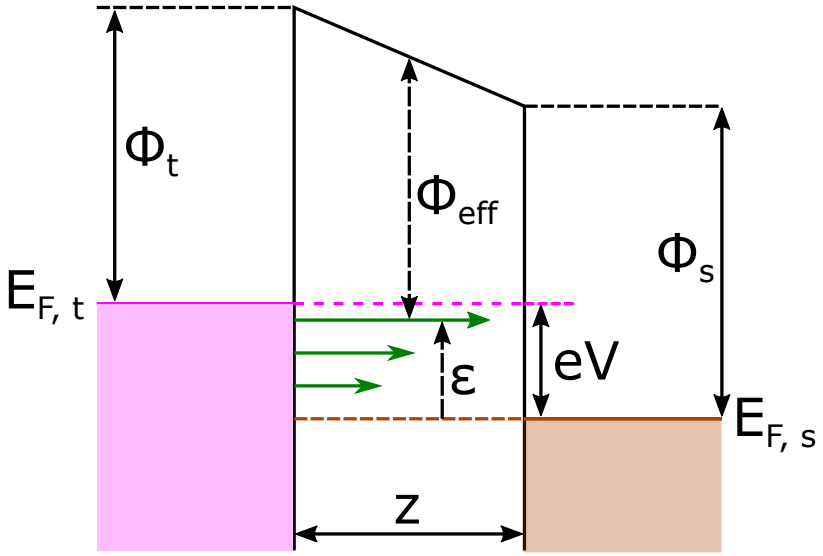

Figure 2.2: Diagram of the tunneling barrier of width z for a metal-vacuum-metal junction. In the STM, the tip, t, and the sample, s, are separated by a vacuum or air. The Fermi energy of the sample, $E_{F,s}$ is shifted due to a positive bias voltage, V. The tip Fermi energy, $E_{F,s}$, does not change from the bias. (Adapted from [44].)

ilar materials through an arbitrarily shaped potential barrier before the invention of the STM [45, 46]. Using the WKB approximation solution from equation 2.5 and replacing $U(x)$ with an approximate form of the barrier height as $\phi(x) + E_{F,t}$, where $E_{F,t}$ is the Fermi energy of the tip and $\phi(x)$ is the energy between the maximum energy of the potential barrier at position x and $E_{F,t}$, the solution now becomes

$$T(\epsilon) = \exp\left[-\frac{2\sqrt{2m}}{\hbar}\int_0^z \sqrt{\phi(x) + E_{F,t} - \epsilon}\, dx\right], \tag{2.6}$$

with ϵ the energy of the tunneling electron with respect to the Fermi energy of the sample, $E_{F,s}$. To perform the integral, the actual barrier height is replaced with an average barrier height, defined as $\overline{\phi} = \frac{1}{z}\int_0^z \phi(x)dx$. This gives as an approximate solution:

$$T(\epsilon) \approx \exp\left[-\alpha\sqrt{\overline{\phi} + E_{F,t} - \epsilon}\right], \tag{2.7}$$

with $\alpha = 2\sqrt{2m}\beta z/\hbar$ the collection of constants, and β a correction factor arising from the integration whose value is near unity. For non-zero temperatures, Simmons

defined the tunnel current using Fermi-Dirac distribution functions for each direction of the flowing electron (be it $f(E)$ flowing from tip-sample or $f(E+eV)$ flowing sample-tip) the potential barrier and the transmission coefficient:

$$I(\epsilon) = \frac{me}{2\pi^2\hbar^3}\int_0^{E_{max}} T(\epsilon)d\epsilon \times \int_0^{\infty}[f(E) - f(E+eV)]dE, \tag{2.8}$$

where E_{max} is the maximum electron energy tunneling through the barrier. The integral $\int_0^{\infty}[f(E) - f(E+eV)]dE$ has three possible solutions dependant on the electron energy ϵ given $f(E) - f(E+eV)$ denotes the range of possible tunneling energies of the electron as shown in Fig. 2.3. First, if the electron energy is between

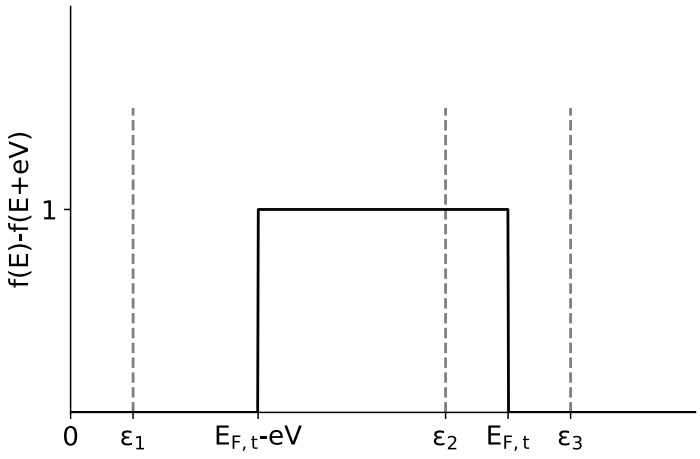

Figure 2.3: Solution of the distribution of possible electron tunneling energies $f(E) - f(E+eV)$. The step function begins at $E_{F,t} - eV$ and ends at $E_{F,t}$, with a width of eV. Shown are three possible electron tunneling energies that will separate the integral of Eq. 2.8.

zero and the Fermi energy of the tip $E_{F,t}$ minus the bias energy eV (ϵ_1), the total energy given by the integral will be eV. If the electron energy lies between eV and $E_{F,t}$ (ϵ_2) the total energy will simply be $E_{F,t} - \epsilon$. Finally, if the electron energy lies above $E_{F,t}$ (ϵ_3) then the integral is zero. Thus, the integral from equation 2.8 can be split into two regions:

$$I(\epsilon) = \frac{me}{2\pi^2\hbar^3}\left(eV\int_0^{E_{F,t}-eV}\exp\left[-\alpha\sqrt{E_{F,t}+\overline{\phi}-\epsilon}\right]d\epsilon + \int_{E_{F,t}-eV}^{E_{F,t}}(E_{F,t}-\epsilon)\exp\left[-\alpha\sqrt{E_{F,t}+\overline{\phi}-\epsilon}\right]d\epsilon\right). \tag{2.9}$$

With the assumption that $\alpha\sqrt{\overline{\phi}+eV} >> 1$, and recognizing after the expansion of the integrals that some terms are negligible, Simmons derived the final solution for the tunnel current as:

$$I(\epsilon) = \frac{e}{4\pi^2\hbar(\beta z)^2}\left[\overline{\phi}\exp(-\alpha\sqrt{\overline{\phi}}) - (\overline{\phi}+eV)\exp(-\alpha\sqrt{\overline{\phi}+eV})\right]. \tag{2.10}$$

The first term of the current equation is the current travelling from the tip to the sample, while the second term is for the opposite direction. This net current is zero with no bias V given the electronic states of the sample and tip are at equilibrium, an expected result for STM.

While the Simmons model assumes a constant density of states on both edges of the potential barrier, Bardeen in 1960 (once more, before the advent of the STM) developed a model for tunneling based on treating the two edges of the barrier as separate; each with their own set of electron eigenstates of energies [47]. The Bardeen model has been used to model tunnel currents in the STM since 1983 [48–51], and continues to be a valid model today. Beginning with a one-dimensional barrier model, the transition matrix element from an initial energy of the tip, $E_{t,i}$ and a final energy state of the sample, $E_{s,f}$, through a one dimensional rectangular potential barrier is

$$M(E) = \frac{\hbar^2}{2m}\int_{x=x_s}\left[\psi_t(x,E)\frac{\partial\psi_s^*(x,E)}{\partial x} - \psi_s^*(x,E)\frac{\partial\phi_t(x,E)}{\partial x}\right]dS, \tag{2.11}$$

where x_s is some height above the sample surface and S is the tip-sample separation surface. Using x_s instead of the full barrier length z considers the two edges of the potential barrier separately. Also, only elastic tunneling is considered, giving $E_{t,i} = E_{s,f} = \epsilon$. Considering the solutions of the electron wave form at the tip and

sample, $\psi_t(x) = \psi_t(0) \exp -\kappa x$ and $\psi_s(x) = \psi_s(z) \exp \kappa(x - z)$, and inserting it into Eq. 2.11 gives:

$$\begin{aligned} M(\epsilon) &= \frac{\hbar^2}{2m} \int_{x=x_s} 2\kappa \psi_{t,i}(0) \psi_{s,f}(z) e^{-\kappa x_s} e^{\kappa(x_s - d)} dS, \\ M(\epsilon) &= \frac{\hbar^2 \kappa}{2m} \psi_{t,i}(0) \psi_{s,f}(z) A e^{-\kappa z}, \end{aligned} \tag{2.12}$$

where A is the area of contact between the tip and sample. Looking at the one-dimensional rectangular approximation where $U(x) = U_0$, we know from Fermi's Golden Rule that the transmission probability P between an initial state i and a final state f is proportional to the transmission matrix element squared:

$$P_{if} = \frac{2\pi}{\hbar} |M|^2 \delta(\epsilon_f - \epsilon_i). \tag{2.13}$$

Inserting equation 2.12 into Fermi's golden rule, and acknowledging that the energy dependence in the exponent will dominate the value of the probability factor (or $x^2 < e^{2x}$ for $x > 0$):

$$T(\epsilon, z) \propto \exp \left[- \frac{2\sqrt{2m}}{\hbar} \sqrt{U_0 - \epsilon}\, z \right]. \tag{2.14}$$

This is comparable to both equation 2.5 and equation 2.7 for the transmission probability. If a trapezoidal well is considered rather than a rectangular well, and making the assumption that the barrier distance, z, is sufficiently small (as is the case for an STM system), the barrier height $U_0 - E$ can instead be replaced with an effective barrier height dependent on the bias voltage and electron energy approximated by a rectangular barrier:

$$\phi_{eff}(\phi_t, \phi_s, V, \epsilon) = \frac{\phi_t + \phi_s}{2} + \frac{eV}{2} - \epsilon, \tag{2.15}$$

leading to a transmission coefficient now dependent on the bias, V, the energy of the electron, ϵ, and the tip-sample distance, z, as:

$$T(\epsilon, V, z) \propto \exp\left[-\frac{2\sqrt{2m}}{\hbar}\sqrt{\phi_{eff}}\, z\right]. \tag{2.16}$$

To determine the current that arises from the tunneling electron, an integral is formed over both the density of states of the tip, ρ_t, and of the sample, ρ_s along with the probability factor $T(\epsilon, V, z)$ over all possible electron energies:

$$I(\epsilon, V, z) = \frac{4\pi e}{\hbar}\int_{E_{F,s}}^{E_{F,t}} \rho_t(\epsilon - (E_{F,t} - E_{F,s}))\rho_s(\epsilon)T(\epsilon, V, z)d\epsilon. \tag{2.17}$$

All of these models lead to the same result about the current-position relationship: the current measured from a biased tunneling system related to the exponential of the effective barrier height, the tip-sample distance, and the voltage bias. These conclusions agree with the measurable signal when a current/distance change is measured. Thus, the STM can be run in both constant height mode where the current is measured as a function of changes in the height, or constant current mode where the height is measured as a function of a change in current. A feedback loop is used to keep the current constant while taking a scan. Thus, if there is a change in the current while scanning a surface, the feedback loop will cause a shift in the tip height.

2.3 Image Potential

Given the small distances between the tip and sample, it is important to consider the effects of a charge approaching a conducting plane, also defined as an image charge. In this case, a classical treatment can be achieved to explain the multiple image potentials (from the tip and the surface). Simmons arrived at a solution to this using a classical description [46]:

$$\phi_i = \left(-\frac{e^2}{4\pi\epsilon}\right)\left[\frac{1}{2z} + \sum_{n=1}^{\infty}\left(\frac{nx}{[(nx)^2 - z^2]} - \frac{1}{nx}\right)\right], \tag{2.18}$$

where ϕ_i is the image potential, z is the tunnel length, and x is the distance of the electron from the tip as it tunnels through the potential barrier. This equation can

be approximated using a parabola, where

$$\phi_i = -\frac{1.15e^2 \ln(2)}{8\pi\epsilon x}\frac{x^2}{z(x-z)}. \tag{2.19}$$

This shows a reduction of the barrier height by this image charge. It also shows that the trapezoidal barrier is rounded, the apparent barrier height is reduced, and the current between the electrodes is increased due to this reduction of the barrier height.

2.4 Scanning Tunneling Spectroscopy

As shown in section 2.2, the tunneling current arising from a tip-vacuum-sample system is dependent on the bias voltage, the apparent barrier heights (which contain the workfunctions of the tip and sample), the tip-sample distance, and the density of states of the tip and sample. These relationships open an interesting series of measurements to determine the properties of the surface of a sample.

The relationship between the current, I, and barrier length, z, is apparent in most of the STM models outlined in the previous section. Thus, it is possible to measure the effective barrier height, ϕ_{eff}, by looking at the current response of the tip with respect of a change in the tip-sample distance. At low biases ($V << \phi_{eff}$), the equation of the transmission factor from equation 2.16 approximates to

$$T \propto \exp\left[-\frac{2\sqrt{2m}z}{\hbar}\sqrt{\frac{\phi_t + \phi_s}{2}}\right], \tag{2.20}$$

meaning the tunneling current is now proportional to the transmission coefficient. The work functions of metals are approximately the same, so the approximation leads to a solution of the apparent barrier height, ABH, as follows

$$ABH = \frac{\hbar^2}{8m}\left(\frac{d\ln I}{dz}\right)^2, \tag{2.21}$$

where $d\ln I/dz$ is the slope of the resulting current-distance measurement. Given the relationship between the current and distance, these measurements are not without

their difficulties. The stability of the tip with respect to the sample and any drift in the tip positioning plays a strong role in accurate I-z measurements.

A second direct measurement is the relationship of the bias voltage V to the tunneling current I. Beginning with a given tip height from a current setpoint and initial voltage, the feedback loop is deactivated and the bias voltage is changed. The resulting current response from the system is measured as a function of the change in voltage bias. From equation 2.17, and from Fig. 2.2, taking the Fermi Energy of the sample as the reference energy, the current from equation 2.22 becomes:

$$I = \frac{4\pi e}{\hbar} \int_0^{eV} \rho_t(\epsilon - eV)\rho_s(\epsilon)T(\epsilon, V, z)d\epsilon, \tag{2.22}$$

where eV is also the difference between the Fermi energy of the tip and the Fermi energy of the sample. The relationship between the current and the bias voltage is contained in both the density of states of the tip and the sample (from the integral) and also in the transmission coefficient. This means it is difficult to interpret an I-V curve. However, some assumptions can be made in order to extract some information. First, only the maximum value of the integral eV is taken into account given the spectroscopy is probing the highest energy value of the surface of the sample (which is fine as a first approximation):

$$dI = \frac{4\pi e}{\hbar}\rho_t(0)\rho_s(eV)T(\epsilon, V, z)d\epsilon. \tag{2.23}$$

Second, at the maximum value $\epsilon = eV$, any change in the bias will change the maximum electron energy, $e\Delta V = \Delta\epsilon$, meaning:

$$dI = \frac{4\pi e^2}{\hbar}\rho_t(0)\rho_s(eV)T(\epsilon, V, z)dV. \tag{2.24}$$

Finally, the density of states of the tip and the transmission coefficient are assumed to be voltage independent; the tip is typically of a metal with a near-constant density of states close to the Fermi energy, and the transmission factor can be approximated

to be bias independent for biases much lower than the apparent barrier height. This means equation 2.22 can be rewritten as

$$\frac{dI}{dV} \approx \frac{4\pi e}{\hbar}\rho_{t,0}T(z)\rho_s(eV). \tag{2.25}$$

Now, with the assumptions made, the density of states of the surface is proportional to the derivative of the current with respect to the voltage bias. This is known as a dI/dV or conductance curve. This derivative can simply be the numerical derivative of acquired I-V data. However, the numerical method lends itself to error if the number of points in an I-V scan is not chosen appropriately. A different method of measuring the derivative of the I-V curve is modulating the bias while taking the scan and using a lock-in amplifier to modulate the bias using a small AC voltage. In this way, the derivative of the curve (i.e. conductance) can be measured simultaneously with the I-V curve.

Chapter 3

Principles of THz-STM

3.1 THz Pulse Generation

One of the methods to generate THz pulses is using a photoconductive emitter together with femtosecond laser pulses (Fig 3.1). This emitter is typically constructed using a semiconductor with two electrical contacts made from a metal. With the use of the femtosecond pulse at a photon energy large enough to surpass the semiconductor band gap, the surface of the semiconductor can be irradiated generating negative (electrons) and positive (holes) charge carriers. A bias is applied across the metal contacts on the semiconductor, accelerating the created electrons towards the positive bias contact and the holes towards the negative bias contact. The acceleration of the carriers generates a picosecond duration THz pulse. The amplitude of the THz pulse is proportional to the acceleration of the carriers. This allows the control of the THz electric field through the bias voltage: a larger bias leads to a larger acceleration of carriers and thus a larger electric field. The bias is also modulated, lowering power dissipation in and extending the lifetime of the antenna.

With a pulsed laser train, the recombination time of the electron-hole pairs is important between pulses to allow the photoconductive process to be repeatable and a THz pulse train to be achieved. An example of a laser pulse source is a Ti:Sapphire femtosecond pulse generation with a centered wavelength of 800 nm and a repetition rate of 250 kHz. This means that the semiconductor used in the photoconductive

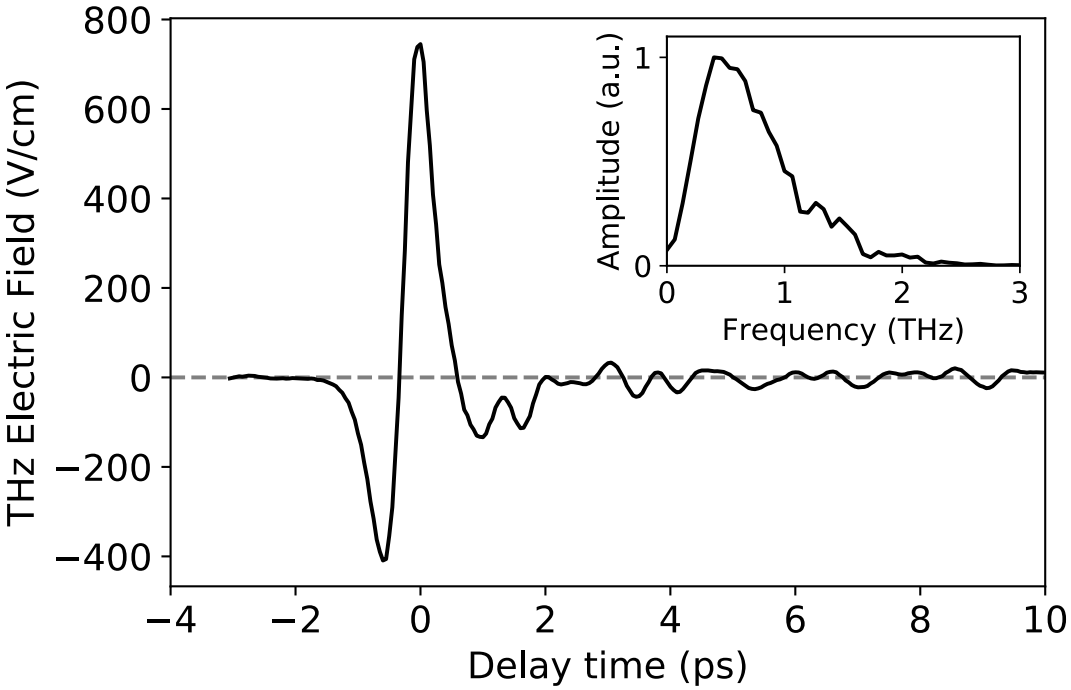

Figure 3.1: THz pulse generated using a GaAs photoconductive antenna and measured using electro-optic sampling. The corresponding Fourrier transform is shown in the inset. The time axis has been shifted such that the peak of the THz pulse is at 0 ps. The peak of the frequency spectrum is at 0.5 THz.

source must have a band gap energy less than 1.55 eV with carrier recombination lifetimes of less than 4 μs. A typical semiconductor candidate is GaAs due to its band gap energy of 1.435 eV at room tempertature and carrier lifetimes of several hundred picoseconds [52–54].

3.2 THz Detection via Electro-Optic Sampling

It is important to determine the electric field of the THz waveform incident onto the STM tip. Given the THz induced voltage modulates the tunnel current based on the non-linearity of the I-V curve of the tunnel junction (see section 3.3), it is then important to also determine the strength of the THz field. One method of measuring the electric field of an ultrafast pulse is called free-space electro-optic sampling (EOS), which utilises the electro-optic effect.

To begin, the electro-optic effect is a change of optical properties in a material due to the introduction of an external electric field. There are two processes related to the electro-optic effect: a linear relationship known as the Pockels Effect, and a non-linear (quadratic) effect known as the Kerr effect. The polarization due to the Pockels effect can be described as

$$P_i(\omega + 0) = 2\epsilon_0 \sum_{jk} \chi^{(2)}_{ijk}(\omega = \omega + 0) E_j(\omega) E_k(0), \tag{3.1}$$

where $P_i(\omega)$ is the polarization, ϵ_0 is the vacuum permittivity, $\chi^{(2)}_{ijk}(\omega = \omega + 0)$ is the second order non-linear susceptibility tensor for an electric field with frequency ω and another electric field of frequency 0 (static electric field).

The Maxwell equation for a displacement field $\mathbf{D}$ through a medium with susceptibility χ and electric field $\mathbf{E}$ in three dimensions is given by

$$\begin{bmatrix} D_x \\ D_y \\ D_z \end{bmatrix} = \begin{bmatrix} \epsilon_{xx} & \epsilon_{xy} & \epsilon_{xz} \\ \epsilon_{yx} & \epsilon_{yy} & \epsilon_{yz} \\ \epsilon_{zx} & \epsilon_{zy} & \epsilon_{zz} \end{bmatrix} \begin{bmatrix} E_x \\ E_y \\ E_z \end{bmatrix}, \tag{3.2}$$

assuming low field strengths and using the relation $\epsilon_r = 1 + \chi$, where ϵ_r is the dielectric permeability tensor and ϵ_{ij} are the elements of ϵ_r. The dielectric permeability tensor is symmetric due to conservation of energy. Thus, $\epsilon_{ij} = \epsilon_{ji}$, meaning there are six independent elements to the tensor ϵ_r.

The energy density of a wave propagating through a medium, u, is given by $u = \frac{1}{2}\mathbf{E} \cdot \mathbf{D}$, so that

$$\begin{aligned} u = &\frac{1}{2\epsilon_0}\left[\left(\frac{1}{n^2_{xx}}\right)D_x^2 + \left(\frac{1}{n^2_{yy}}\right)D_y^2 + \left(\frac{1}{n^2_{zz}}\right)D_z^2 \right. \\ &\left. + 2\left(\frac{1}{n^2_{yz}}\right)D_y D_z + 2\left(\frac{1}{n^2_{xz}}\right)D_x D_z + 2\left(\frac{1}{n^2_{xy}}\right)D_x D_y\right], \end{aligned} \tag{3.3}$$

where $(1/n^2_{ij}) = \epsilon_0/\epsilon_{ij}$. Given $2u\epsilon_0$ is a constant, we can rewrite $x = \frac{D_x}{\sqrt{2\epsilon_0 u}}$, $y = \frac{D_y}{\sqrt{2\epsilon_0 u}}$, and $z = \frac{D_z}{\sqrt{2\epsilon_0 u}}$ to get an ellipsoid of the form

$$1 = \left(\frac{1}{n_{xx}^2}\right)x^2 + \left(\frac{1}{n_{yy}^2}\right)y^2 + \left(\frac{1}{n_{zz}^2}\right)z^2 + 2\left(\frac{1}{n_{yz}^2}\right)yz + 2\left(\frac{1}{n_{xz}^2}\right)xz + 2\left(\frac{1}{n_{xy}^2}\right)xy. \quad (3.4)$$

This equation describes the index ellipsoid of a material where x and y relate to the face of the medium, and z the length of the medium, and is important in the description of the optical properties of a material. If an electric field (like such from a THz pulse) is introduced into the medium, the index ellipsoid will change; that is the optical constants will be dependent on the incident electric field. If $\frac{1}{n_{ij}^2}(\mathbf{E})$ is now expanded using a Taylor series about $\mathbf{E} = 0$, and ignoring higher order terms, those constants are now

$$\left(\frac{1}{n_{ij}^2}\right) = \frac{1}{n_{ij}^2}(0) + \sum_k r_{ijk}E_k + O(\mathbf{E}^2), \quad (3.5)$$

where $i, j, k = 1, 2, 3$ where $1 = x$, $2 = y$, and $3 = z$; and r_{ijk} are the elements of a tensor and are known as the linear electro-optic coefficients. The $\frac{1}{n_{ij}^2}(0)$ matrix has only non-zero terms along the diagonal, where if no field is applied to the crystal those terms would correspond to the three principal refractive indexes. Given the symmetry of the tensor, it is common to relabel the indices i, j, k to l, k, where l is defined in Table 3.1.

i/j	1	2	3
1	1	6	5
2	6	2	4
3	5	4	3

Table 3.1: Reduced indices table for compact notation. Example: if $i, j = 1, 3$ then $l = 5$.

This allows the linear electro-optic tensor to be written as

$$\mathbf{r} = \begin{bmatrix} r_{11} & r_1 & r_{13} \\ r_{21} & r_{22} & r_{23} \\ r_{31} & r_{32} & r_{33} \\ r_{41} & r_{42} & r_{43} \\ r_{51} & r_{52} & r_{53} \\ r_{61} & r_{62} & r_{63} \end{bmatrix}. \tag{3.6}$$

A typical crystal for THz detection is ZnTe, a cubic $\overline{4}3m$ crystal with a linear electro-optic tensor given by

$$\mathbf{r} = \begin{bmatrix} 0 & 0 & 0 \\ 0 & 0 & 0 \\ 0 & 0 & 0 \\ r_{41} & 0 & 0 \\ 0 & r_{41} & 0 \\ 0 & 0 & r_{41} \end{bmatrix}. \tag{3.7}$$

This material has a single electrooptical coefficient $r_{41} = 4.0\text{x}10^{-12} m/V$ and an ordinary index of refraction $n_x = n_y = n_z = n_0 = 2.853$ at $\lambda = 800$ nm. If the incident electric field is applied along the z-direction, the index ellipsoid becomes

$$1 = \frac{x^2}{n_0^2} + \frac{y^2}{n_0^2} + \frac{z^2}{n_0^2} + 2r_{41}E_{THz}xy. \tag{3.8}$$

Replacing $x = (X - Y)/\sqrt{2}$, $y = (X + Y)/\sqrt{2}$, and $z = Z$, the index ellipsoids major and minor axes n_X and n_Y, respectively, become

$$\begin{aligned} n_X &= n_0 + \frac{1}{2}n_0^3 r_{41}E_{THz}, \\ n_Y &= n_0 - \frac{1}{2}n_0^3 r_{41}E_{THz}. \end{aligned} \tag{3.9}$$

These n_X and n_Y values now denote the index of refraction for the material after the introduction of the electric field as shown in Fig. 3.2. It can be inferred by these new axes for the index ellipsoid that a second field travelling through the medium will now acquire a phase difference due to the two indices being different values.

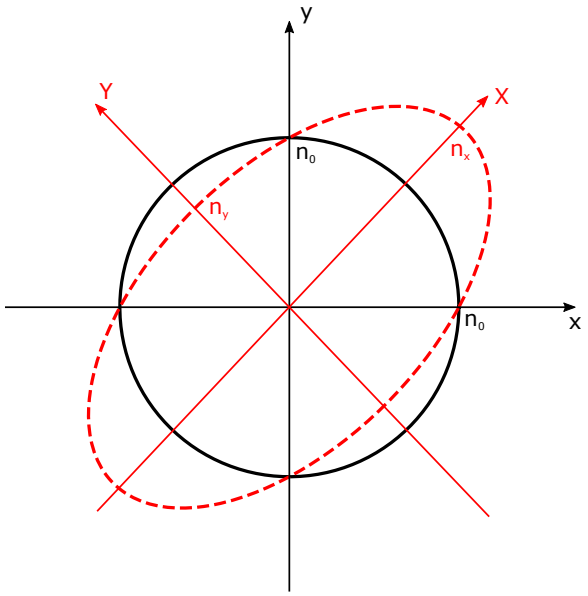

Figure 3.2: Index ellipsoid absent of a weak electric field (black solid circle) and with the introduction of an electric field (red dashed ellipse). The ellipsoid is exaggerated for visual effect as the change in the effective index is small for the fields used in this study.

Thus, if a static beam is introduced also directed in the z-direction (Fig. 3.3), the optical retardation from this new ellipsoid will be

$$\begin{aligned} \Delta\Phi &= (n_X - n_Y)\frac{2\pi L}{\lambda}, \\ &= \frac{2\pi n_0^3 r_{41} L}{\lambda} E_{THz}, \end{aligned} \tag{3.10}$$

with L the propagation length of the beam through the crystal and λ the wavelength of the input beam. Using a system comprised of a quarter-waveplate and a polarizer, it is possible to separate the x and y components of the output beam with a Wollaston prism into two separate balanced photodiodes. The resulting ratio of the two measured values gives the phase change $\Delta\Phi = \frac{I_y - I_x}{I_y + I_x}$. Given the incident electric field strength of the THz pulse changes with time, the resulting index ellipsoid's axes will change, meaning a change in the optical retardation. This means the electric field of the THz proper can be calibrated over time, giving an EOS waveform as shown in Fig. 3.1.

The transmission factor of the ZnTe crystal is also important to consider while determining the electric fields of the pulse. The crystal introduces reflection losses, and at a refractive index of approximately 3.2 for low-THz frequencies, the transmission factor of the crystal is 0.48. This gives as a final calculation for the THz electric field in EOS to be:

$$E_{THz} = \frac{2\pi n_0^3 r_{41} L}{\lambda 0.48} \frac{I_y - I_x}{I_y + I_x}, \tag{3.11}$$

where I_y and I_x are the currents measured through the two balanced photodiodes.

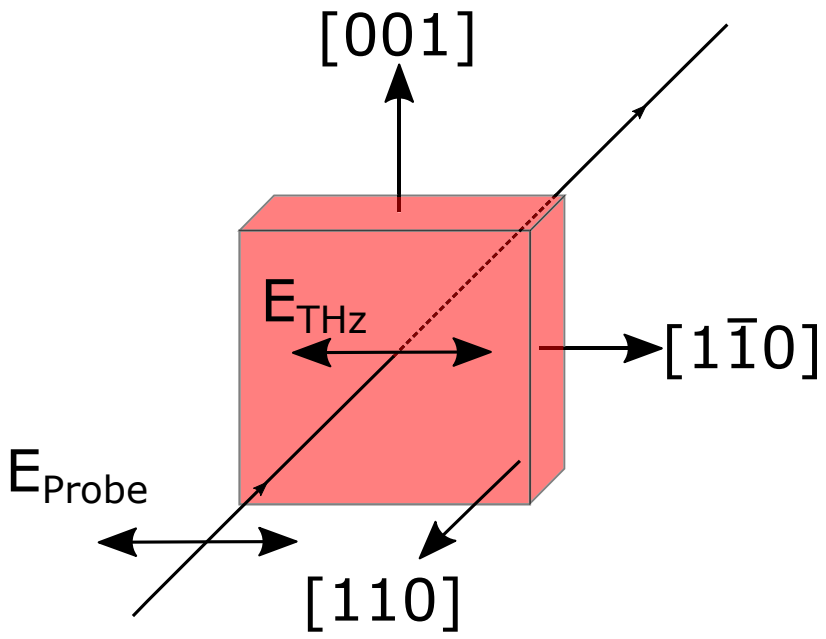

Figure 3.3: Example of the orientation of a ZnTe crystal for free-space electro-optic sampling. The THz electric field is onset to the crystal, causing a birefringence. The electric field of the probe beam while travelling through the crystal after will have a phase change from this birefringence.

3.3 THz Coupling to an STM tip

It has been shown that THz radiation can be coupled to a metallic tip which acts like an antenna or waveguide for the radiation [55–57]. This effect is the basis of THz-STM; as a terahertz pulse beam is shined on the STM tip, it is guided to the

end of the tip and enhanced at the tunnel junction. Although the size of a 1 THz wave is long at 0.3 mm, an STM tip causes the THz radiation to be confined and enhanced down to the nanometer scale. This in turn allows a transient THz bias to add to the DC bias from the STM system. Given the THz electric field changes over time, then the voltage introduced from the THz electric field will also change over time.

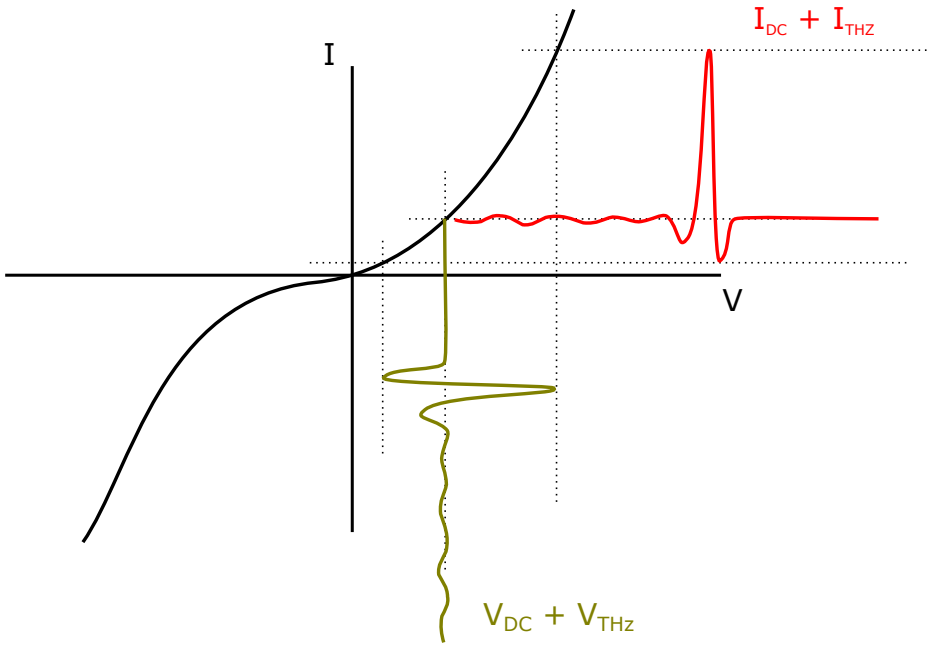

Figure 3.4: Schematic of a THz pulse incident on a tunnel junction. The THz pulse coupled to the tip modulates the bias of the system (gold). Given the non-linearity of the I-V curve, the current response from the modulated voltage will in turn be modulated (red).

Given the non-linearity of the current-voltage response in the tunnel junction as shown in equation 2.17, the onset of the time-varying bias voltage onto the junction produces a time-varying rectified current response that has a net rectified current. Since the actual sub-picosecond tunnel current induced by the THz is too quick for the tunnel current amplifier, the rectified current response is instead measured. This rectified current is measured as the number of rectified electrons per pulse, or $I_{THz,avg} = \frac{dQ}{dt} = e(f_{rep})N_e$, where f_{rep} is the repetition rate of the laser pulse and N_e is the number of rectified electrons. The measured current is now a combination of the

static DC current and the transient THz-induced current. The THz-induced current response is also spatially localized given the I-V response only occurs at the STM junction. Therefore, the THz-STM system is now capable of probing sub-picosecond dynamics with nanometer precision on the surface of a sample.

It is also important to differentiate the DC current from the THz-induced current in some instances. The STM has a feedback loop to change the height based on measured currents. To avoid a convolution with the DC current measurement, the THz pulse can be chopped at a frequency above the bandwidth of the STM feedback loop. This allows the system to ignore the minute changes that arise from the onset THz. Also, the chopping frequency is set below the pre-amplifier bandwidth of the system, allowing for current measurements to be detected by a lock-in amplifier, thus allowing the detection of THz currents in the system separate from the DC current response.

3.4 THz-STM of Materials

THz-STM, although a relatively new technique, has already demonstrated many applications of observing surface dynamics of materials. Cocker et al. published the first work of THz-STM in 2013 [35]. Using an STM system in ambient conditions, they coupled a THz pulse to the tip of the STM without any changes to the ambient STM system. From the non-linearity of the I-V response in the tunnel junction, they were able to modulate the bias voltage and read a rectified current response. Autocorrelation measurements on the surface of HOPG and on gold nanoislands showed electron generation times as low as 350 fs, showing the sub-picosecond time resolution of the system. They also presented THz-STM scans over the nanoislands at different autocorrelation overlap times, demonstrating the simultaneous nanometer spacial resolution and aforementioned temporal resolution of the system. Finally, they performed optical-pump/THz-STM-probe experiments on InAs nanodots grown on GaAs. The measurements showed a decay time from the transient THz-STM re-

sponse of approximately 1 ps, which agreed with ultrafast studies of similar systems [58].

Three years later, Cocker et al. used THz-STM to observe the motion of a single pentacene molecule absorbed on NaCl after excitation from a THz pulse [59]. The system was under ultra-high vacuum and low temperatures. By keeping the STM tip height constant, a THz pulse pair was incident onto the sample where the first THz pulse caused electrons to be excited from the highest occupied molecular orbital of the pentacene molecule causing it to vibrate, while the second THz pulse probed the changes in the tunnel current from the oscillations of the molecule. This established a new method for using THz-STM to probe and image ultrafast movements of a single molecule.

In 2017, Jelic et al. atomically resolved the surface of Si(111)-(7x7) with the THz-STM where only the THz induced current contributed to the tunneling current (0 d.c. bias between the tip and sample), called THz-driven STM (TD-STM) [38]. This experiment used the same UHV-STM system as described in this thesis with the THz focused to the tip. They compared regular STM scans and TD-STM scans of the Si(111)x(7x7) surface and saw that the TD-STM transient current was much larger than the d.c. current, attributing this difference to band bending of the depletion layer allowing transport between the bulk and the surface of the sample. This is typically not seen in regular STM scans on Si(111)-(7x7), showing the possibility of THz-STM to allow new conduction pathways betweem the bulk and surface.

In 2020, Luo et al. performed TD-STM on Cu(111) to demonstrate THz-STM and TD-STM on a metal, and used a tunneling model with a 3D tip geometry to explain the THz current response at step edges and defects [40]. The use of a metal allows for a true approximation of the Bardeen model (see sec. 2.2) given metals have very small variations in their density of states. Using a UHV-STM system with a sample temperature of 100 K, their 3D model agreed well with the THz-STM measurements performed on the surface, allowing for a better understanding of both the tip geometry

effects and a method to quantify the THz-induced bias voltage.

Just this year (2021), Yoshida et al. published results on visualizing the ultrafast motion of electrons over surface defects and step edges on C_{60} monolayers [39]. With the sub-nanometer resolution of the STM and the sub-picosecond time resolution of THz, as well as an infrared pump laser pulse, they were able to time-resolve electron motion about step edges and defects. The pump excited the carriers from the highest occupied molecular band into the lowest unoccupied molecular orbital while the THz-induced current probed the change in electron population. They were able to successfully demonstrate the movement of electrons after optical excitation with this method, allowing for a visualization of the surface dynamics of the material.

While not a comprehensive list, the ability of THz-STM to observe different effects on different materials allows for a new and exciting method of measuring, characterizing, and visualing surface dynamics of many materials. There are also advancements towards using spintronic high broadband THz emitters for THz-STM, allowing for higher bandwidth (1-30 THz) pulses to couple to the tip, with voltage transients up to 2 V and 15 THz frequencies measured in the near-field [37].

Chapter 4

UHV-STM System

4.1 Ultrahigh Vacuum Scanning Tunneling Microscope

The UHV-STM system used in this work is a commercial system purchased from RHK Technologies (RHK-UHV-SPM 3000). The system is comprised of three chambers which can be separated via two internal gates that can be opened or closed from outside the system. The entire system also sits on an active piezoelectric damping system (STACIS 2100/3000, TMC) to minimize vibrations from outside the system affecting data collection during an STM scan.

First, the load-lock chamber serves as the point of entry and exit of the UHV system. A combination of a roughing pump and turbo pump are used to depressurize the chamber until approximately 1x10^{-8} torr. An inlet valve separates the pumps from the system and allows for the pumps to be disabled during an STM scan. This keeps the chamber under vacuum for ease of sample transfer if required. This is also important to avoid the introduction of outside contaminants into the system. When a new sample or tip is placed into the load-lock chamber, it is baked in-chamber at approximately 130°C for 12 hours before being moved into the chamber in order to remove any organic contaminants.

Next, the preparation chamber is used for in-vacuum sample deposition, cleaning, and annealing. Gate 1 is used to isolate the load-lock chamber from the preparation

chamber. The preparation chamber is kept at a pressure of $< 1\text{x}10^{-10}$ torr using ion pumps. A transfer arm is used to move the sample between the load-lock chamber and the STM chamber. The transfer arm has an electronic connection with a sample puck (section 4.3). This connection allows the sample to be resistively heated for in-situ annealing. Also present in the chamber is an argon ion gun. With the sample to be cleaned at a desired grazing angle, a filament within the gun and an outside controller sets the acceleration voltage. To the side of the main cavity of the chamber, a sub-section is used for deposition of materials. This is useful for depositing onto substrates without removing the sample from vacuum: the substrate can be characterized and cleaned, then another material can be deposited in-situ.

Finally, the STM chamber is comprised of a sample elevator for storage and an STM stage. Gate 2 isolates the STM chamber from the preparation chamber. The elevator allows for storage of up to 6 samples or tips for later use in the system. Much like having a deposition chamber, the elevator allows for tips and samples to be in vacuum while not in use to avoid contamination or oxidation. The chamber also has a copper stage for in-vacuum tip preparation, further explained in section 4.2. An inlet allows for a connection with a cryostat to cool the sample on the STM stage for low temperature scans.

The STM stage contains contacts much like the ones on the transfer arm of the preparation chamber to heat the sample during scans (although this is not used in this study). It also contains contacts such that a thermocouple could be included in the sample holder configuration to monitor the sample temperature during cooling and while performing scans. While performing scans, the sample stage is biased while the tip and tip head is virtually grounded.

The STM scan head has three piezo legs capped with glass balls. These balls will glide across the top of the sample holder as an approach is made. A head manipulator is used to manually move the scan head vertically to approach or retract the scan head from the STM stage. When the glass balls are in contact with the sample puck,

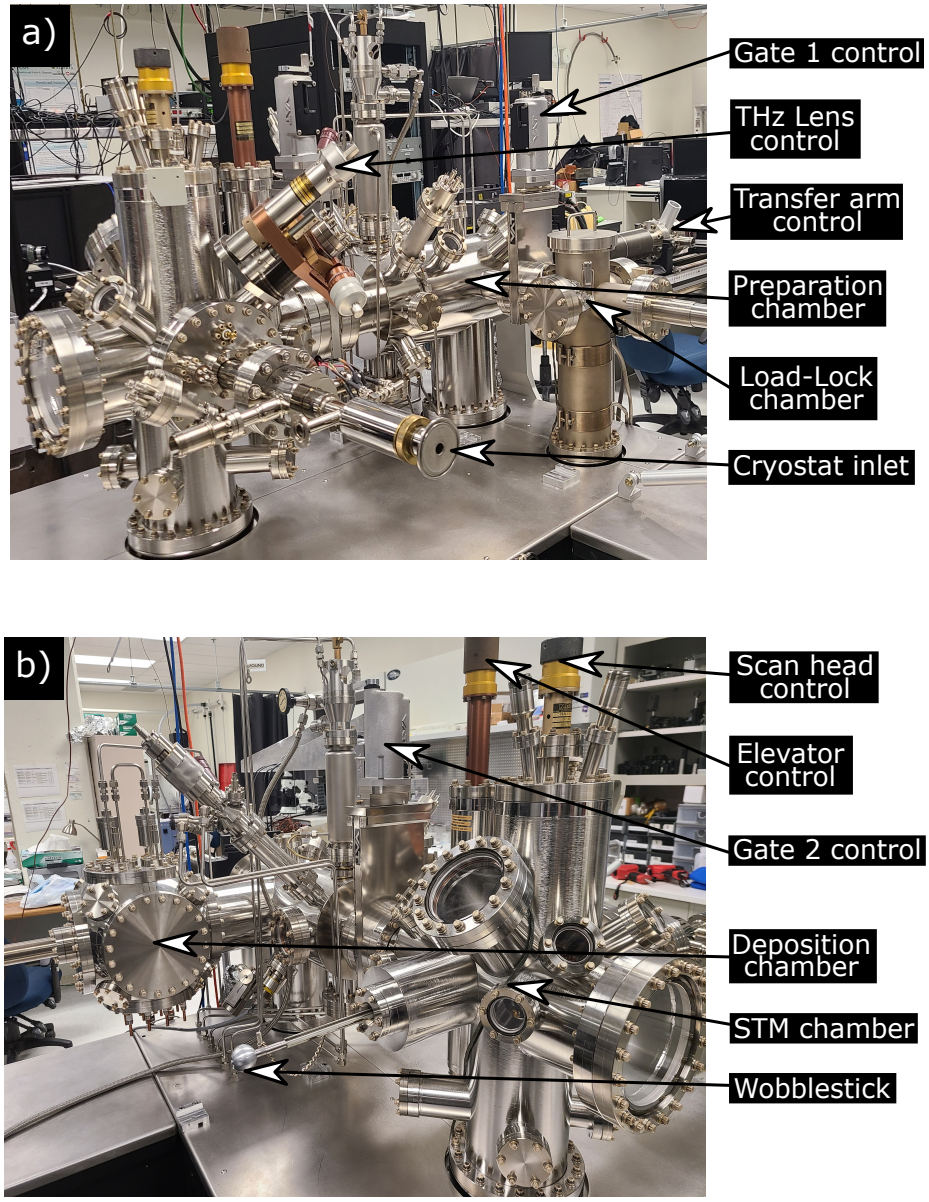

Figure 4.1: Exterior of the UHV-STM system. a) The load-lock chamber and preparation chamber is separated by gate 1 controlled manually from the exterior. The transfer arm control in the background allows for transport of a sample or tip from the preparation chamber to the STM chamber and can be rotated for various sample preparation methods in the chamber. The THz lens control allows for external alignment of the THz beam lens focused on the STM sample. The cryostat inlet allows liquid nitrogen or helium to flow to the sample stage for low-temperature measurements. b)The deposition chamber open to the preparation chamber allowing material preparation in-situ. The preparation chamber is kept isolated from the STM chamber using gate 2. The elevator and scan head controls allow manual vertical control of the sample elevator and scan head outside the system. A wobble stick allows manipulation of sample and tip holders in the system.

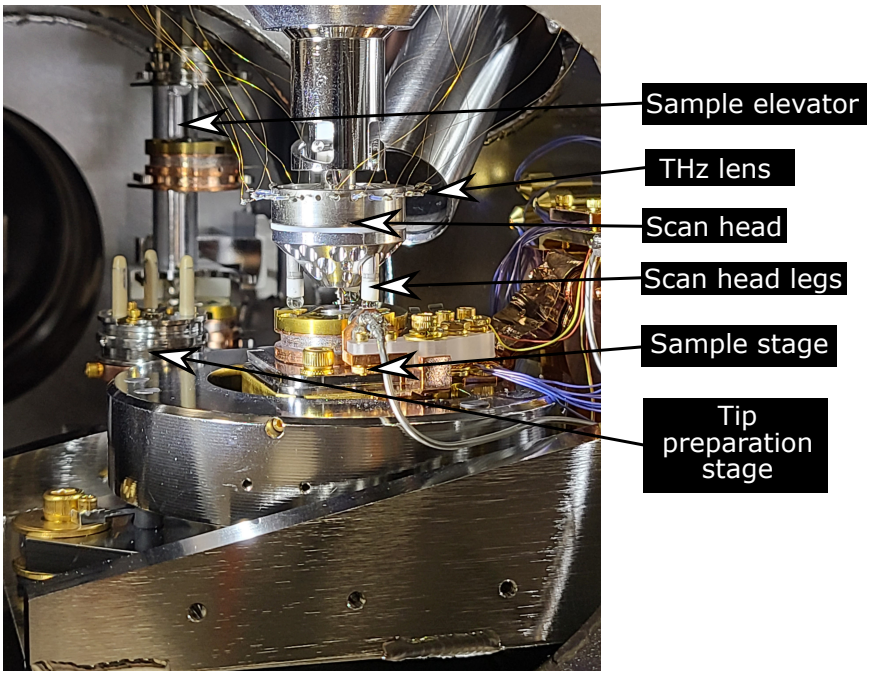

Figure 4.2: Interior of the STM chamber of the UHV-STM system. The sample elevator is in the background of the image. A tip transfer holder is placed on the tip preparation stage located behind the sample stage. The THz lens allows for a close focus of the THz beam onto the sample surface. The scan head has three scan head legs positioned for tunneling of a sample. A tip in a tip holder is in the scan head. The sample stage ensures the sample holder is fixed during scans and is biased for STM operation.

a regular step motor is used for a coarse approach. The sample holder surface is slanted so that as the motor turns the STM head the tip approaches the surface. Piezo tubes in the three legs are used to precisely approach the tip within angstroms of the sample surface. At the bottom of the scan head there is a scan tube that holds the tip holder in place for STM operation.

4.2 STM Tip Preparation

Gold and tungsten STM tips were prepared using an electrochemical etching method adapted from [60] for gold and [61] for tungsten. Figure 4.3 shows the setup of the system. The system is on a pneumatic vibration isolation table that uses dry nitrogen to limit vibrations during electrochemical etching.

The gold and tungsten wires were purchased from Alfa Aesar, and had a 99.998% and 99.95% purity, respectively. Both wires were 0.25 mm in diameter according to the company label. Pre-preparation of the W wire was necessary due to the presence of oxides forming at the wire surface. Thus, the wire was sanded with 180 grit sandpaper before further tip preparation. Both wires were then prepared using the same methods (with different chemical etching solutions).

The wire was cut into 1-1.5 cm lengths and placed into methanol. The wire was sonicated in the methanol for 2 minutes to remove any possible surface contaminants. A solution of 1:1 ratio of ethanol and hydrochloric acid was prepared for the Au tips while a 2 M solution of sodium hydroxide was prepared for the W tips. The tips were then placed in the tip preparation area as shown in Fig. 4.3 a). The solution is placed

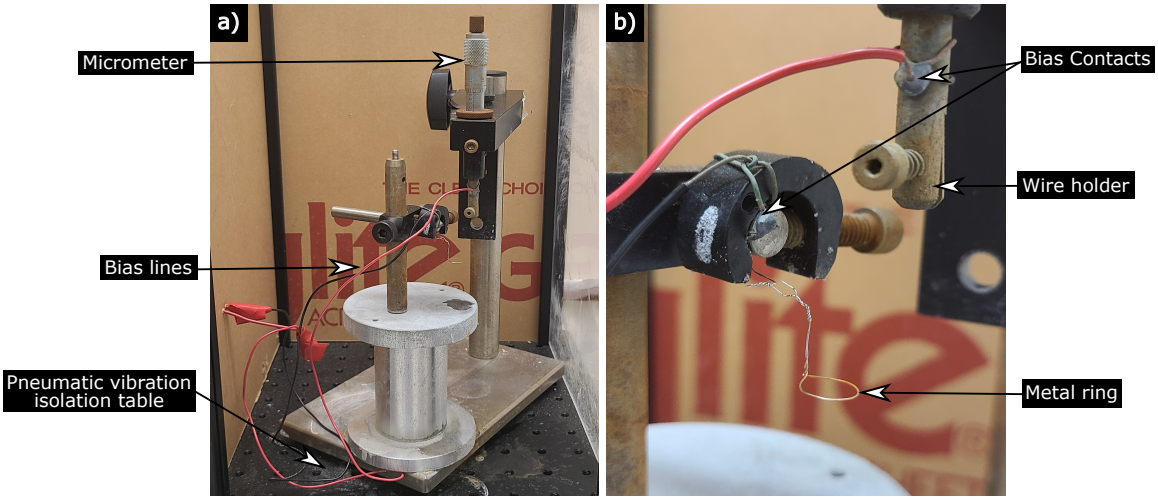

Figure 4.3: Photos of the tip preparation setup. a) A micrometer allows for fine vertical positioning of the wire into the solution. Bias lines allow the wire and ring to be biased. The tip preparation setup sits on a pneumatic isolation chamber to minimize external vibrations. b) Bias contacts are soldered onto the wire holder and metal ring. The wire holder is positively biased while a metal ring of the same material as the wire being etched is negatively biased, allowing for a complete circuit through the the required chemical medium.

under either a gold or tungsten ring to match the metal wire being etched (Fig 4.3 b)). The ring is then lowered such that it dips into the solution and then is raised to create a meniscus of solution. The tip is lowered to the center of the loop such that

only the tip is submerged. A DC power supply applies a bias between the tip and the ring. As a result, a current flows from the tip to the ring. The solution acts as the electrolyte where the ions will want to bond with the tip material (the Cl for gold tips and the oxygen from the OH for tungsten). Voltages used were 2.3 V for gold tips and 4.5 V for tungsten tips. Since the tip completes the circuit, as the tip is being etched the measured current decreases. Once the measured current is sufficiently low, the voltage supply is turned off. The tip is then cleaned using de-ionized water and mounted into the tip holder to be placed in the STM system.

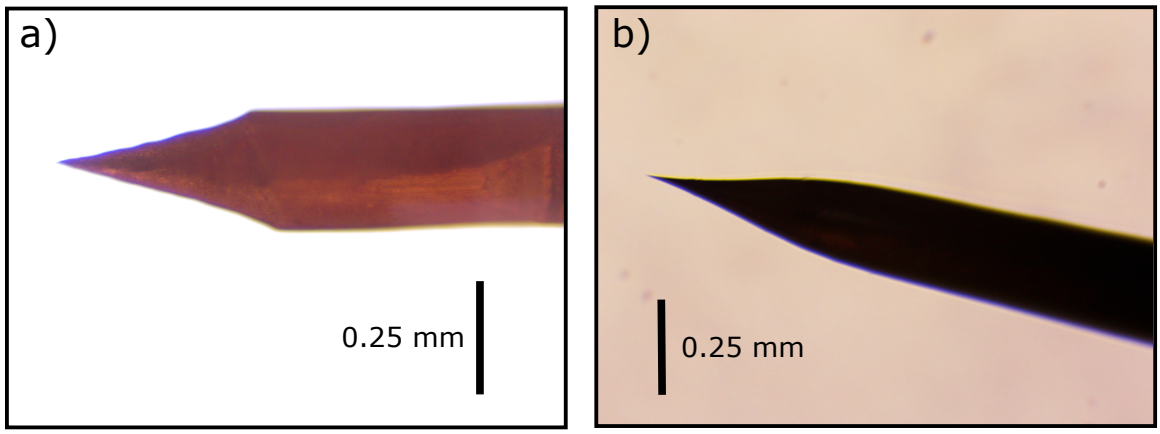

Figure 4.4: Microscope images of a) gold and b) tungsten tips after tip preparation using the electrochemical etching method.

The copper stage for tips in the STM chamber mentioned in section 4.1 allows for in-vacuum STM treatment without the need to remove the tip from the vacuum environment. There are two methods to reshaping the tip using this configuration. First, electron bombardment is used to remove any oxides that may be present, especially on tungsten tips [62]. A floating power supply applies a voltage and current across a tungsten filament in the copper stage, generating a current. The tip is grounded through the copper stage, and the current between the tip and the stage is measured during bombardment. Typically, the power supply settings used for electron bombardment is -150 V with the current from the power supply increased until the current between the sample and stage reaches 1-3 mA (typically 1.5-2 A of generated

current). The electrons from the filament are thus bombarded onto the tip. The electrons have enough energy to allow tungsten oxides to form on the tip apex and be removed from the tip surface. This process is typically done within 30 seconds to a minute. The kinetic energy of the electrons causes the tip to be heated, and the small tip apex can melt creating a blunt tip.

Field emission is then used to reshape the tip. The configuration is nearly the same as electron bombardment but the current generator is not used. The bias across the filament is now positive such that electrons will travel from the tip to the filament. As the voltage across the filament is increased, the number of electrons field emitted from the tip to the sample also increases. The electrons from the tip travelling to the filament do so via the tip apex, shaping the tip. Typically, voltages ranging from 200-4000 V are used depending on the measured actual current. The measured tip-stage current should be between 1-100 nA, and the applied voltage is changed to accommodate those changes. As the tip sharpens due to electromigration, the field enhancement at the tip increases and the current will increase. The tip is deemed sharp once the actual current is stable over a long period of time. Heating effects are possible, but minimal, and will not affect the tip shape at the apex.

4.3 Tip and Sample Holders

Tip and sample holders were specifically designed for use in the UHV STM system as shown in Figure 4.5. The U-shape bases ensure proper connection with the sample filaments to the transfer arm and STM stage and consistent tip and sample orientation. Mounting a tip into the tip holder requires the tip to be sufficiently long (between 8 and 15 mm). The mechanism for keeping a tip into the tip holder is mechanical: the long end of the tip must be bent in order for it to not slip out of the holder. Once the tip is inserted into the tip holder, it is placed sharp-side down into a tip transfer holder as seen in figure 4.5 a). A thick wire is used to lock the tip holder into the tip transfer holder to avoid the tip holder falling into the system. The bottom of the tip

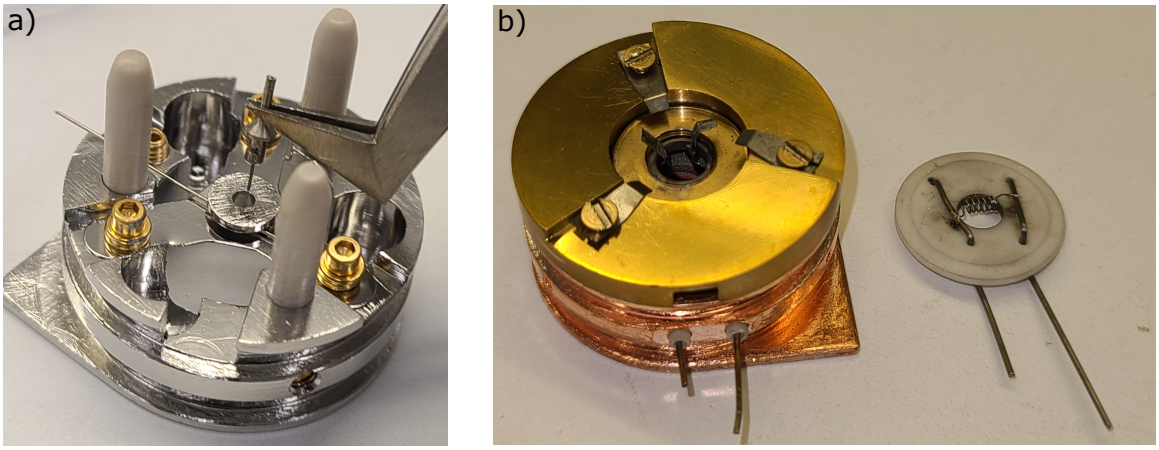

Figure 4.5: a) Tip holder and tip transfer holder used to transport the tip in the UHV-STM system. Tweezers are holding the tip holder where a wire has been inserted for demonstration purposes. The tip transfer holder below the tip holder has a horizontal wire used to lock the tip holder in place. The three protruding legs allow for precise alignment with the STM scan head. b) A sample holder used in the UHV-STM chamber is on the left configured for semiconductor samples while the filament on the right replaces the protruding contacts in the sample holder for metal samples. Both have electronic contacts through the side of the sample holder allowing contact with the transfer arm and STM sample stage.

transfer holder is open, allowing for in-vacuum tip preparation as outlined in section 4.2. Three rods are present to allow for proper alignment with the STM scan head to mount the STM tip. The scan head also uses mechanical force to keep the tip holder from falling out during scans.

The sample holder comes in two variations, one for semiconductor samples and another for metal samples as shown in Figure 4.5 b). The semiconductor sample puck uses two metal films to make contact with a conductive base allowing the semiconductor to be directly biased with the STM system. This also allows for quick annealing or flashing of the semiconductor in-situ. The films are connected via two contacts that allow for a complete circuit configuration. Thus, the sample is heated through thermal conduction from film-sample-film. The metal sample holder, by contrast, uses a filament instead of direct contacts. This allows for electron bombardment heating for the sample in vacuum instead of direct heating, much like the tip preparation method. Both the semiconductor and metal sample pucks can be biased for an STM

scan.

In both cases, the top of the sample puck has three slanted areas for the three legs of the STM scan head. The position of the sample puck is constant scan-to-scan due to the U-shaped base. As a tip is approached, each of the STM scan head legs will arrive at the top of the ramps and will slowly glide down allowing for smooth operation with no jolting of the tip. Screw clamps are used at the top of the sample holder to ensure the sample within does not fall. The height of the sample and the length of the tip are measured such that no contact is made from tip to sample when the STM head lands, and sapphire disks are used to ensure the sample height is sufficient and used as a buffer between the clamps and the sample.

4.4 Laser Setup

The laser pulses used in this work were generated using a combination of a titanium:sapphire regenerative amplifier (Coherent RegA Model 9000), a titanium:sapphire modelocked oscillator (Coherent Micra), and a diode-pumped laser (Coherent Verdi V-18 for the BSCCO measurements of Chapter 5 and Lighthouse Photonics Inc. Sprout-G for the Au and Ag measurements of Chapters 6 and 7, respectively). The output beam of the system was centered at 800 nm with a repetition rate of 250 kHz and compressed to a pulse duration of 212 fs, which will be roughly 71 fs at the THz source due to group velocity dispersion. A typical average pulse power on output of the compressor is 1.1 W.

Fig. 4.6 shows the schematic of the beam for the entire experiment. The exit beam is split into two beams using a 80/20 beam splitter. First, the 80% beam travels through a delay stage for time-resolution measurements, and will continue on to be the THz generation beam. The other 20% of the beam is further split by another 80/20 beam splitter. The new 80% (16% of the total output beam power) is used as the pump beam. The new 20% (4% of the total beam power) is split by another 80/20 beam splitter. The 80% (3.2% of the total beam power) is used as

the sampling beam for electro-optic sampling (see section 3.2). Finally, the last 20% (0.8% of the total beam power) is measured by a photodiode and is used as a trigger for the THz voltage bias.

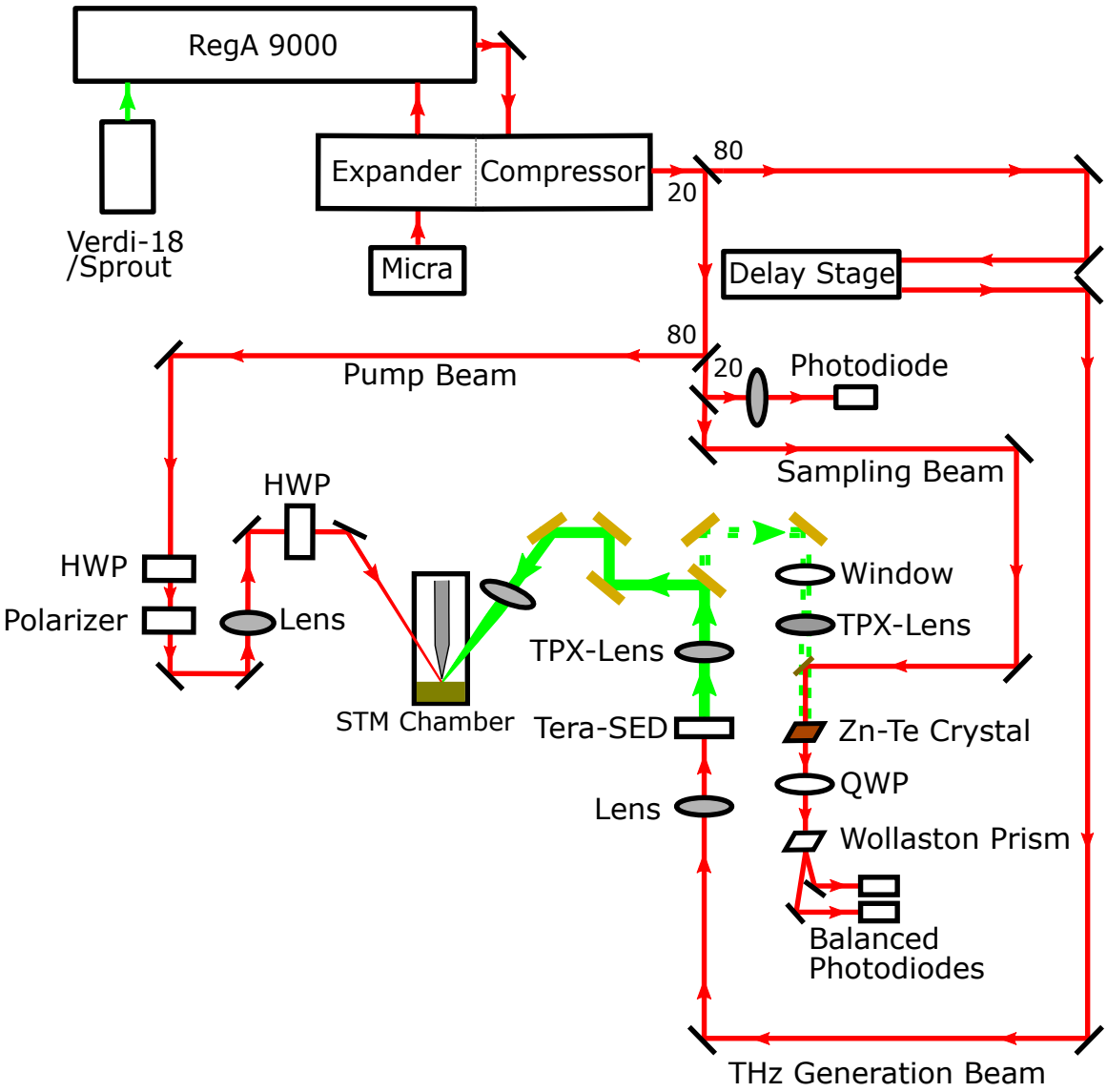

Figure 4.6: Complete laser setup schematic for the UHV THz-STM system. The beam is split into four different beams: the THz generation beam, pump beam, sampling beam, and trigger beam. A flip mirror in the THz beam path (green line) allows the THz beam to be onset to the electro-optic setup for THz pulse detection (green dashed line).

The three other beams are then onset to the UHV-STM system (Fig. 4.7). The pump beam passes through a half-wave plate (HWP), polarizer, HWP configura-

tion. The first HWP is placed into a rotational stage so that the polarization of the pump beam is controlled remotely. The polarizer only allows s-polarized light to pass through the medium. Thus, the intensity of the pump beam will diminish at different polarizations, allowing for remote control of the pump power. The second HWP is also set into a rotation stage. This time, without a polarizer, the polarization of the pump beam can be controlled remotely. The lens before the second HWP allows the pump beam to be focused onto the tip-sample junction.

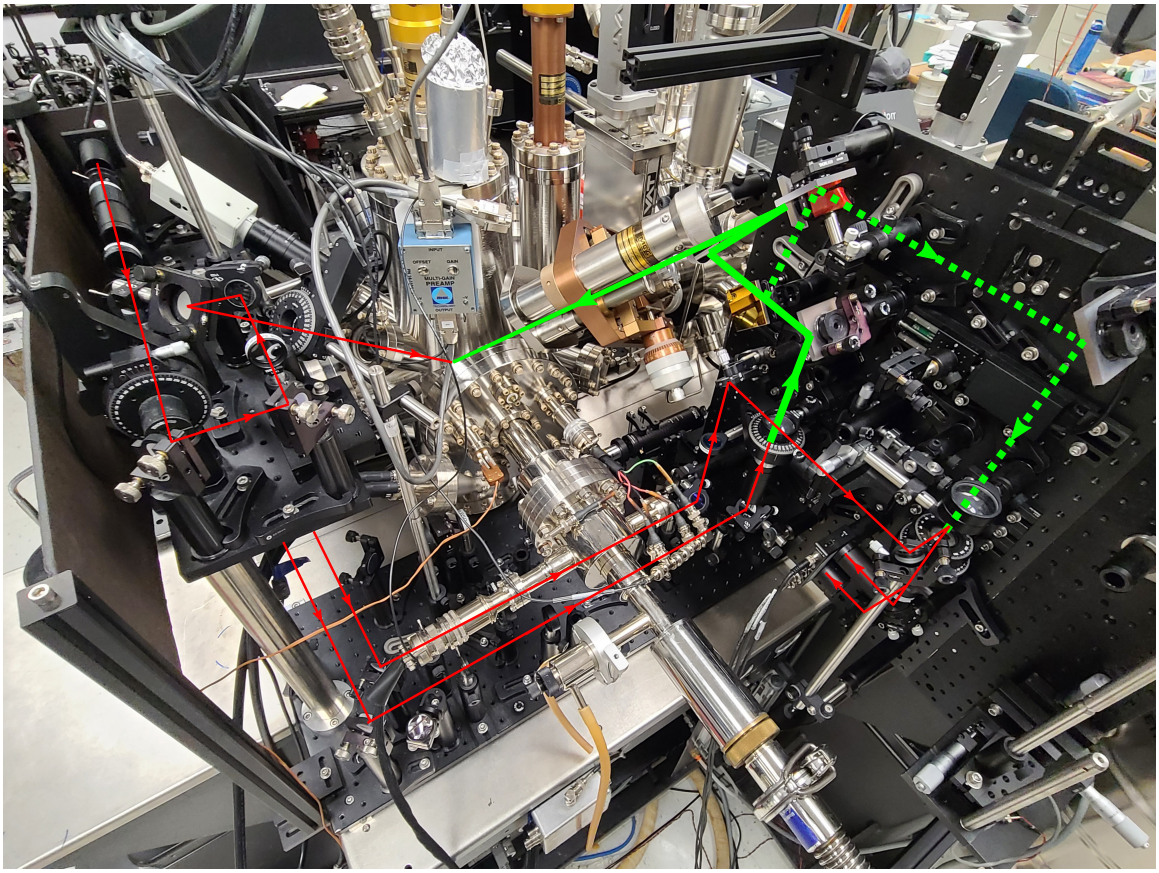

Figure 4.7: Photo of outside the STM chamber with the optics in place. The green line signifies the THz beam path. The dashed green line is the path for electro-optic sampling.

The THz generation beam is focused onto the photoconductive THz source (Tera-SED, Laser Quantum). The source is a GaAs type emitter with interdigitated electrodes. The source is placed into a rotation stage to control the polarization of the output THz pulse. A polymethylpentene lens (TPX lens, Menlo Systems) is used to

collimate the THz beam. The beam is then onset to the STM system, where it is focused by a TPX lens before passing through the UHV-STM window and onto the tip-sample junction.

A flip mirror is used to divert the THz beam path to the electro-optical sampling (EOS) configuration. The THz beam first passes through a small window of fused-silica to emulate the UHV-STM window. Then, a TPX lens focuses the THz beam onto a ZnTe crystal. The sampling beam is also onset to the ZnTe crystal for proper EOS measurements. The probe beam is then passed through a quarter wave plate (QWP) to create circularly polarized light, a Wollaston prism to separate the horizontal and vertical components of the circular light, and each of those beams are read by balanced photodiodes to calculate the THz electric field (see section 3.2, Eq. 3.11).

4.5 STM Operation

During STM operation, the sample stage and sample holder are biased while the tip is virtually grounded through a current preamplifier (IVP-200, RHK). This preamplifier converts the low signal from the tunnel current to a readable level for the control electronics. The IVP-200 has a gain of 10^8 with a bandwidth of 50 kHz. The voltage bias and current setpoint are controlled using the control panel (SPM 1000, RHK). A feedback loop with a circuit gain of approximately 1 kHz coupled to the z piezo is used to keep the current or height constant during a scan. Gain and time constant controls allow tuning of the feedback loop gain. The current setpoint sets the current for the feedback loop. Thus, a higher current setpoint will mean a smaller tip-sample distance.

In a topography scan in constant current mode, as the tip scans across a sample the change in height due to the surface features will in turn change the value of the tunneling current. This current is measured through the feedback loop, which will send a signal to the z piezo in order to adjust the height of the tip to return to the

current setpoint value. The height change and the current is read into two channel windows using a computer program specific to the RHK system.

The current measured from the STM junction is also split to a low-noise voltage pre-amplifier (SR360, Stanford Research Systems) that uses a low-pass filter. During THz-STM, there is both a d.c. component and THz induced component to the total measured current by the feedback loop (see section 3.3). This low-pass filter allows solely the d.c component of the current to be read given the high-frequency modulation of THz generation explained later in this section. This d.c current is read into a channel window by the computer software.

I-z spectroscopy uses the same configuration as a regular STM topography scan. The tip begins stationary above the surface of the sample, and the initial height of the tip is set via a current setpoint. The feedback loop is then disabled. Then, the tip is retracted and the current is measured simultaneously. Given the feedback loop is disabled, the tip will not return to its initial position, allowing the relative height change of the tip to be measured with the tunneling current. I-V curves also have the feedback loop disabled, the difference being voltage is changed rather than the tip height.

Conductance measurements (dI/dV curves) are taken simultaneously using a lock-in amplifier (SR830, Stanford Research Systems) by modulating the bias using a sine-wave voltage. The frequency of the bias modulation is set above the bandwidth of the feedback loop, allowing the height of the tip to not be affected by the bias modulation. The phase of the lock-in amplifier is chosen such that capacitive components are maximized, then changed by 90°. This allows the resistive component, the component localized at the tip-sample junction, is the only measured component. Then, the voltage amplitude is chosen such that the voltage effects are small yet noticeable, generally matched to the voltage step-size of the I-V scan. The output value of the lock-in amplifier is read through to a conductance channel in the STM software.

4.6 THz-STM Operation

The THz generation bias for the photoconductive antenna is modulated using a square wave from a function generator (BK4052, BK Precision) set to a frequency of 5.077 kHz. The frequency is set such that it is below the bandwidth of the IVP-200 preamplifier and above the bandwidth of the feedback loop. This allows for the changes due to the THz induced current to affect the feedback loop to avoid tip crashes but to mostly bypass the IVP-200 preamplifier. To measure the THz induced current, a lock-in amplifier (SR830, Stanford Research Systems) set to the modulation frequency of the THz bias reads the signal from the STM system and outputs the current value to a THz-current channel in the STM software.

Taking THz-STM scans require a low d.c current setpoint to observe the changes by the THz induced current while scanning. The THz electric field should also be minimum to avoid any surface destruction. Thus, $I_{THz} - E_{THz}$ measurements are taken to observe the amount of THz induced current, I_{THz}, with respect to the amplitude of the onset electric field, E_{THz}. A power supply (9122A, BK Precision) is used to change the bias voltage across the interdigitaged contacts of the photoconductive antenna, allowing for control of E_{THz}, while the I_{THz} is measured from the lock-in amplifier as outlined above. The feedback loop remains active during this scan to ensure a constant tip-surface distance. With the $I_{THz} - E_{THz}$ data, it is possible to select a suitable THz electric field for THz-STM measurements.

A final aspect of the THz-STM system is the ability to perform optical pump-THz probe measurements. The usual configuration has the peak of the THz and pump pulses arriving simultaneously to the tip-sample junction. Using a delay stage in the THz generation beam, it is possible to delay the arrival time of the THz pulse (Fig. 4.8). Given the value of E_{THz} also changes across the pulse, it is possible to then have a time resolved measurement of the surface dynamics of the sample.

These measurements can be done while the tip and sample are within tunneling

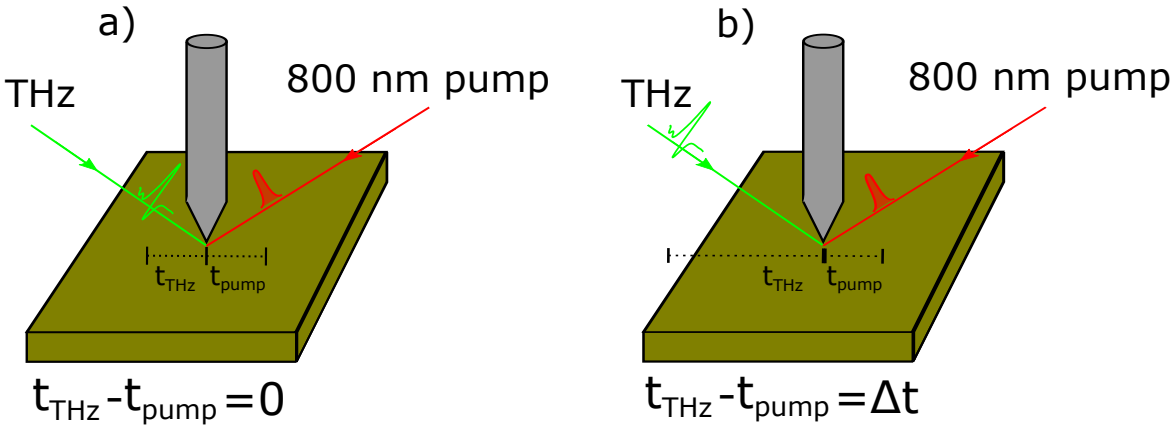

Figure 4.8: Schematic of an optical-pump/THz-probe measurement. The pump beam is used to excite carriers the sample while the THz is used as a probe to measure changes in the current caused by the excited carriers. a) The peak of the electric field of the optical pump is onset to the tip-sample junction at the same time as the peak of the THz electric field. b) The THz pulse is delayed such that the peak of the optical pulse arrives before the peak of the THz pulse. This delay in the peak-to-peak time allows for a time resolution measurement of the surface dynamics of the sample.

distance, much like an THz-STM scan. It is also possible to take measurements while the tip is retracted far enough away to be outside the ability for electrons to tunnel in normal STM mode. If the pump beam fluence is sufficiently high, photo-excitation of the electrons from the sample causes a current between the sample and the tip. This current can be read from the same channel as normal STM measurements. The THz pulse focused on the area between the tip and sample still allows for the THz induced current to be probed thanks to the delay stage.

Chapter 5

STM and THz-STM of $Bi_2Sr_2CaCu_2O_{8+x}$

High critical temperature (T_c) superconductivity is an ongoing area of study. The ability to cool the superconductor with liquid nitrogen to reach the superconducting T_c opened the field for potential commercial uses of superconductors. Particularly, bismuth strontium calcium copper oxide (BSCCO) is a family of cuprate superconductors with chemical formula $Bi_2Sr_2Ca_{n-1}Cu_nO_{2n+4+x}$, where n denotes the type of BSCCO and x is the amount of oxygen (hole-doping) in the material. Cuprate superconductors such as BSCCO contain copper oxide planes where superconductivity is believed to take place, separated by layers of charge-reservoir metal oxides [63, 64]. The n=1 case (named Bi-2201) has a low T_c of 7 K to 22 K based on oxide doping [65]. The n=3 case (Bi-2223) has a high T_c of 110 K, but is the most difficult of the three materials to synthesize [66]. By contrast, the n=2 case (Bi-2212) has a higher T_c of 95 K, leading it to be the more commonly studied material of the BSCCO family of superconductors. For scanning tunneling microscopy and spectroscopy, Bi-2212 is a good candidate to observe superconducting effects due to its high critical temperature and ease of cleaving.

The first Bi-2212 material was reported by Maeda et al. in 1988 [67]. After this discovery, many other studies were performed on the material, especially in the STM field due to the preferred cleaving plane of Bi-2212 being between the two BiO layers,

as shown in Fig. 5.1 [68]. This cleaving plane is due to the weak Van der walls force between the BiO layers in the unit cell. Although it is possible to cleave into the CuO layer below the BiO layer [68], the two layers can be distinguished by observing the topography of the surface in question [69]. The BiO layer is also non-metallic and has a band gap, meaning at probing biases within the BiO band gap the CuO_2 layer at 4.5 Å below the BiO layer is probed by the STM during spectroscopy (but not during topography scans) [70–72]. Thus, an STM can probe the superconductive CuO_2 layer even if the cleaving plane reveals a surface BiO layer.

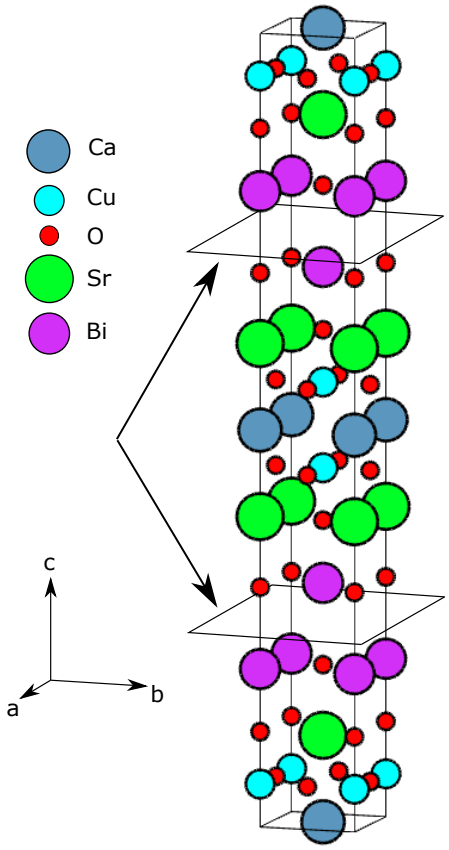

Figure 5.1: Unit cell of $Bi_2Sr_2CaCu_2O_{8+\delta}$ (Bi-2212) with lattice parameters a=b=0.38 nm, c=3.09 nm. Simplified unit cell created with VESTA [73] from crystallography data collected from [74]. The arrows point to the cleaving planes between the BiO layers.

According to Bardeen, Cooper, and Schrieffer (BCS) theory, an energy gap forms around the Fermi energy in the superconducting state. The value of this gap is

given by $2\Delta(0) = 3.52k_BT_c$ for conventional, weakly-coupled superconductors with $2\Delta(T)$ the superconducting gap energy and k_B the Boltzmann constant. For stronger-coupled superconductors, this ratio value can go as high as 4.6. Interestingly, if the typical $3.52k_BT_c$ value is used on Bi-2212, the expected 2Δ value would be 8.4 meV. The measured superconducting gap found for Bi-2212 is 2Δ=70-100 meV giving a much higher ratio at approximately $8k_bT_c - 12k_bT_c$ [75].

The superconducting gap is dependent on the critical temperature, which in turn is dependent on the material and the doping of the material (Fig. 5.2). The amount of doping, x, coupled with the amount of CuO_2 layers will also affect the superconductive gap [18]. This gap allows scanning tunneling spectroscopy (STS) of superconductors to observe the superconducting gap and allows some experimental insight into its behaviour. Conductance (dI/dV) spectroscopy measurements on semiconductors, s-

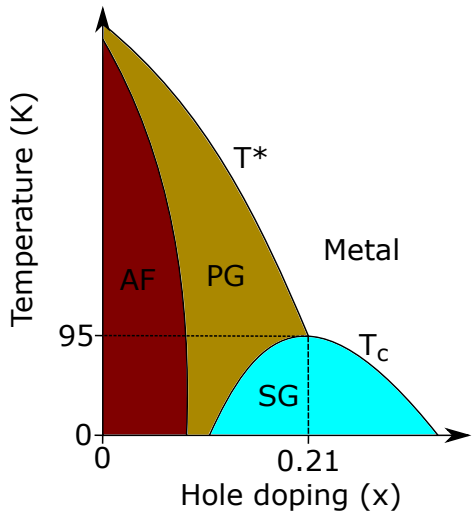

Figure 5.2: Schematic of the phase diagram for $Bi_2Sr_2CaCu_2O_{8+x}$, where AR is the antiferromagnetic phase, PG is the pseudogap phase, and SG is the superconducting gap phase. The T_c is the critical temperature line, while T^* is the pseudogap temperature line. The optimal critical temperature and critical doping values are denoted on their respective axes. The size of the axes are not to scale.

wave superconductors, and d-wave superconductors all have a different behaviour as schematically shown in Fig. 5.3. The s-wave conductance rapidly drops to zero at Δ, while for the d-wave superconductor the descent is slower and pointed. Both

superconductor conductance measurements show coherence peaks about the Δ superconducting gap energy below T_c. These coherence peaks denote a maximum pairing excitation, dependent on the amount of doping and sample temperature [76].

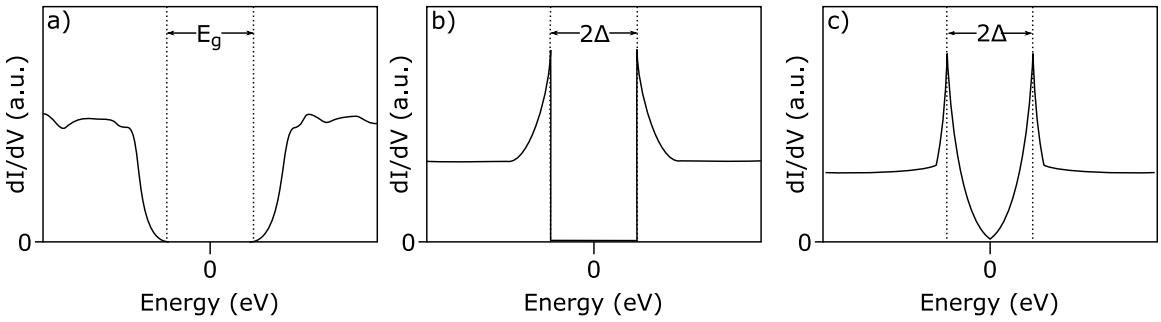

Figure 5.3: Schematic showing the theoretical shape of the conductance data as a function of energy (or tip bias) of a) a semiconductor with a band gap energy of E_g, an s-wave superconductor with a superconducting gap energy of 2Δ and a d-wave superconductor with a superconducting gap energy of 2Δ. The semiconducting and superconducting gap energies for each schematic is centered around the zero energy point. In b) and c), coherence peaks can be observed denoting the edges of the superconducting gap (dashed lines).

For temperatures used above the critical temperature a pseudogap forms around the Fermi energy of the system. This pseudogap is dependent on the doping and the sample temperature, much like the superconducting gap. This gap is still visible in the scanning tunneling spectroscopy given it is still smaller than the Bi-O gap at approximately 100 meV and 300 meV, respectively [71, 75, 77].

5.1 Sample Preparation

The Bi-2212 samples used in the following experiments were purchased from 2D Semiconductors and had approximate dimensions of 5 x 5 mm. The Bi-2212 sample was affixed to a thin aluminium disk using a silver UHV-safe epoxy (Epoxy Technology). The epoxy and the aluminium disk allowed for an electrical connection between the Bi-2212 sample and the bias lines of the sample puck. The Bi-2212 sample also required cleaving of the top-most bismuth layer. However, this cleave must be done in a UHV environment in order to minimize the possibility of contaminants and oxides

on the sample surface. To do this, one end of a thin copper wire was heated until a small ball was formed large enough to cover the surface of the sample. The ball was then flattened on the bottom to allow better surface contact with the sample. The other end of the wire was shaped into a hook. After allowing the end of the wire to cool, it was affixed to the sample surface using the silver epoxy, as shown in Fig. 5.4 a).

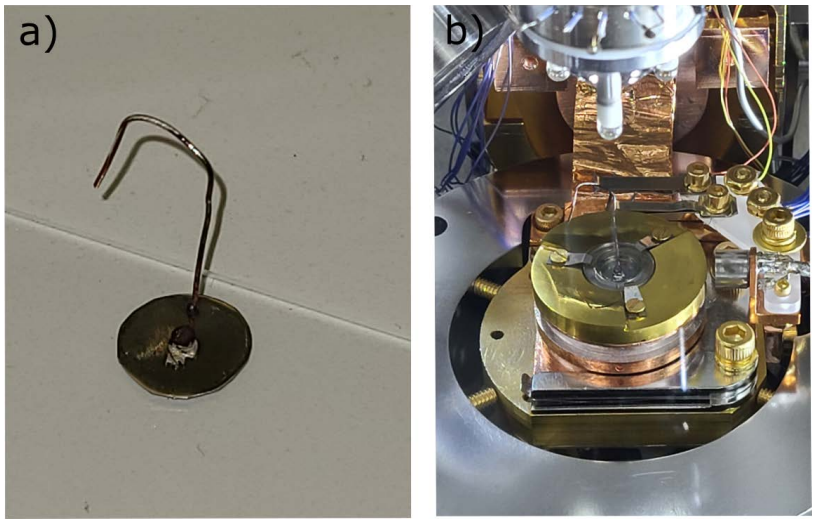

Figure 5.4: Bi-2212 sample mounted using a silver UHV-compatible epoxy, an aluminium base, and a copper wire. a) The basic setup with the copper wire 'balled' at the bottom for a larger surface contact with the Bi-2212 sample and the top of the wire bent for in-situ cleaving. b) The wire-sample setup from a) mounted on a sample puck and in the STM chamber ready for cleaving.

The sample was heated in the load-lock chamber for 12 hours at 120 °C in order to remove any possible organic contaminants on the surface or in the environs of the sample and sample puck. Once cooled, the sample was moved to the sample holder of the STM chamber as shown in Fig. 5.4 b). The sample and sample holder were then cooled to 100 K using liquid nitrogen in order to cleave the sample. The wobblestick of the STM was positioned such that the fork can make contact with the upper hook of the copper wire. With a little force to push the copper wire, the surface of Bi-2212 was cleanly cleaved in-situ (Fig. 5.5). The sample was then left to warm to room temperature for initial scans of the surface.

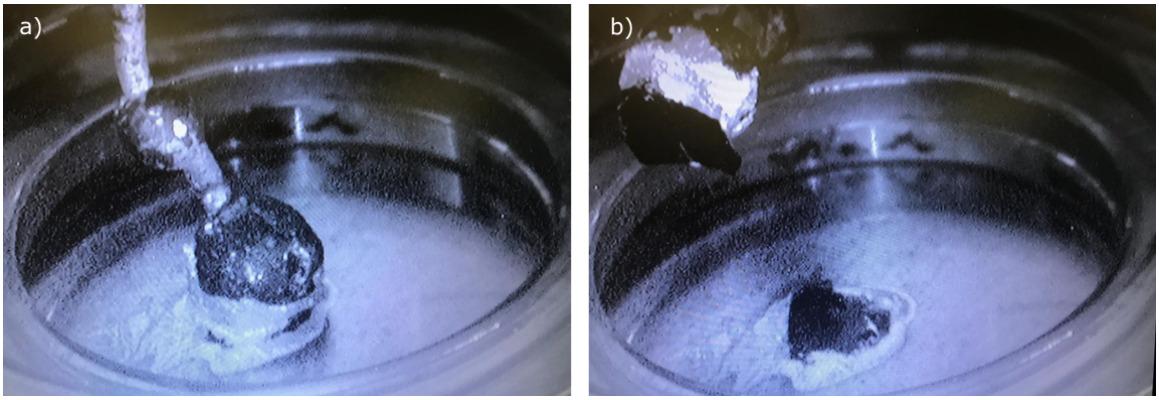

Figure 5.5: In-situ images of a) before and b) after cleaving using a thin copper wire and silver epoxy. The sample was cooled to 100 K prior to cleaving. A thin layer of the BSCCO sample can be seen affixed to the copper wire post-cleaving.

5.2 Topography

Topography scans were taken of the Bi-2212 surface at room temperature with a gold tip (Fig. 5.6). There are row-like zig-zag patterns across the surface that appear periodically across the surface. There are also large dark areas in the rows. The periodic rows are 2.3 $\pm$ 0.3 nm in width, in agreement with the 2.6 $\pm$ 0.15 nm value from literature [78]. The zig-zag lines between the rows shown in Fig. 5.6 were first believed to be caused by empty Bi sites on the surface [78]. However, the 'missing' Bi atoms are simply moved due to the sinusoidal behaviour of the rows. This behaviour is due to the oxygen atoms being shared by both the Bi atoms on the surface layer and the Cu layer below. Since the bond between Cu and O is stronger than the Bi-O bond, the Bi atoms will move to a more energy-favourable position in order to compensate for the stronger Cu-O bond. This causes strain from both compression and extension of the bond length, meaning the Bi atoms will also move to compensate for these changes in bond distance allowing for empty Bi sites [79].

Fig. 5.7 shows a closer, 5 nm x 5 nm image of the BiO surface of Bi-2212 taken at room temperature with a gold STM tip with scanning parameters of 1 V bias and current setpoint of 0.12 nA. The image shows bright spots periodic across the surface. These bright spots correspond to Bi sites on the surface, indicative of the

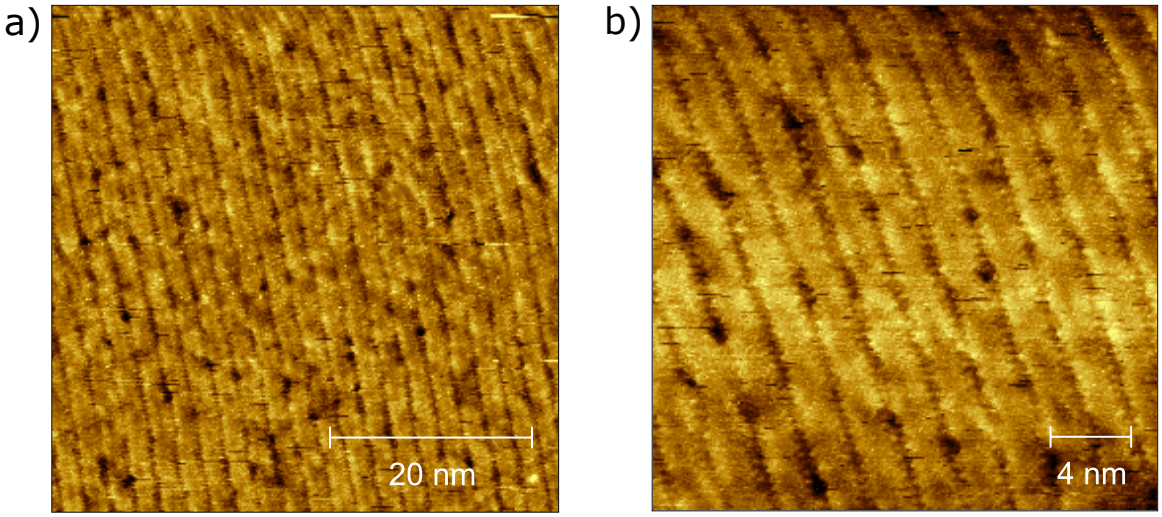

Figure 5.6: Topography images of BSCCO-2212. Images were taken using a gold tip at room temperature in UHV conditions with a bias voltage of 1 V and a current setpoint of 0.12 nA. a) is a 50 nm x 50 nm image showing the superstructure of the BiO layer, while b) is a 25 nm x 25 nm image of the same area. The slight bend at the top of each image is caused by a drift in the piezoelectronics of the scan head at the start of the scan.

cleaving plane of Bi-2212. The low-resolution of the Bi sites is due to the image being performed at room temperature, likely due to lattice vibrations. The Bi atoms are still expected to have a sinusoidal pattern that will be difficult to map with the unit cell alone. The spacing between the clear bright spots was measured to be 4.2 ± 0.2 Å which is consistent with a previous measurement of 4.1 ± 0.3 Å [78].

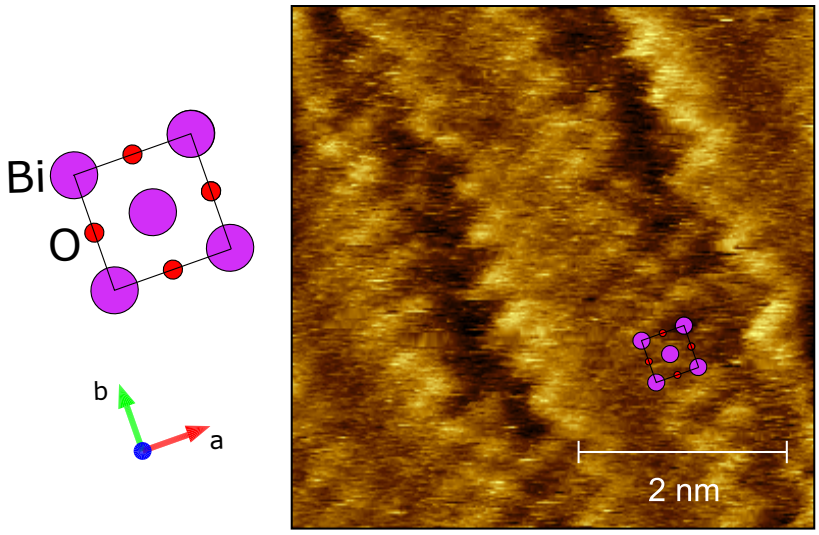

Figure 5.7: 5 nm x 5 nm image of the BiO layer of BSCCO-2212. The topography scan was taken at room temperature under UHV conditons with a gold tip, a bias voltage of 1 V, and a current setpoint of 0.51 nA. The Bi-O plane of the unit cell with a-b-directionality is placed on the left of the image for reference, while a to-scale plane is placed on the image as a guide to the eye for atomic resolution. The b-axis is parallel to the dark rows [78, 79].

5.3 Spectroscopy

I-V and dI/dV curves were taken simultaneously on the surface of BSCCO with a tungsten STM tip. The dI/dV (conductance) curves were taken using the bias-modulation method. Conductance measurements of Bi-2212 were performed at 100 K using liquid nitrogen (Fig. 5.8 a)) and at 55 K cooled by liquid helium (Fig. 5.8 b)). Features in the 100 K cooled data are not obvious. In contrast, the Cu-O semiconducting gap is more pronounced in the 55 K measurement. The expected Bi-O gap is not visible in either measurement. The two measurements were performed on different days. The step size of the 55 K measurement was decreased in order to resolve the features. The BiO gap and Cu-O pseudo gap are expected to be approximately 300 meV and 100 meV, respectively [71, 75, 77]. The value of the Cu-O pseudo gap matches the value expected from literature. However, the expected pseudogap and BiO gap values in the 100 K conductance measurement are not visible, likely due to

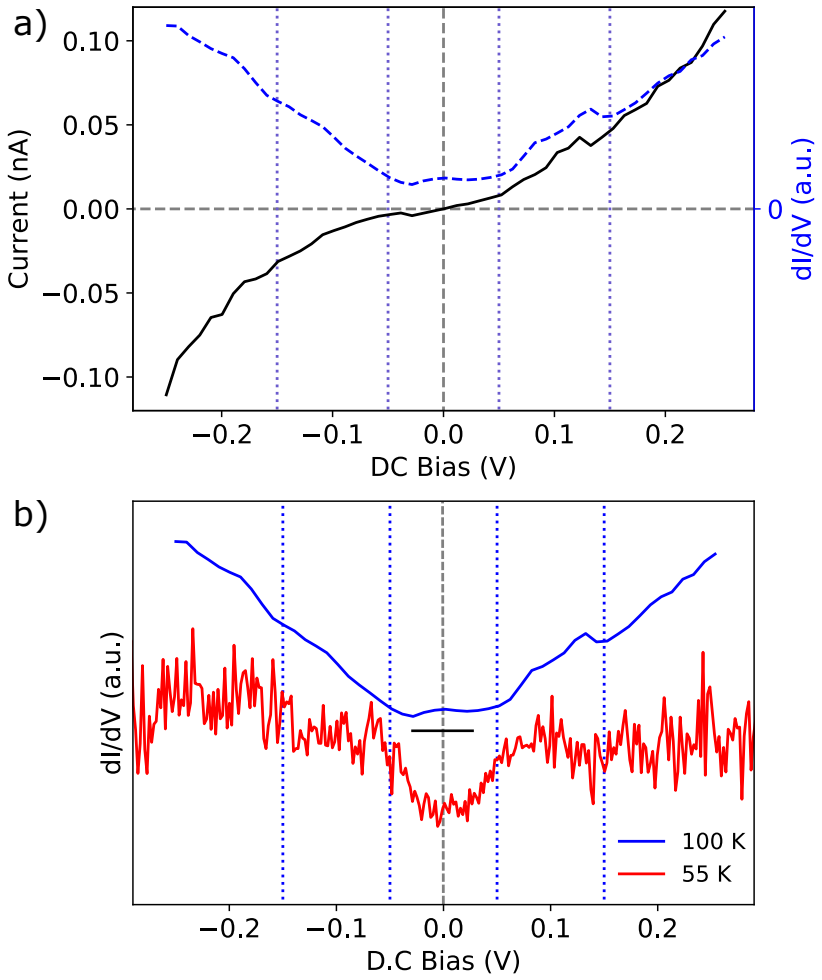

Figure 5.8: a) I-V (black solid) and dI/dV (blue dashed) curves taken at a bias voltage of 1 V a current setpoint of 40 pA with a voltage range of -0.25 to 0.25 V at 100 K sample temperature. b) Comparison between dI/dV curves taken at 100 K (from a)) and taken at 55 K. The blue dashed lines in both figures correspond to the BiO gap and Cu-O pseudogap of 300 meV and 100 meV, respectively. The black horizontal line represents the zero of the 100 K data, while the zero of the 55 K data corresponds to the bottom of the graph.

noise in the measurement. This noise can arise primarily due to thermal drift from cooling the sample. Given the feedback loop is off, any heat transfer between the sample and the tip will cause the sample to expand or retract, and thus the cause the tip-sample distance to change between measurements. I-V measurements with a smaller voltage step size may also resolve the missing features in both the 100 K and 55 K measurements. It is also important to note that the dI/dV conductance curves were not normalized using the I-V curve as is conventional, as this introduced undesirable numerical anomalies around V_{DC}=0 V. Instead, it was simply normalized to unity.

Expected is a sharper increase about the pseudogap gap lines in the spectra given the temperature of the sample. The 55 K measurements are indeed sharper than the scan at 100 K. It has been shown at higher sample temperatures the gap peaks starts to soften, indicative of a loss of the superconducting state [80]. The Bi-O gap expected is not visible, likely due to the noise from the conductance scan. Further experimentation with different current setpoints (tip heights) as well as different scanning parameters could achieve better resolution of the two gaps.

The I-z curve in Fig. 5.9 shows four measurements taken using a tungsten STM tip. The apparent barrier heights were calculated using equation 2.21. We see that although the data was taken using the same 0.1 V bias voltage and 100 pA current setpoint, the values for the apparent barrier height vary from 0.95 eV to 1.74 eV, leading to an average value of 1.4 $\pm$ 0.4 eV. This average does not agree with the value found by Sugimoto et. al. of 5.3 $\pm$ 0.4 eV [81]. This could be due to the stability of the tip with respect to the sample surface, causing the distance-current response to also be unstable. It is also possible the tip was not close enough to the sample during the initial stages of the acquisition. Using a higher current setpoint and a lower bias voltage would allow the tip to begin closer to the sample. Finally, the sample used in this work was purchased long before the results of this study, leading to the possibility of degassing of the doping oxygen from the sample over time in the

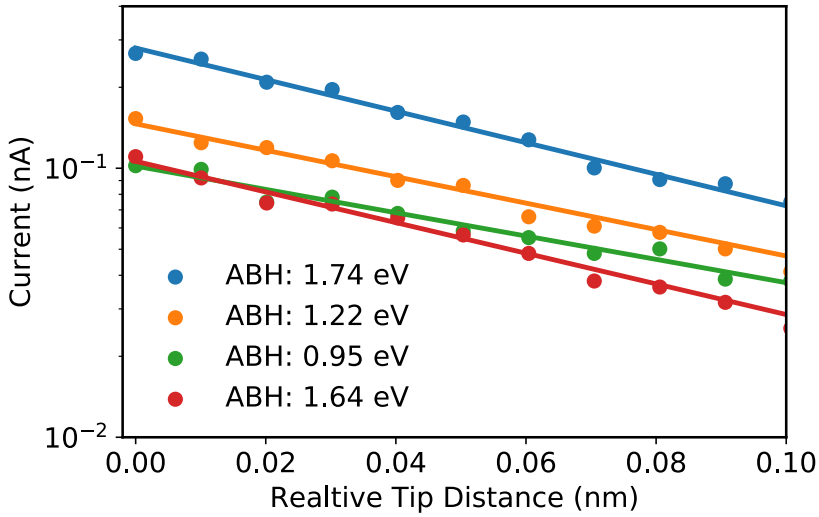

Figure 5.9: I-z curves of the BiO surface of BSCCO-2212 at 100 K with a W tip. The tip height was kept constant prior to measurements with a bias of 0.1 V and a current setpoint of 0.1 nA for each measurement. The apparent barrier heights (ABH) of each slope were calculated using Eq. 2.21.

UHV system.

5.4 THz-STM of the Bi-2212 Surface

THz-STM was performed on the BSCCO surface at 100 K using liquid nitrogen and with a tungsten STM tip. Fig. 5.10 shows the measured THz-induced current as a function of the electric field at the peak of the THz pulse in the tunneling regime. The height of the tip was kept fixed by turning off the feedback loop at a setpoint of 100 pA and bias voltage of 0.4 V. The I-E curve provides a measure of the THz electric field required for a THz current response from the sample. The electric field is increased until a sharp signal is observed. This allows for a choice of low electric fields to avoid possible damage to the sample surface. In this case, the onset of the I-E curve begins at 200 V/cm THz field.

Fig. 5.11 shows preliminary results of a THz-STM scan using the 200 V/cm THz peak electric field determined by the I-E curve in Fig. 5.10 in a 20 x 20 nm window. The scan speed was calculated such that the lock-in time constant was synced with the number of pixels per line to achieve the three images simultaneously. The topography

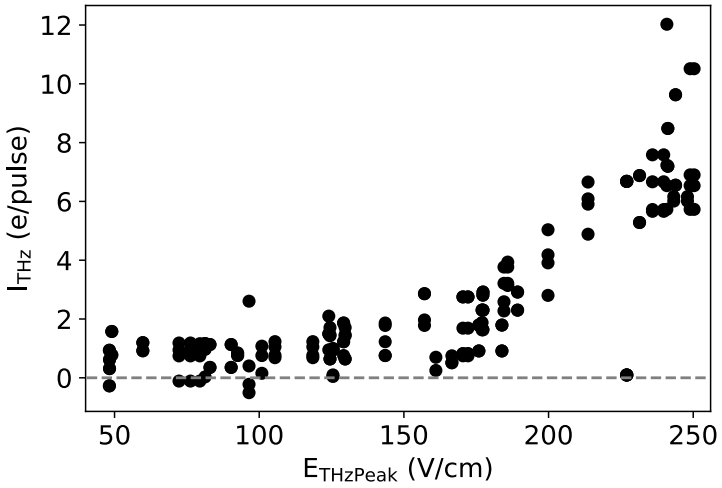

Figure 5.10: THz-STM $I_{THz} - E_{THzPeak}$ curve on the BSCCO surface. The curve was taken at 100 K with a W STM tip. The DC current was constant with a current setpoint of 100 pA and a tunnel bias of 0.4 V.

image shows the zig-zag pattern of the BSCCO surface. However, the DC current channel shows a shadow of the topography image. Since the feedback loop was set to constant current mode, it is expected that the DC current channel remain constant over the scan. A reason for this stems from the gain and time-constant settings on the feedback loop. As the tip approaches a feature such as a step edge, the DC current measured by the STM head will increase, signalling a change in height to compensate for the DC current setpoint. At a low gain, the feedback loop takes longer to adjust, and thus a shadow of the topography appears on the DC current channel. Although this DC bias shadow should not appear in the THz current channel given the THz current is measured via lock-in detection, the frequency from the change in the feedback loop could be enough to cause a false-signal in the THz current channel that is larger than the small THz currents expected.

5.5 THz-Induced Surface Damage

Damaging the surface of a sample of interest could prove useful in sample experiments, specifically composite materials with large unit cells. It is possible to cleave the surface

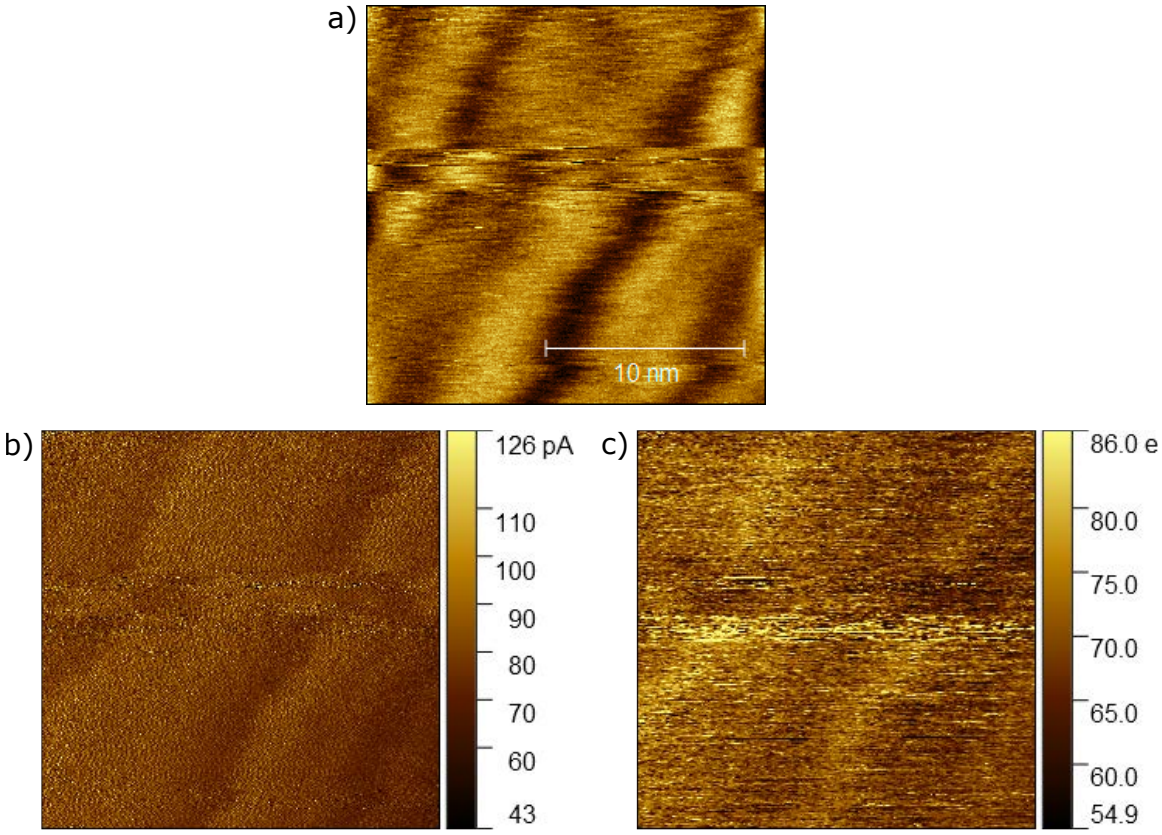

Figure 5.11: THz-STM of the BSCCO surface showing a) Topography channel, b) DC current channel, and c) THz induced current channel. Scanning parameters are 0.4 V bias, 100 pA setpoint, and a peak THz electric field value of 200 V/cm. The center of the image is smeared likely to a change in the tip surface during scanning.

of a sample with high electric fields due to high current densities. Fig. 5.12 a) shows the Bi-2212 sample prior to high THz fields, while Fig. 5.12 b) shows the damaging effects caused by a static STM tip with a THz electric field peak of 600 V/cm.

The surface changes from the typical superstructure expected for the BiO layer of BSCCO to a surface filled with defects. Unfortunately, a smaller window scan was not possible due to bad resolution of the image likely caused by tip deformities from the damage caused on the surface. This damage could prove useful to observing the planes under the BiO surface. As stated previously, the typical cleave plane is that of the BiO layer. Meanwhile, the superconductivity arises in the CuO layer found beneath the surface of the BiO layer in the unit cell. High THz fields coupled to the STM tip could expose the lower Cu-O layer and would allow a direct surface

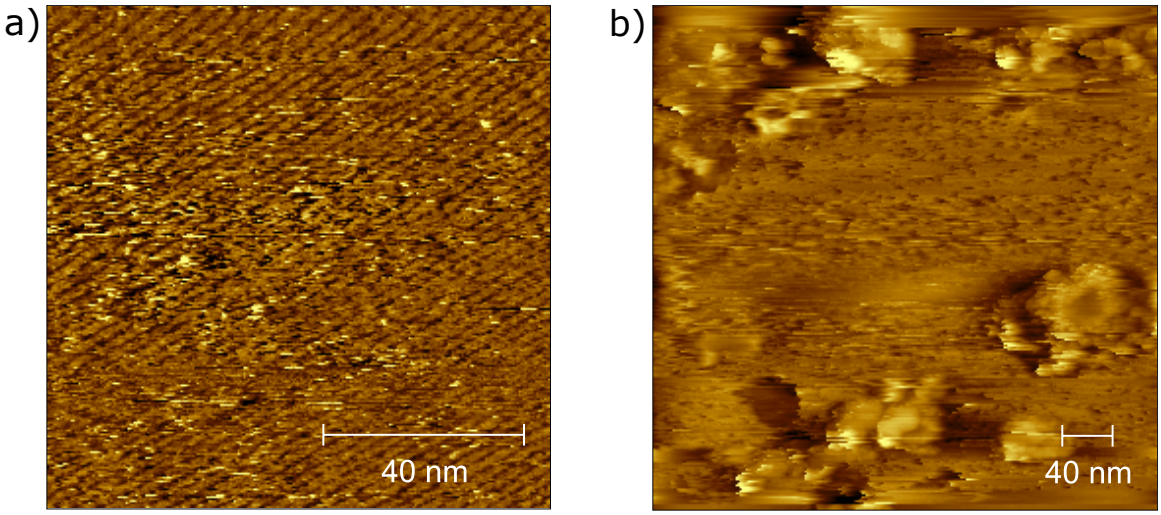

Figure 5.12: Determining surface damages to Bi-2212 caused by high THz electric fields. a) The surface before is clean with the superstructure visible. b) The surface has nanometer sized holes caused by the THz electric field coupled to an STM tip while tunneling.

measurement of that layer. This would also allow a comparison study using a step edge between the two layers of the crystal and the ability to possibly observe and simultaneously compare the dynamics of the two layers [82].

Chapter 6

STM of Au(111)

Gold is a transition metal from the group 11 family of the periodic table. Gold is also a noble metal with a naturally occurring face-centered cubic structure (FCC) in bulk with a lattice constant of 4.08 Å [83, 84]. One of the first reported STM measurements of Au(111) deposited on Mica were performed by Hallmark et. al. in 1987 [85]. Since then, it has been used as a substrate for multiple STM experiments due to its stability in air and vacuum, its closed-packed structure, and that it is easy to prepare a flat surface for deposition [86]. Gold is also an interesting STM subject due to its surface reconstruction, one of the only FCC metals to exhibit such a surface effect [87].

6.1 Au Deposition and Preparation

Gold was deposited on a thin Mica substrate in a vacuum deposition chamber using an evaporation technique. Mica grade V1 (Ted Pella, Inc.) was used as the deposition substrate. The gold was evaporated under a vacuum of $2\text{x}10^{-6}$ torr and at a rate of 0.2 nm/s until an approximate thickness of 50 nm was deposited. Then, before mounting the sample into a sample puck, the surface was flame annealed using a hand torch for one minute to smooth the surface. The sample was then placed unto a sample puck and put into the load-lock chamber of the STM system where it was baked for 12 hours at 120 °C to remove any organic materials that may be present on the sample

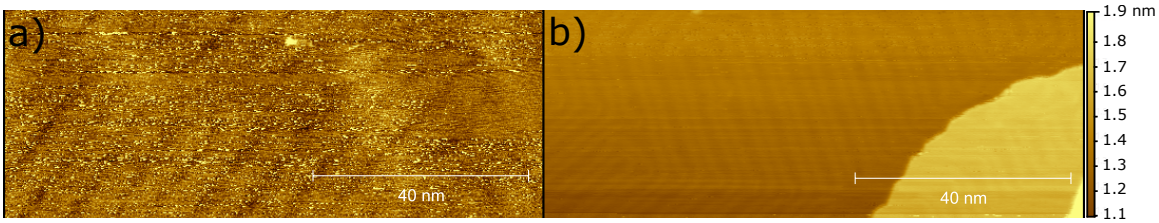

Figure 6.1: a) Before and b) after two rounds of Ar bombardment and annealing. The effects of the annealing cycles show a cleaner surface with a better resolution of the surface features. The two images were performed on different areas of the same gold surface. The scale bar on the right corresponds to the relative surface height in b).

or the sample puck.

In-vacuum preparation was also completed in the preparation chamber of the UHV-STM system. The sample was first argon bombarded at a 30° angle of incidence onto the sample for 30 minutes. Then the argon was evacuated and the sample was annealed at 400°C for 40 minutes. After a 20 minute cooling period, the sample underwent nine more cycles of Ar bombardment and annealing. An example of the gold surface before and after annealing is shown in Fig. 6.1. It is difficult to scan the same region after the sample is removed for annealing, thus the surface topography is different. However, the surface is cleaner and more compatible with higher resolution scans.

6.2 Surface Reconstruction of Au(111)

Topography scans were performed on the gold surface using a gold STM-tip at 100 K as shown in Fig. 6.2. Both images show the herringbone type reconstruction surface indicative of Au(111). This herringbone reconstruction is attributed to a stacking fault of the topmost gold layer induced by surface elastic strain [88]. This surface strain causes a second structure, hexagonal-closed-packed (HCP), to appear in between two domain walls. These domain walls are the bright, parallel lines seen across the gold surface, and denote the transition between the FCC stacking and the HCP stacking. Given the energetically favourable stacking of FCC in bulk gold, the

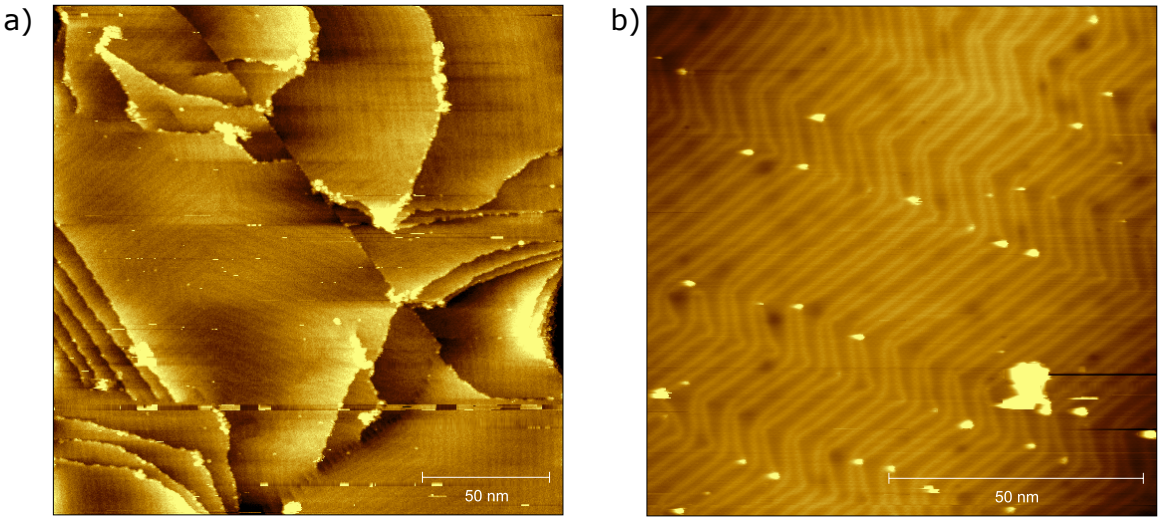

Figure 6.2: a) 200x200 nm and b) 100x100 nm topography images of Au(111) at 100 K using an Au tip. Scans were performed using a voltage bias of 1 V and a setpoint of 0.4 nA. The herringbone structure of the reconstructed surface of the gold is indicative of a clean Au(111) surface.

FCC region of the surface is larger than the HCP region. Two different forces cause the bending of the domain walls. There is a long-range stress on the surface that favours a contraction, while a more local stress favours a uniaxial contraction [87].

Fig. 6.3 shows a single line topography scan across the herringbone structure in Fig. 6.2. The length of each pair of peaks, the domain-HCP-domain region, was measured to be 5.8 ± 0.2 nm, corresponding well with a previously measured value of 6.3 nm from [88]. The height of the peaks from the corresponding valleys was found to be 0.14 ± 0.03 Å aligning well with previous experimental values of 0.15 ± 0.04 Å from [89] and 0.20 ± 0.05 Å from [88]. The individual peak-to-peak distances for the domain walls, the HCP region, have a measured distance of 2.2 ± 0.2 nm while the length of the larger valleys, the FCP regions, correspond to a distance of 3.6 ± 0.2 nm. Previously recorded values of the HCP region and FCC region are 2.7 to 2.9 nm from [88] and 2.2 nm and 4.4 nm from [89], respectively. Also, DFT calculations performed by Hanke et al. have lengths of 2.8 nm for the HCP region and 3.8 nm for the FCC region [90].

Of note in the images are what seem to be surface anomalies appearing as bright

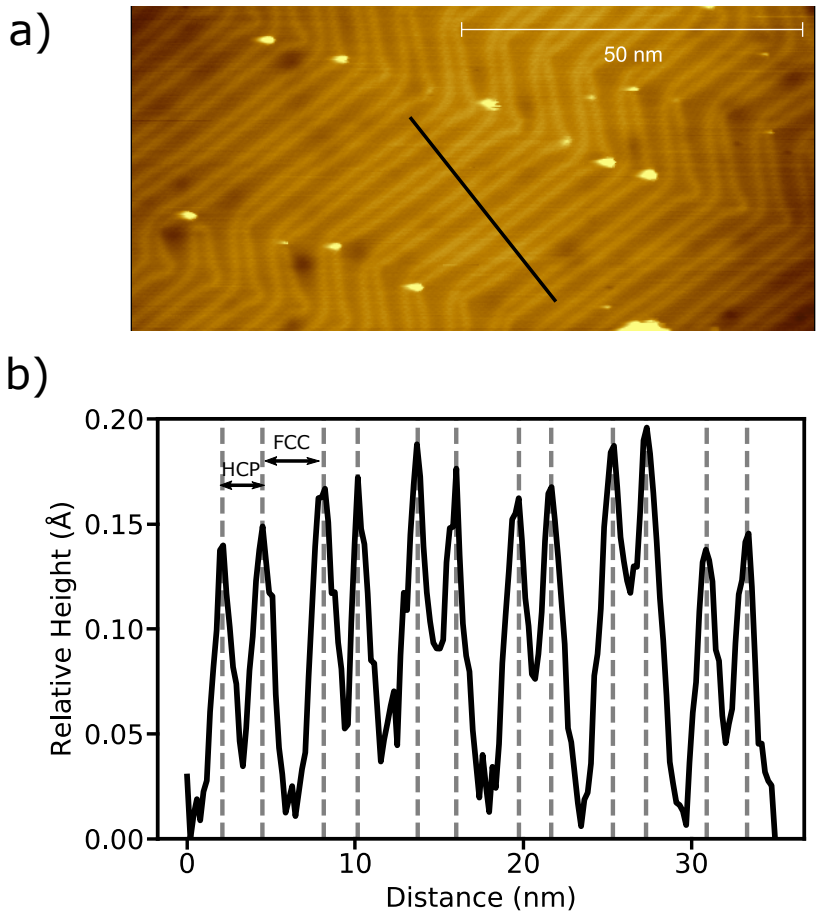

Figure 6.3: a) A cropped image from Fig. 6.3 b). The black line in the image is a line scan across the surface. b) The resulting topography scan with the peaks denoted by dashed grey lines. The HCP and FCC regions of the herringbone reconstruction are shown, with the peaks being the domain walls between the two regions.

spots in the topography scans. These spots are likely due to surface contaminants on the gold or extra gold atoms at the surface that cannot 'fit' into the surface reconstruction space. The kinks in the herringbone structure have been known as nucleation sites due to the inhomogeneity of the FCC-HCP lattice sites [91]. This can be explored further with sub-monolayer deposition on the herringbone surface.

Another interesting feature of the herringbone reconstruction of the Au(111) surface is the tensile reconstruction around new surface defects. Fig. 6.4 shows STM images before and after the STM tip came into contact with the gold surface. Before, the surface topography has the typical structure. Once the tip came into contact

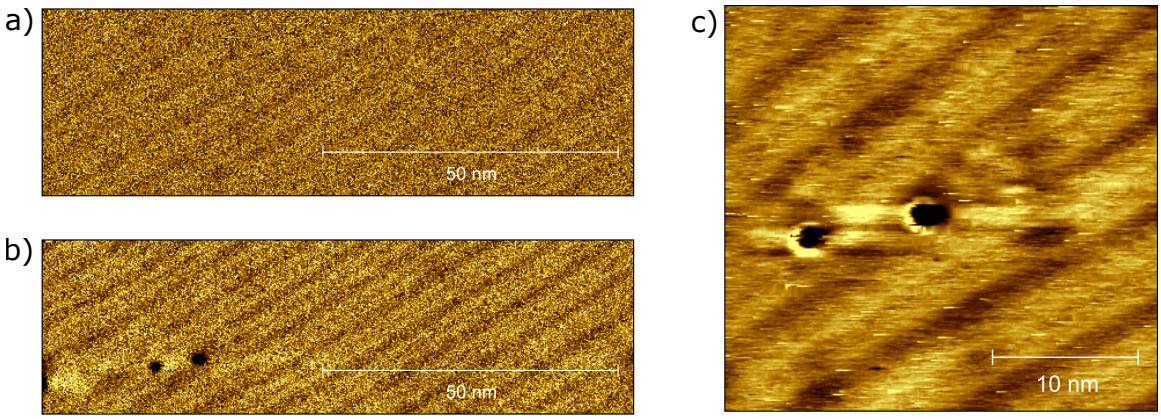

Figure 6.4: Effects of new surface defects on the herringbone structure of Au(111). a) Au(111) topography scan prior to the introduction of a surface defect. b) The same area as a) after the tip made contact twice to the surface. c) A smaller region scan of the defect area. The herringbone pattern changes around the introduction of the new surface defects.

with the surface, new sample defects (holes) were introduced. The herringbone pattern then deviated from its original path and adapted to these new defects. It would appear that the segment where the herringbone structure meets the defect ends and buckles, and the segments surrounding the defect alter their path. This is due to the defect creating some stress relief on the surface. Scans over a longer period of time would show these holes either changing position relative to their surroundings or disappearing entirely due to the diffusion of the Au atoms [92]. Effects at a farther distance could also be expected, such as newer kinks in the structure, but this was not observed in this study.

6.3 Surface Spectroscopy on the Au(111) Surface

Spectroscopy on the gold surface was performed using a tungsten tip at 100 K. Fig. 6.5 a) shows the I-V and dI/dV (conductance) curves taken from -0.5 to 0.5 V bias with the tip height set from a voltage bias of 0.4 V and current setpoint of 50 pA prior to the feedback loop being deactivated. The conductance curves were taken using the bias modulation method outlined in section 2.4.

Previous experiments on the conductance of gold were performed by Davis et. al

[93]. In their experiment, they observe the same energy shift towards the positive voltage. However, they also observed a peak at -350 mV. This peak is due to a Shockley state of the surface of the gold, and is expected to extend across a large area. Also, this feature is amplified close to a step-edge or a defect [94]. It is possible that this feature appears through the noise floor of the conductance curve. Taking curves with a more localized bias range about the suspected region would likely show this Shockley state on the surface.

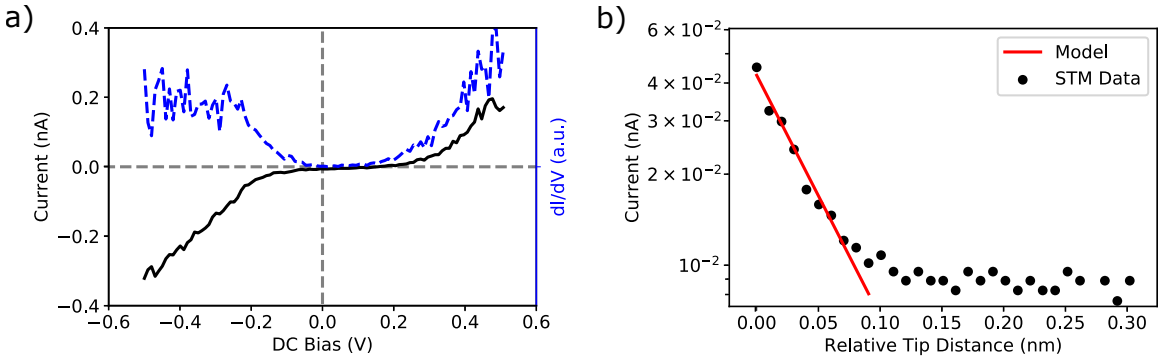

Figure 6.5: Scanning tunneling spectroscopy performed on the gold surface. Spectroscopies were performed at 100 K using a tungsten tip. a) I-V curve (black, solid line) and corresponding dI/dV curve (blue, dashed line). Initial tip heights were determined using 1 V bias and 50 pA setpoint. b) I-z curves of the gold surface. The initial tip height was set by a bias voltage of 0.4 V and a current setpoint of 50 pA. The black dots correspond to the experimental data while the red line corresponds to the model from equation 2.21. The calculated apparent barrier height is 3.2 ± 0.2 eV.

Fig. 6.5 b) shows the I-z curve taken at the surface of the gold sample using a tungsten tip. The data is plotted on a semilog axis to match the model from Eq. 2.21. The noise floor from the pre-amplifier is visible as the tip distance increases. This noise floor matches the manufacturer specifications for the pre-amplifier. The data on the noise floor were not used in the calculation of the apparent barrier height. A low bias voltage of 0.4 V was used for the measurement with a current setpoint of 50 pA. The data shown is an average of 5 curves taken at the same position on the sample. The apparent barrier height was found to be 3.2 ± 0.2 eV. Although the workfunction for gold is approximately 5.1 eV, the apparent barrier height may be

different due to reasons outlined in section 2.4. Nevertheless, the reported value in this work corresponds poorly with a previously reported value of 2.5 eV [88].

The apparent barrier height is dependent on the tunneling parameters, as well as the tip material. A barrier height of 1.85 eV was reported using a tungsten tip with tunneling parameters of 50 mV and 0.46 nA [95]. For a gold tip, a barrier height of 1.9 $\pm$ 0.2 was found using 0.5 V and 50 pA [96]. An attempt was made to determine the apparent barrier height with gold STM tips. However, the results were inconclusive. It would be prudent to do a similar study based on the tip-sample distance with different STM tips.

It has also been reported that the value of the apparent barrier height will lower by a value of 0.3 eV based on the location of the tip due to the herringbone structure [95]. They attributed this change to electric dipoles that arise on the dislocations. By modulating the tip during a scan and reading the output change in tip height through a lock-in amplifier, they were able to map the apparent barrier heights over the scanned surface. The ability to determine the apparent barrier heights in such a fashion would give good insight into the behaviour of the surface at areas such as step-edges and surface defects.

It is also possible to compare ABHs from different metals given their close work functions. Yang et al. reported the ABH of copper using a tungsten tip with similar I-z parameters of 0.5 V bias and 50 pA current setpoint using the same system as this study [40]. In their study, the ABH of copper was reported to be 4.2 eV. Given the work function of gold is 5.1 eV and the work function of copper is 4.7 eV, and both measurements used a tungsten tip, a difference between the ABH values are on the order of half the difference of the work functions is to be expected. The difference comparing this study to Luo is 1 eV, outside the expected value of 0.2 eV.

Chapter 7

THz-STM of Ag-coated Au(111)

Much like gold, silver is a transition metal from the group 11 family in the periodic table. Also similarly, the bulk silver crystal lattice is face-center cubic (FCC). One of the main differences between silver and gold is the surface of silver does not reconstruct, allowing it to be a suitable substrate for materials without extra chemical preparation to achieve an atomically flat layer [87].

7.1 Sample Preparation

Silver was deposited in the preparation chamber of the STM using an evaporation technique similar to that of section 6.1. The substrate used was the gold substrate observed in Chapter 6 due to the clean, flat surface indicated by the herringbone structure. The deposition was done at a pressure of $< 1\text{x}10^{-8}$ torr at a deposition rate of 0.1 Å/second until roughly 3 nm of material was deposited. The silver was then annealed at 250°C for 15 minutes using the transfer arm and filament heating technique.

7.2 Topography

Topography scans were performed on the silver surface at 100 K using a tungsten tip with scanning parameters of 1 V bias and 0.35 nA current setpoint. Fig. 7.1 a) shows a 200x200 nm window, where the silver has deposited as mounds of varying height as

opposed to a flat surface. Fig. 7.1 b) shows a 100 x 100 nm scan window using the same scanning parameters of a step edge. It appears that the herringbone structure of the gold sample from chapter 6 has been replaced with mounds and valleys with no visible herringbone reconstruction on the surface.

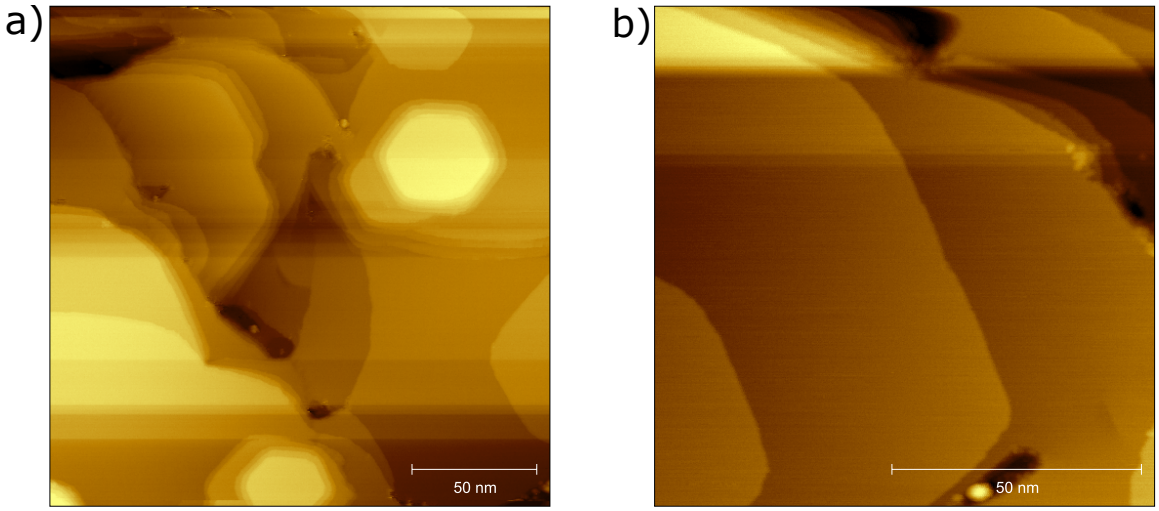

Figure 7.1: a) 200x200 nm and b) 100x100 nm topography scans of approximately 3 nm of silver deposited on Au(111) from Chapter 6. Scans were taken at 100 K using a W-tip with a bias of 1 V and a current setpoint of 0.35 nA.

A closer 5 x 5 nm window was scanned as shown in Fig. 7.2 using 1 V bias and 0.35 nA scanning parameters. There appears to be 'fuzzy', periodic objects across the scan window with some directionality. Although difficult to discern, an estimation was made on the diameter of the objects. The diameter of the objects are 2.7 $\pm$ 0.4 Å, agreeing with the metal diameter of silver at 2.88 Å.

The nearest neighbour distance between the atoms in the image is 0.24 $\pm$ 0.06 nm. Assuming a lattice constant of 0.408 nm for the FCC lattice of silver [97], the nearest neighbour distance expected is 0.29 nm for the (111) surface. The experimental results are within error of the theoretical value. However, the error is large due to the quality of the image. Changing the scanning parameters of the gain of the feedback loop could aid in the resolution of these features. Also, The diameter of gold and silver are approximately the same, meaning that the size of the atoms is not sufficient to determine the type of metal at the surface [98]. That said, given the long range

topography of the surface and the lack of a visible herringbone structure it safe to say that the surface under investigation is indeed silver.

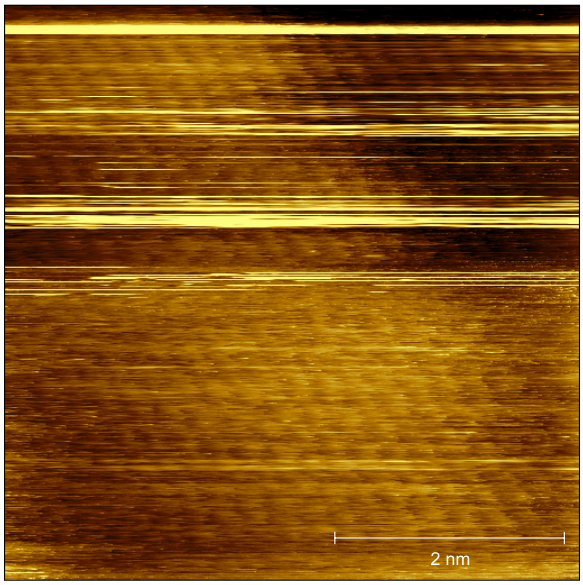

Figure 7.2: 5 x 5 nm topography scan of the Ag(111) surface deposited on Au(111) with scanning parameters of 1 V bias and 0.35 nA current setpoint. Streaks in the image are due to tip changes while scanning.

7.3 Dependence of the Apparent Barrier Height with Bias Voltage and Current Setpoint

The current setpoint of the STM system will set the tip-sample distance, and from Eq. 2.21 the apparent barrier height (ABH) is affected by the bias voltage. Given the equation assumes a very low bias, an assumption can be made that at higher biases the value of the ABH will lower due to the contribution of the voltage bias.

Fig. 7.3 a) shows the ABH of the silver surface at different biases using a constant current setpoint of 50 pA. The ABH value for tends to increase until a bias voltage of 0.6 V, then decreases. A jump in the value occurs at 3 V bias, then the ABH value decreases once more. Fig. 7.3 b) shows the ABH on the silver surface over changing current setpoints with a constant voltage bias of 1 V. The trend is linear about 4 eV. For each measurement, five I-z curves were averaged and the ABH was

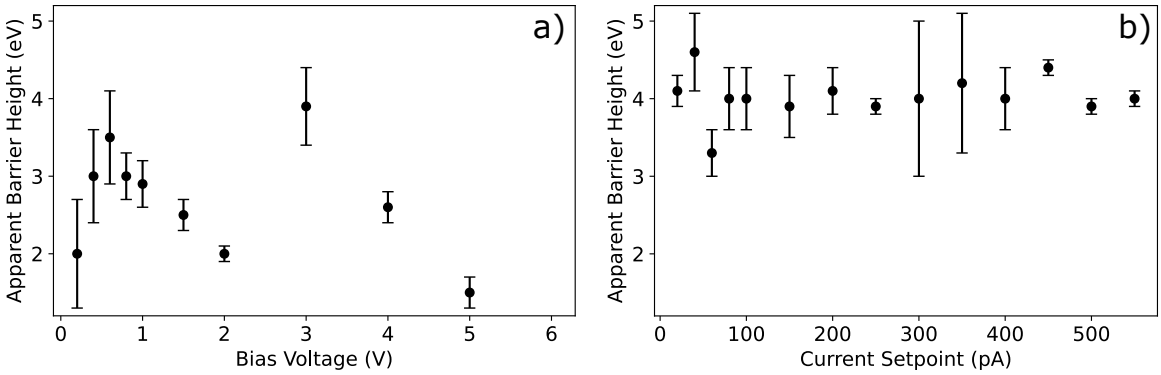

Figure 7.3: Apparent barrier height measurements of the silver surface using a tungsten tip and calculated using Eq. 2.21. a) The apparent barrier heights measured with a constant setpoint of 50 pA over different biases. b) The apparent barrier heights measured with a constant voltage bias of 1 V over different current setpoints.

calculated from that averaged slope. This was done three times per setpoint and voltage. The three values of the ABHs were averaged, and the error bars signify the range of the three values measured. The error bars for the small voltage biases are large, signifying a range of values for the ABH. The measurements for the constant setpoint were more consistent save for the values at 300 pA and 400 pA.

Fojtík et. al. observed the same downward trend for the ABH for a bias range of 1 to 2.5 V attributing the increase of the distance between the Fermi level of the tip to that of the sample, tilting the barrier such that the average height of the barrier is smaller (see chapter 2 for more information) [99]. However, the actual values of the ABH between their experiment and those of this study are different. This is likely due to the setpoint used here of 50 pA while the setpoint in the mentioned experiment is 3 nA. The jump of the value of the apparent barrier height at 3 V could be attributed to a change in the tip shape due to a possible tip-surface crash. From Luo et.al. it is expected that for a metal-metal tunneling process the apparent barrier height continuously decreases at increasing biases due to the increase of the tunneling probability for biases close to the workfunction of the sample [40]. Also expected would be a decreasing barrier height as the tip approaches the sample due to the image potential (see section 2.3). This downward trend does appear in the

ABH values from 0.6 V bias to 0 V bias.

The apparent barrier height value of 4.0 ± 0.5 eV from Fig. 7.3 b) agrees well with 3.8 eV from previous experiments [100]. Interestingly, the average barrier height does not quite coincide with the value of the apparent barrier height at 1 V for a setpoint of 50 pA from Fig. 7.3 a). This could be due to the mentioned tip changes discussed above since the I-z curve and apparent barrier height values are also dependent on the tip shape. If the surface of the tip significantly changes between the measurements such as a bend due to contact with the sample surface, the measured tunneling current may also differ. Other factors include piezo drift from the system and thermal drifts from STM tip operation. Also, a rapid scanning time between individual scans could also affect the ability of the tip to return to the same initial relative distance than previous scans. Having a longer wait time between measurements and ensuring the temperature

7.4 Optical-Pump/THz-STM-Probe of Ag Deposited on Au(111)

An aspect of the THz-STM is the ability to do optical-pump/THz-STM-probe measurements on the surface of a material. While the THz pulse is coupled to the tip of the STM system, a separate optical femtosecond pulse can be used to photoexcite carriers on the sample surface. This increases the number of carriers available to tunnel, increasing the current between the sample and tip, and can be measured the same way as a typical STM scan. This can be done in the tunneling regime where the tip is in tunneling range of the sample surface. It is important that the pump power is small so that the feedback loop does not raise the tip out of the tunneling regime due to the increased current from excited carriers. Fig. 7.4 a) shows the electro-optically sampled (EOS) waveform as per section 3.2. The negative polarization of the THz pulse is denoted by the absolute maximum of the electric field in the negative. Fig. 7.4 b) shows the optical-pump/THz-STM-probe waveform measurements with a tungsten

tip in the tunneling regime on the silver surface at increasing negative THz electric fields. The tip bias was set to -0.8 V to maximize the THz current based on the I-V curve taken at the junction, and the current setpoint was set to 20 pA. This setpoint allows for a safe tip-sample distance during the scans. The pump pulse was centered at 800 nm with a fluence set to 33 nJ. A line was drawn at the 0 ps time delay for comparison with the positive peak of the electro-optically sampled waveform. Each waveform is obtained through averaging five measurements.

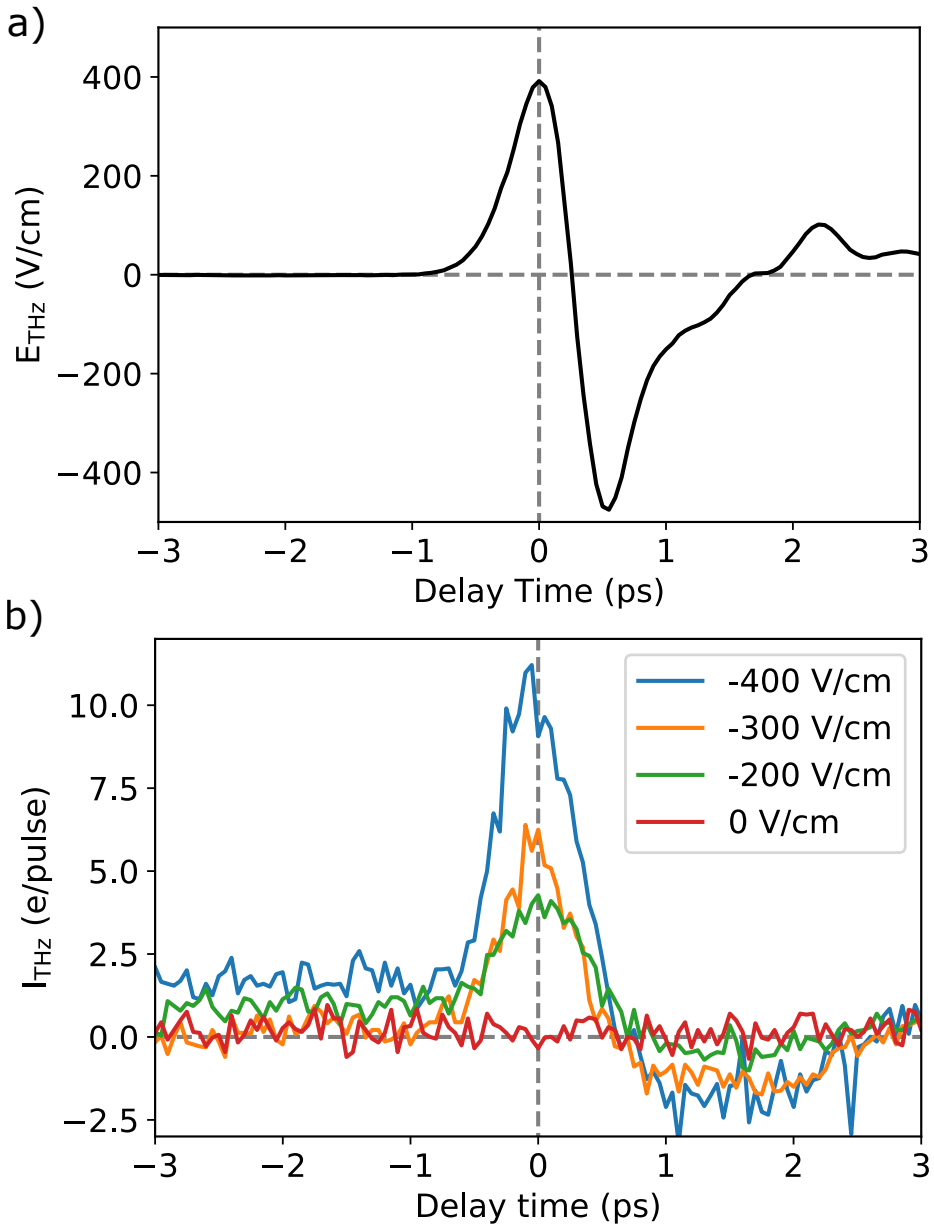

Figure 7.4: Optical-pump/THz-STM-probe measurements taken on the Ag surface using a tungsten tip at 100 K. a) The electro-optically sampled waveform with negative polarization. b) The optical-pump/THz-STM-probe results at varying THz electric fields at the peak. The two grey lines denote the average positive current peak position set to zero time delay to align with the EOS pulse.

The waveforms have a relatively similar shape to the electro-optically sampled waveform. The onset of the positive peak begins at -0.7 ps for all waveforms. The peak appears to center at about 0 ps, then decreases until 0.7 ps, much later than the EOS waveform. This broadening of the peak is due to a convolution of the optical and

THz waveforms in the tip-sample junction. These changes from the EOS waveform demonstrate a different dynamics arising from the excitation of the surface. However, it is difficult to determine the exact phenomena.

Possible explanations could be the antenna coupling of the THz to the tip, the shape of the tip, photoexcited carriers, or hot electron effects. Also, the tip could be outside the tunneling regime due to the current from the pump. In future work, to determine if the tip is within the tunneling regime, an I-z curve can be taken. If the current significantly changes while the tip is retracted, then the tip is in the tunneling regime. If the current does not change with changing tip height, the tip is outside the tunneling regime. A signal in the tunneling regime would allow for optical-pump/THz-STM-probe scans.

7.5 Optical-Pump/THz-Probe with Photoemitted Carriers and Different Pump Beam Placements

Optical-pump/THz-probe experiments were also performed on both the silver deposited on gold and a new gold sample prepared using the same methods as outlined in chapter 6. The measurements done for these experiments were performed with the tip retracted approximately 100 nm away from the sample surface. This ensures no tunneling is occurring between the tip and sample under normal operating conditions. For the following results, all experiments were performed with a THz electric field of -600 V/cm at a sample temperature of 100 K with a tungsten STM tip. The pump beam wavelength was centered at 800 nm with a 136 nJ pump fluence for the gold measurements and the silver measurements used a pump fluence of 112 nJ. Three waveforms were sampled and averaged for all data in this experiment.

Fig. 7.5 a) shows a schematic of the p-polarized pump beam locations during the experiments. The positions, tip size, THz pulse size, and positions relative to the tip are not to scale. The pump beam was moved in a line across the sample at approximately 0.2 - 0.4 mm intervals, with the tunneling junction centered across the

line. At each position, the pump beam was verified to not be incident onto the tip via reflections off the surface. The angle of incidence of the pump and THz beams are 40° and 35° with respect to the sample surface, respectively. The spot size of the pump beam is 0.2 mm in diameter.

Fig. 7.5 b) and c) are the THz-induced current at the tip-sample junction of the STM with pump beam illumination for the gold and silver samples, respectively. The zero lines are denoted by dashed lines to indicate the peak of the THz waveform. The peak current value from the silver sample is five times larger than that from the gold sample, indicating a stronger response from the surface. However, the form of each waveform are very similar to each other, with the reflection due to the tip at the same 14.5 ps mark. Given the THz electric fields at the peak were negative, a negative current at the peak could be expected for both samples. However, it appears that the strongest current value is positive.

Fig. 7.5 d) and e) are the THz-induced current for different pump positions. The dashed vertical line in the figures denote the 0 ps time delay relative to the 0 ps position of the tunneling waveforms from b) and c) for gold and silver, respectively. The current waveform at position 3 was normalized to unity given it had the largest current response, and the waveforms of the other positions were normalized to the position 3 maximum. This was done separately for the silver and gold samples. Although not indicated on the figures, the values for the current in the gold sample are still five times less than the currents for the silver sample. The waveforms of the two farthest pump beam configurations on the gold sample are either too small to see through the noise floor or the signal is not strong enough to allow the THz waveform to be sampled at the junction. This is not the case for the silver sample, where small bumps in the waveform can be seen outside of the noise floor of the system. The first positive peak for each position in both experiments appear to shift relative to the 0 ps reference point from the photoemission waveform. Waveforms probed from pump beam positions 1 and 2 have a positive time delay relative to the peak at the

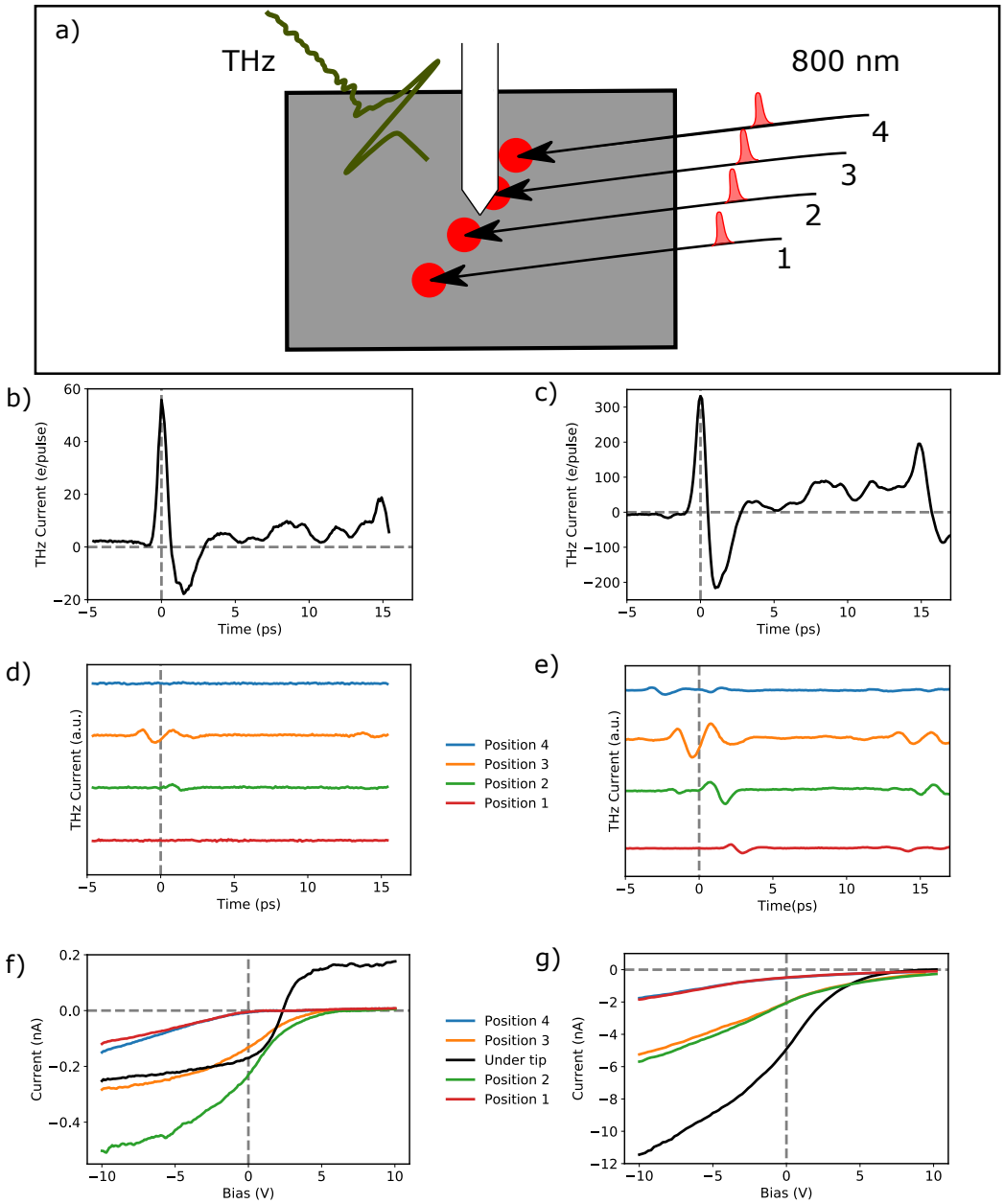

Figure 7.5: Photoemission-assisted measurements of the gold and silver surfaces at 100 K using a tungsten STM tip retracted 100 nm away from the sample surface using a p-polarized 800 nm laser pulse. a) A schematic of the locations of the pump beams relative to the tip-sample junction are numbered, while the THz pulse is always focused onto the tip-sample junction. b), c) Photoemission-assisted waveforms taken with the pump beam at the tip-sample junction of the gold and silver samples, respectively. d), e) THz waveforms probed at the tip-sample junction at different pump beam positions of gold and silver, respectively. The dashed lines indicate the zero time delay of the peak of the tunneling waveform. All currents were normalized with the same value, thus the amplitudes of the currents are relative. f), g) I-V curves taken with the THz focused onto the tip-sample junction with different pump beam positions of gold and silver, respectively.

tip-sample junction. Waveforms probed from pump beam position 3 and 4 have a negative time delay with respect to the waveform at the tip-sample junction. This is also seen with the reflection at 14.5 ps of the tip-sample waveform, although it is difficult to ascertain in many of the gold results and in the farther pump positions in the silver results. Finally, the general appearance of the waveforms change based on the location of the pump-beam. None of the waveforms appear to match in shape to the waveform from the tip-sample junction. It does appear in the silver sample that the peaks in the waveform from pump position 2 are getting repressed the further away the pump moves from the junction. The same observation is made with pump position 3 to pump position 4.

Although the current amplitudes from the silver sample are larger than that of the gold sample, the shape of the waveforms remain consistent with the pump position. The time delay of the positive peaks are also consistent with the pump position between samples. This is a good indication that the pump placement plays a role on the probed THz current. The time difference between the positive peak of the THz current while the pump is incident to the tip-sample junction and elsewhere may give some insight into the photoemission-assisted measurements. With a more precise method of measuring the distance from the tip to the pump beam, a speed may be calculated and compared to various phenomena such as surface plasmon polaritons. However, some of the probed peaks have a negative time difference when making this comparison. It would be expected that the farther distance travelled away from the tip, the longer time it would take to travel. This would give a positive time difference for every position. This might be explained by the tip being angled onto the sample, the sample itself not being flat in the STM system, and the onset beam length may also change based on changing the position from the onset mirror.

Fig. 7.5 f) and g) are the current-voltage responses of the system at varying pump positions relative to the tip-sample junction for the gold and silver sample, respectively. The I-V curve of the pump pulse in the tip-sample junction is also

shown. For each of the I-V curves, the THz pulse was incident onto the tunnel junction. The difference in the maximum currents at -10 V bias is more than ten times higher for the silver sample than the gold sample. The I-V curves for the pump beam at the furthest positions from the tip-sample junction for the gold sample trends to 0 nA at 0 V bias while the farthest pump positions do not cross the 0 nA line, instead trending towards 0 nA at high positive biases. The slopes of the I-V curves for similar and opposing pump distances relative to the tip-sample junction in the silver sample are consistent, while the slopes in the gold sample are mismatched. The I-V curves for the gold and silver samples in the tunnel junction have a similar current at the positive voltage bias. However, the shape of each is different. The stronger current response in the negative bias regime can be attributed to an influx of photoexcited electrons from the sample to the tip. As the sample bias moves towards the positive bias regime, the number of electrons flowing from the sample to the tip is reduced until there is no current flow. The positive current response in the tunneling regime for both the silver and gold samples show a flow of electrons from the tip to sample. This is attributed to the pump beam affecting carriers on the tungsten tip. The trend of the I-V curves in the negative bias regime coincides with the distance of the pump to the tip-sample junction, meaning the number of electrons from the sample to the tip diminishes the farther away the surface is pumped.

A final investigation on the sample surface is the polarity of the pump beam incident onto the surface at the same relative positions as outlined above. Fig. 7.6 shows the I-V curves similar to Fig. 7.5 f) and g) with an s-polarized pump beam instead of a p-polarized pump beam. The I-V curves follow the same trends for both p-polarized and s-polarized light albeit with a diminished current response for negative biases for s-polarized light. In both the silver and gold cases, it appears that current response from the s-polarized pump positioned under the tip is stronger in the positive bias regime, signalling s-polarized light couples to the tip better than p-polarized light. The results also show there is a pump polarity dependence for photoexcitation of

the surface carriers unto the tip and could signify multiple processes involved in the photoemission-assisted measurements on the surface.

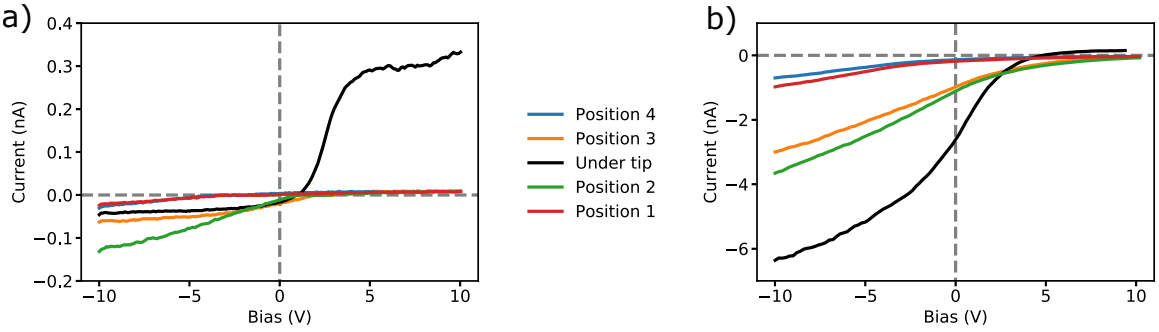

Figure 7.6: I-V curves of a) gold and b) silver samples taken with the same pump positions as outlined in Fig. 7.5 with an s-polarized 800 nm laser beam.

Experimental improvements can be made to further investigate the phenomena of the surface. Observing silver deposited on mica instead of on a gold substrate could prove useful for further comparisons. The pump beam spot size should also be considered given the approximate beam displacement on the sample surface. A smaller beam spot size would allow a more focused area to be illuminated and the beam edges to be properly moved away from the tip-sample junction to avoid any effects from the edges of the beam. A more mechanical method of moving the pump beam would assist in more accurate comparisons between samples. Finally, etching some reference lines onto the sample surface as a reference distance in order to calibrate the distance measurements from pump to the junction would assist in measuring the velocity of the carriers from the different tip distances to the tip.

Chapter 8

Conclusions

The work in this thesis used scanning tunneling microscopy, scanning tunneling spectroscopy, and THz-STM with the goal of observing the surfaces of superconductors and metals, measuring their THz dynamics, and examining the intriguing behaviour from photoemission-assisted measurements on metals. The first THz-STM scan of the surface of Bi-2212 is also presented, demonstrating the capability of THz-STM to possibly probe the superconducting dynamics of Bi-2212. The photoemission-assisted measurements may be an indication of a new way of measuring photon-induced surface dynamics of metals.

The topography and spectroscopy of Bi-2212 was observed using a UHV-STM system. The topography scans and atomic bond lengths were compared with literature, and coincided with previously published results. Conductance measurements appeared to match predicted results for the semiconducting and superconducting gaps of Bi-2212. However, the apparent barrier height measured did not match previous values, likely due to surface contaminants and an outgassing of the oxygen layer due to prolonged use in the UHV-STM system. Also, an attempt was made to perform a THz-STM scan on the surface. Although the THz-STM scan of the surface of Bi-2212 yielded no discernable results in the image, the non-zero THz current response from the onset of the THz electric field (I-E curve) is the first time THz-STM currents have been observed on a superconducting surface and allows hope for future experi-

mentation using THz-STM on the Bi-2212 sample. It would be interesting to further cleave the BiO layer to access the CuO_2 layer, to look at the contrast between the two layers in the THz-STM regime. Finally, it would be useful to take more I-V and I-z curves on the surface to have a better idea of the apparent barrier height, with and without the THz current.

STM topography and spectroscopy were also performed on a gold surface deposited onto mica. The herringbone reconstruction of the gold is visible, and the widths of the structures compared well to literature values. The change in the herringbone structure was also observed around surface defects. From the spectroscopy data, an apparent barrier height was measured and compared to previous results with a tungsten tip. Future experiments will include conductance measurements about the energy of the Shockley state of the surface. Conductance surface scans could also be completed about the surface, especially about surface defects and step edges, to characterize electron transport through the system. Further measurements of the apparent barrier height with respect to current biases with THz modulation could also give some insight into the tip height relationship.

Finally, silver deposited on a flat gold surface was also investigated. Atomic resolution was achieved on the silver sample, with good agreement with the expected diameter and lattice spacing. A study of the apparent barrier height with respect to changing voltage biases and current biases was also performed. The resulting trend of the voltage dependence agreed with literature values for a small range of voltages, but the values did not agree with other results on higher voltage biases. The barrier heights with varying current setpoints remained at a consistent value of 4 eV, matching previous literature values. A smaller tip-sample distance prior to the measurements could allow for a more consistent measurement.

Optical-pump/THz-STM-probe experiments were performed in both the tunneling regime for the silver sample and with the tip retracted outside the tunneling regime for silver and gold samples. The optical-pump/THz-probe results show the surface

response to the incoming THz waveform with respect to the surface. While the onset of the waveform matches well with the shape of the electro-optically sampled waveform, the pulse is widened and suppressed. The results from the optical pump-THz probe measurements where the tip is retracted away from the tunneling regime are interesting, and not yet well understood. Studying silver with no gold substrate, reducing the spot-size of the optical pump beam, and looking at different metal-on-metal configurations may give some insight into this observed behaviour.

References

[1] G. Fassin, "Something About the Early History of the Microscope," *The Scientific Monthly*, vol. 38, no. 5, pp. 452–459, 1934.

[2] E. Ruska, "The Development of the Electron Microscope and of Electron Microscopy (Nobel Lecture)," *Angewandte Chemie International Edition in English*, vol. 26, no. 7, pp. 595–605, 1987, ISSN: 15213773. DOI: 10.1002/anie.198705953.

[3] E. W. Müller, "Elektronenmikroskopische Beobachtungen von Feldkathoden [Electron microscopic observations of field cathodes]," *Zeitschrift für Physik*, vol. 106, no. 9-10, pp. 541–550, 1937, ISSN: 14346001. DOI: 10.1007/BF01339895.

[4] M Drechsler, "Erwin Müller and the early development of field emission microscopy," *Surface Science*, vol. 70, no. 1, pp. 1–18, 1978, ISSN: 00396028. DOI: 10.1016/0039-6028(78)90397-7. [Online]. Available: https://linkinghub.elsevier.com/retrieve/pii/0039602878903977.

[5] E. W. Müller, "Das Feldionenmikroskop [The Field Ion Microscope]," *Zeitschrift für Physik*, vol. 131, no. 1, pp. 136–142, 1951, ISSN: 1434-6001. DOI: 10.1007/BF01329651. [Online]. Available: http://link.springer.com/10.1007/BF01329651.

[6] E. A. Ash and G. Nicholls, "Super-resolution aperture scanning microscope," *Nature*, vol. 237, no. 5357, pp. 510–512, 1972, ISSN: 00280836. DOI: 10.1038/237510a0.

[7] G. Binnig and H. Rohrer, "Scanning Tunneling Microscopy," *Surface Science*, vol. 126, no. 1-3, pp. 236–244, 1983. DOI: 10.1016/0039-6028(83)90716-1.

[8] G. Binnig and H. Rohrer, "Scanning Tunneling Microscopy—from Birth to Adolescence," *Reviews of Modern Physics*, vol. 59, no. 3, pp. 615–625, 1987, ISSN: 15213773. DOI: 10.1103/RevModPhys.59.615.

[9] G Binnig, H Rohrer, C. Gerber, and E Weibel, "7 x 7 Reconstruction on Si(111) Resolved in Real Space," *Physical Review Letters*, vol. 50, no. 2, pp. 120–123, 1983.

[10] J. Gómez, L. Vázquez, A. M. Baró, C. Alonso, E. González, J. Gónzalez-Velasco, and A. J. Arvía, "Scanning tunneling microscopy (STM) and scanning electron microscopy (SEM) of electrodispersed gold electrodes," *Journal of Electroanalytical Chemistry*, vol. 240, no. 1-2, pp. 77–87, 1988, ISSN: 00220728. DOI: 10.1016/0022-0728(88)80314-0.

[11] H. Neddermeyer, "STM studies of nucleation and the initial stages of film growth," *Critical Reviews in Solid State and Materials Sciences*, vol. 16, no. 5, pp. 309–335, 1990, ISSN: 15476561. DOI: 10.1080/10408439008242185.

[12] O. M. Magnussen, "Atomic structure of ordered copper adlayers on single-crystalline gold electrodes," *Journal of Vacuum Science & Technology B: Microelectronics and Nanometer Structures*, vol. 9, no. 2, p. 969, 1991, ISSN: 0734211X. DOI: 10.1116/1.585505.

[13] K. Socha, "Tunneling spectroscopy of the (110) surface of direct-gap III-V semiconductors," *Physical Review B*, vol. 50, no. 7, pp. 4561–4570, 1994, ISSN: 00405116.

[14] B. Aufray, A. Kara, Ś. Vizzini, H. Oughaddou, C. Ĺandri, B. Ealet, and G. Le Lay, "Graphene-like silicon nanoribbons on Ag(110): A possible formation of silicene," *Applied Physics Letters*, vol. 96, no. 18, pp. 94–97, 2010, ISSN: 00036951. DOI: 10.1063/1.3419932.

[15] B. Voigtländer, *Fundamental processes in Si/Si and Ge/Si epitaxy studied by scanning tunneling microscopy during growth*, 5-8. 2001, vol. 43, pp. 127–254, ISBN: 4924616141. DOI: 10.1016/s0167-5729(01)00012-7.

[16] S. H. Pan, E. W. Hudson, K. M. Lang, H. Eisaki, S. Uchida, and J. C. Davis, "Imaging the effects of individual zinc impurity atoms on superconductivity in Bi2Sr2CaCu2O8+δ," *Nature*, vol. 403, no. 6771, pp. 746–750, 2000, ISSN: 0028-0836. DOI: 10.1038/35001534. [Online]. Available: http://www.nature.com/articles/35001534.

[17] Q.-Y. Wang, Z. Li, W.-H. Zhang, Z.-C. Zhang, J.-S. Zhang, W. Li, H. Ding, Y.-B. Ou, P. Deng, K. Chang, J. Wen, C.-L. Song, K. He, J.-F. Jia, S.-H. Ji, Y.-Y. Wang, L.-L. Wang, X. Chen, X.-C. Ma, and Q.-K. Xue, "Interface-Induced High-Temperature Superconductivity in Single Unit-Cell FeSe Films on SrTiO3," *Chinese Physics Letters*, vol. 29, no. 3, p. 037 402, 2012, ISSN: 0256-307X. DOI: 10.1088/0256-307X/29/3/037402. [Online]. Available: https://iopscience.iop.org/article/10.1088/0256-307X/29/3/037402.

[18] Ø. Fischer, M. Kugler, I. Maggio-Aprile, C. Berthod, and C. Renner, "Scanning tunneling spectroscopy of high-temperature superconductors," *Reviews of Modern Physics*, vol. 79, no. 1, pp. 353–419, 2007, ISSN: 00346861. DOI: 10.1103/RevModPhys.79.353. arXiv: 0610672 [cond-mat].

[19] S. M. Lindsay, T. Thundat, and L. Nagahara, "Adsorbate deformation as a contrast mechanism in STM images of biopolymers in an aqueous environment: images of the unstained, hydrated DNA double helix," *Journal of Microscopy*, vol. 152, no. 1, pp. 213–220, 1988, ISSN: 13652818. DOI: 10.1111/j.1365-2818.1988.tb01381.x.

[20] V. B. Pizziconi, D. L. Page, C. T. Connolly, and P. A. Diamond, "Scanning Probe Microscopy Imaging and Characterization of Biological Structures from Biomolecules to Living Cells," in *Atomic Force Microscopy/Scanning Tunneling Microscopy*, S. Cohen, M. Bray, and M. Lightbody, Eds., Boston, MA: Springer US, 1994. DOI: 10.1007/978-1-4757-9322-2_3.

[21] A. Ikai, "STM and AFM of bio/organic molecules and structures," *Surface Science Reports*, vol. 26, no. 8, pp. 261–332, 1996, ISSN: 0167-5729.

[22] G. F. van de Walle, H. van Kempen, P. Wyder, and P. Davidsson, "Scanning tunneling microscopy on photoconductive semi-insulating GaAs," *Applied Physics Letters*, vol. 50, no. 1, pp. 22–24, 1987, ISSN: 00036951. DOI: 10.1063/1.98125.

[23] S. Weiss, D. F. Ogletree, D. Botkin, M. Salmeron, and D. S. Chemla, "Ultrafast scanning probe microscopy," *Applied Physics Letters*, vol. 63, no. 18, pp. 2567–2569, 1993, ISSN: 0003-6951. DOI: 10.1063/1.110435. [Online]. Available: http://aip.scitation.org/doi/10.1063/1.110435.

[24] S. Grafström, P. Schuller, J. Kowalski, and R. Neumann, "Thermal expansion of scanning tunneling microscopy tips under laser illumination," *Journal of Applied Physics*, vol. 83, no. 7, pp. 3453–3460, 1998, ISSN: 00218979. DOI: 10.1063/1.366556.

[25] M. L. Cummings, T. Y. Chien, C. Preissner, V. Madhavan, D. Diesing, M. Bode, J. W. Freeland, and V. Rose, "Combining scanning tunneling microscopy and synchrotron radiation for high-resolution imaging and spectroscopy with chemical, electronic, and magnetic contrast," *Ultramicroscopy*, vol. 112, no. 1, pp. 22–31, 2012, ISSN: 18792723. DOI: 10.1016/j.ultramic.2011.09.018. [Online]. Available: http://dx.doi.org/10.1016/j.ultramic.2011.09.018.

[26] N. Shirato, M. Cummings, H. Kersell, Y. Li, B. Stripe, D. Rosenmann, S. W. Hla, and V. Rose, "Elemental fingerprinting of materials with sensitivity at the atomic limit," *Nano Letters*, vol. 14, no. 11, pp. 6499–6504, 2014, ISSN: 15306992. DOI: 10.1021/nl5030613.

[27] O. Takeuchi, M. Aoyama, R. Oshima, Y. Okada, H. Oigawa, N. Sano, H. Shigekawa, R. Morita, and M. Yamashita, "Probing subpicosecond dynamics using pulsed laser combined scanning tunneling microscopy," *Applied Physics Letters*, vol. 85, no. 15, pp. 3268–3270, 2004, ISSN: 00036951. DOI: 10.1063/1.1804238.

[28] J. B. Ballard, E. S. Carmichael, D. Shi, J. W. Lyding, and M. Gruebele, "Laser absorption scanning tunneling microscopy of carbon nanotubes," *Nano Letters*, vol. 6, no. 1, pp. 45–49, 2006, ISSN: 15306984. DOI: 10.1021/nl0519231.

[29] O. Takeuchi, R. Morita, M. Yamashita, and H. Shigekawa, "Development of time-resolved scanning tunneling microscopy in femtosecond range," *Japanese Journal of Applied Physics, Part 1: Regular Papers and Short Notes and Review Papers*, vol. 41, no. 7 B, pp. 4994–4997, 2002, ISSN: 00214922. DOI: 10.1143/jjap.41.4994.

[30] O. Takeuchi, S. Yoshida, and H. Shigekawa, "Light-modulated scanning tunneling spectroscopy for nanoscale imaging of surface photovoltage," *Applied Physics Letters*, vol. 84, no. 18, pp. 3645–3647, 2004, ISSN: 00036951. DOI: 10.1063/1.1737063.

[31] G. P. Donati, G. Rodriguez, and A. J. Taylor, "Ultrafast, dynamical imaging of surfaces by use of a scanning tunneling microscope with a photoexcited, low-temperature-grown GaAs tip," *Journal of the Optical Society of America B*, vol. 17, no. 6, p. 1077, 2000, ISSN: 0740-3224. DOI: 10.1364/josab.17.001077.

[32] G. N. Jr and M. R. Freeman, "Picosecond Resolution in Scanning Tunneling Microscopy Published by : American Association for the Advancement of Science Stable URL : https://www.jstor.org/stable/2883198 American Association for the Advancement of Science is collaborating with JSTOR to," vol. 262, no. 5136, pp. 1029–1032, 1993.

[33] G. M. Steeves, A. Y. Elezzabi, and M. R. Freeman, "Nanometer-scale imaging with an ultrafast scanning tunneling microscope," *Applied Physics Letters*, vol. 72, no. 4, pp. 504–506, 1998, ISSN: 00036951. DOI: 10.1063/1.120798.

[34] N. N. Khusnatdinov, T. J. Nagle, and G. Nunes, "Ultrafast scanning tunneling microscopy with 1 nm resolution," *Applied Physics Letters*, vol. 77, no. 26, pp. 4434–4436, 2000, ISSN: 00036951. DOI: 10.1063/1.1336817.

[35] T. L. Cocker, V. Jelic, M. Gupta, S. J. Molesky, J. A. Burgess, G. D. L. Reyes, L. V. Titova, Y. Y. Tsui, M. R. Freeman, and F. A. Hegmann, "An ultrafast terahertz scanning tunnelling microscope," *Nature Photonics*, vol. 7, no. 8, pp. 620–625, 2013, ISSN: 17494885. DOI: 10.1038/nphoton.2013.151.

[36] S. Yoshida, H. Hirori, T. Tachizaki, K. Yoshioka, Y. Arashida, Z. H. Wang, Y. Sanari, O. Takeuchi, Y. Kanemitsu, and H. Shigekawa, "Subcycle Transient Scanning Tunneling Spectroscopy with Visualization of Enhanced Terahertz Near Field," *ACS Photonics*, vol. 6, no. 6, pp. 1356–1364, 2019, ISSN: 23304022. DOI: 10.1021/acsphotonics.9b00266.

[37] M. Müller, N. Martín Sabanés, T. Kampfrath, and M. Wolf, "Phase-Resolved Detection of Ultrabroadband THz Pulses inside a Scanning Tunneling Microscope Junction," *ACS Photonics*, vol. 7, no. 8, pp. 2046–2055, 2020, ISSN: 23304022. DOI: 10.1021/acsphotonics.0c00386. arXiv: 2003.09214.

[38] V. Jelic, K. Iwaszczuk, P. H. Nguyen, C. Rathje, G. J. Hornig, H. M. Sharum, J. R. Hoffman, M. R. Freeman, and F. A. Hegmann, "Ultrafast terahertz control of extreme tunnel currents through single atoms on a silicon surface," *Nature Physics*, vol. 13, no. 6, pp. 591–597, 2017, ISSN: 17452481. DOI: 10.1038/nphys4047.

[39] S. Yoshida, Y. Arashida, H. Hirori, T. Tachizaki, A. Taninaka, H. Ueno, O. Takeuchi, and H. Shigekawa, "Terahertz Scanning Tunneling Microscopy for Visualizing Ultrafast Electron Motion in Nanoscale Potential Variations," *ACS Photonics*, vol. 8, no. 1, pp. 315–323, 2021, ISSN: 23304022. DOI: 10.1021/acsphotonics.0c01572.

[40] Y. Luo, V. Jelic, G. Chen, P. H. Nguyen, Y. J. R. Liu, J. A. Calzada, D. J. Mildenberger, and F. A. Hegmann, "Nanoscale terahertz STM imaging of a metal surface," *Physical Review B*, vol. 102, no. 20, p. 205 417, 2020, ISSN: 24699969. DOI: 10.1103/PhysRevB.102.205417. [Online]. Available: https://doi.org/10.1103/PhysRevB.102.205417.

[41] L. Wimmer, G. Herink, D. R. Solli, S. V. Yalunin, K. E. Echternkamp, and C. Ropers, "Terahertz control of nanotip photoemission," *Nature Physics*, vol. 10, no. 6, pp. 432–436, 2014, ISSN: 17452481. DOI: 10.1038/nphys2974.

[42] K. Wang, D. M. Mittleman, N. C. Van Der Valk, and P. C. Planken, "Antenna effects in terahertz apertureless near-field optical microscopy," *Applied Physics Letters*, vol. 85, no. 14, pp. 2715–2717, 2004, ISSN: 00036951. DOI: 10.1063/1.1797554.

[43] P. H. Nguyen, V. Jelic, Y. Luo, J. A. Calzada, Y. J. R. Liu, and F. A. Hegmann, "Modeling the Terahertz Pulse Induced Transient Bias in the STM Junction," *International Conference on Infrared, Millimeter, and Terahertz Waves, IRMMW-THz*, vol. 2020-Novem, pp. 94–95, 2020, ISSN: 21622035. DOI: 10.1109/IRMMW-THz46771.2020.9370659.

[44] B. Voigtländer, *Scanning Probe Microscopy*, ser. NanoScience and Technology. Berlin, Heidelberg: Springer Berlin Heidelberg, 2015, ISBN: 978-3-662-45239-4. DOI: 10.1007/978-3-662-45240-0. [Online]. Available: http://link.springer.com/10.1007/978-3-662-45240-0.

[45] J. G. Simmons, "Generalized Formula for the Electric Tunnel Effect between Similar Electrodes Separated by a Thin Insulating Film," *Journal of Applied Physics*, vol. 34, no. 6, pp. 1793–1803, 1963, ISSN: 00218979. DOI: 10.1063/1.1702682.

[46] J. G. Simmons, "Electric Tunnel Effect between Dissimilar Electrodes Separated by a Thin Insulating Film," *Journal of Applied Physics*, vol. 34, no. 9, pp. 2581–2590, 1963, ISSN: 00218979. DOI: 10.1063/1.1729774.

[47] J. Bardeen, "Tunneling from a many-particle point of view," *Physical Review*, vol. 6, no. 57, pp. 1083–1086, 1961, ISSN: 0031899X. DOI: 10.1103/PhysRevLett.6.57.

[48] J. Tersoff and D. R. Hamann, "Theory and Application for the Scanning Tunneling Microscope," *Physical Review Letters*, vol. 50, no. 25, pp. 1998–2001, 1983, ISSN: 0031-9007. DOI: 10.1103/PhysRevLett.50.1998. [Online]. Available: https://link.aps.org/doi/10.1103/PhysRevLett.50.1998.

[49] J. Tersoff and D. R. Hamann, "Theory of the scanning tunneling microscope," *Physical Review B*, vol. 31, no. 2, pp. 805–813, 1985, ISSN: 0163-1829. [Online]. Available: https://link.aps.org/doi/10.1103/PhysRevB.31.805.

[50] C. J. Chen, "Origin of atomic resolution on metal surfaces in scanning tunneling microscopy," *Physical Review Letters*, vol. 65, no. 4, pp. 448–451, 1990, ISSN: 0031-9007. DOI: 10.1103/PhysRevLett.65.448. [Online]. Available: https://link.aps.org/doi/10.1103/PhysRevLett.65.448.

[51] C. J. Chen, "Tunneling matrix elements in three-dimensional space: The derivative rule and the sum rule," *Physical Review B*, vol. 42, no. 14, pp. 8841–8857, 1990, ISSN: 01631829. DOI: 10.1103/PhysRevB.42.8841.

[52] M. B. Panish and H. C. Casey, "Temperature Dependence of the Energy Gap in GaAs and GaP," *Journal of Applied Physics*, vol. 40, no. 1, pp. 163–167, 1969, ISSN: 0021-8979. DOI: 10.1063/1.1657024. [Online]. Available: https://onlinelibrary.wiley.com/doi/10.1002/pssa.2210080244http://aip.scitation.org/doi/10.1063/1.1657024https://www.osapublishing.org/abstract.cfm?URI=ao-42-9-1726.

[53] F. G. Sun, G. A. Wagoner, and X. C. Zhang, "Measurement of free-space terahertz pulses via long-lifetime photoconductors," *Applied Physics Letters*, vol. 67, no. July, p. 1656, 1995, ISSN: 00036951. DOI: 10.1063/1.115047.

[54] X. Zheng, Y. Xu, R. Sobolewski, R. Adam, M. Mikulics, M. Siegel, and P. Kordoš, "Femtosecond response of a free-standing LT-GaAs photoconductive switch," *Applied Optics*, vol. 42, no. 9, p. 1726, 2003, ISSN: 0003-6935. DOI: 10.1364/ao.42.001726.

[55] K. Wang and D. M. Mittleman, "Metal wires for terahertz wave guiding," *Nature*, vol. 432, no. 7015, pp. 376–379, 2004, ISSN: 0028-0836. DOI: 10.1038/nature03040. [Online]. Available: http://www.nature.com/articles/nature03040.

[56] M. Walther, G. S. Chambers, Z. Liu, M. R. Freeman, and F. A. Hegmann, "Emission and detection of terahertz pulses from a metal-tip antenna," *Journal of the Optical Society of America B*, vol. 22, no. 11, p. 2357, 2005, ISSN: 0740-3224. DOI: 10.1364/josab.22.002357.

[57] A. J. Adam, N. C. van der Valk, and P. C. Planken, "Measurement and calculation of the near field of a terahertz apertureless scanning optical microscope," *Journal of the Optical Society of America B*, vol. 24, no. 5, p. 1080, 2007, ISSN: 0740-3224. DOI: 10.1364/JOSAB.24.001080. [Online]. Available: https://www.osapublishing.org/abstract.cfm?URI=josab-24-5-1080.

[58] D. A. Yarotski, R. D. Averitt, N. Negre, S. A. Crooker, A. J. Taylor, G. P. Donati, A. Stintz, L. F. Lester, and K. J. Malloy, "Ultrafast carrier-relaxation dynamics in self-assembled InAs/GaAs quantum dots," *Journal of the Optical Society of America B*, vol. 19, no. 6, p. 1480, 2002, ISSN: 0740-3224. DOI: 10.1364/JOSAB.19.001480. [Online]. Available: https://www.osapublishing.org/abstract.cfm?URI=josab-19-6-1480.

[59] T. L. Cocker, D. Peller, P. Yu, J. Repp, and R. Huber, "Tracking the ultrafast motion of a single molecule by femtosecond orbital imaging," *Nature*, vol. 539, no. 7628, pp. 263–267, 2016, ISSN: 14764687. DOI: 10.1038/nature19816. [Online]. Available: http://dx.doi.org/10.1038/nature19816.

[60] B. Ren, G. Picardi, and B. Pettinger, "Preparation of gold tips suitable for tip-enhanced Raman spectroscopy and light emission by electrochemical etching," *Review of Scientific Instruments*, vol. 75, no. 4, pp. 837–841, 2004, ISSN: 00346748. DOI: 10.1063/1.1688442.

[61] J. K. Schoelz, P. Xu, S. D. Barber, D. Qi, M. L. Ackerman, G. Basnet, C. T. Cook, and P. M. Thibado, "High-percentage success method for preparing and pre-evaluating tungsten tips for atomic-resolution scanning tunneling microscopy," *Journal of Vacuum Science & Technology B, Nanotechnology and Microelectronics: Materials, Processing, Measurement, and Phenomena*, vol. 30, no. 3, p. 033 201, 2012, ISSN: 2166-2746. DOI: 10.1116/1.3701977.

[62] T. K. Yamada, T. Abe, N. M. Nazriq, and T. Irisawa, "Electron-bombarded 110-oriented tungsten tips for stable tunneling electron emission," *Review of Scientific Instruments*, vol. 87, no. 3, pp. 1–8, 2016, ISSN: 10897623. DOI: 10.1063/1.4943074. [Online]. Available: http://dx.doi.org/10.1063/1.4943074.

[63] J. G. Bednorz and K. A. Müller, "Possible highT c superconductivity in the Ba-La-Cu-O system," *Zeitschrift für Physik B Condensed Matter*, vol. 64, no. 2, pp. 189–193, 1986, ISSN: 0722-3277. DOI: 10.1007/BF01303701. [Online]. Available: http://link.springer.com/10.1007/BF01303701.

[64] J. C. Phillips, "Structural chemistry and high-temperature superconductivity," *Physical Review B*, vol. 36, no. 1, pp. 861–863, 1987, ISSN: 0163-1829. DOI: 10.1103/PhysRevB.36.861. [Online]. Available: https://link.aps.org/doi/10.1103/PhysRevB.36.861.

[65] C. Michel, M. Hervieu, M. M. Borel, A. Grandin, F. Deslandes, J. Provost, and B. Raveau, "Superconductivity in the Bi - Sr - Cu - O system," *Zeitschrift für Physik B Condensed Matter*, vol. 68, no. 4, pp. 421–423, 1987, ISSN: 07223277. DOI: 10.1007/BF01471071.

[66] J. L. Tallon, R. G. Buckley, P. W. Gilberd, M. R. Presland, I. W. M. Brown, M. E. Bowden, L. A. Christian, and R. Goguel, "High-Tc superconducting phases in the series Bi2.1(Ca,Sr)n+1CunO2n+4+δ," *Nature*, vol. 333, pp. 153–156, 1988.

[67] H. Maeda, Y. Tanaka, M. Fukutomi, and T. Asano, "A New High-Tc Oxide Superconductor without a Rare Earth Element," *Japanese Journal of Applied Physics*, vol. 27, p. L209, 1988, ISSN: 0021-4922. DOI: 10.1007/978-94-011-1622-0_42.

[68] B. Susłla, R. Czajka, W. Gordon, S. Szuba, and J. Raułluszkiewicz, "AFM and STM investigations of a Bi2Sr2CaCu2O8 high-Tc superconductor," *Materials Science and Engineering: A*, vol. 217-218, no. 96, pp. 419–423, 1996, ISSN: 09215093. DOI: 10.1016/S0921-5093(96)10351-8. [Online]. Available: https://linkinghub.elsevier.com/retrieve/pii/S0921509396103518.

[69] S. Sugita, T. Watanabe, and A. Matsuda, "Atomic image of a CuO2 plane in the STM image of a Bi2Sr2CaCu2O8+δ cleaved surface," *Physical Review B - Condensed Matter and Materials Physics*, vol. 62, no. 13, pp. 8715–8718, 2000, ISSN: 01631829. DOI: 10.1103/PhysRevB.62.8715.

[70] M. Tanaka, T. Takahashi, H. Katayama-Yoshida, S. Yamazaki, M. Fujinami, Y. Okabe, W. Mizutani, M. Ono, and K. Kajimura, "Evidence for non-metallic nature of the BiO plane in Bi 2 Ca Sr 2 Cu 2 O 8 from scanning tunnelling spectroscopy," *Nature*, vol. 339, pp. 691–693, 1989. DOI: 10.1038/339691a0.

[71] M. Tanaka, S. Yamazaki, M. Fujinami, T. Takahashi, H. Katayama-Yoshida, W. Mizutani, K. Kajimura, and M. Ono, "Surface electronic properties on BiO plane of Bi 2 Sr 2 CaCu 2 O 8 single crystal measured by scanning tunneling microscopy," *Journal of Vacuum Science & Technology A: Vacuum, Surfaces, and Films*, vol. 8, no. 1, pp. 475–478, 1990, ISSN: 0734-2101. DOI: 10.1116/1.577022.

[72] C. K. Shih, R. M. Feenstra, and G. V. Chandrashekhar, "Scanning tunneling microscopy and spectroscopy of Bi-Sr-Ca-Cu-O 2:2:1:2 high-temperature superconductors," *Physical Review B*, vol. 43, no. 10, pp. 7913–7922, 1991, ISSN: 01631829. DOI: 10.1103/PhysRevB.43.7913.

[73] K. Momma and F. Izumi, "VESTA 3 for three-dimensional visualization of crystal, volumetric and morphology data," *Journal of Applied Crystallography*, vol. 44, pp. 1272–1276, 2011.

[74] R. Wesche, *Physical Properties of High-Temperature Superconductors*. West Sussex: John Wiley & Sons, Ltd, 2015, p. 528, ISBN: 9781119978817.

[75] C. Renner and O. Fischer, "Vacuum tunneling spectroscopy and asymmetric density of states of Bi2Sr2CaCu2O8+δ," *Physical Review B*, vol. 51, no. 14, pp. 9208–9218, 1995, ISSN: 0163-1829. DOI: 10.1103/PhysRevB.51.9208. [Online]. Available: https://link.aps.org/doi/10.1103/PhysRevB.51.9208.

[76] D. L. Feng, D. H. Lu, K. M. Shen, C. Kim, H. Eisaki, A. Damascelli, R. Yoshizaki, J. I. Shimoyama, K. Kishio, G. D. Gu, S. Oh, A. Andrus, J. O'Donnell, J. N. Eckstein, and Z. X. Shen, "Signature of superfluid density in the single-particle excitation spectrum of Bi2Sr2CaCu2O(8+δ)," *Science*, vol. 289, no. 5477, pp. 277–281, 2000, ISSN: 00368075. DOI: 10.1126/science.289.5477.277.

[77] S. Misra, S. Oh, D. J. Hornbaker, T. DiLuccio, J. N. Eckstein, and A. Yazdani, "Atomic Scale Imaging and Spectroscopy of a CuO2 Plane at the Surface of Bi2Sr2CaCu2O8+δ," *Physical Review Letters*, vol. 89, no. 8, pp. 2–5, 2002, ISSN: 10797114. DOI: 10.1103/PhysRevLett.89.087002.

[78] M. D. Kirk, J. Nogami, A. A. Baski, D. B. Mitzi, A. Kapitulnik, T. H. Geballe, and C. F. Quate, "The origin of the superstructure in Bi2Sr2CaCu 2O8+δ as revealed by scanning tunneling microscopy," *Science*, vol. 242, no. 4886, pp. 1673–1675, 1988, ISSN: 00368075. DOI: 10.1126/science.242.4886.1673.

[79] C. K. Shih, R. M. Feenstra, J. R. Kirtley, and G. V. Chandrashekhar, "Surface structural and electronic properties of cleaved single crystals of $Bi_{2.15}Sr_{1.7}CaCu_2O_{8+\gamma}$ compounds: A scanning tunneling microscopy study," *Physical Review B*, vol. 40, no. 4, pp. 2682–2685, 1989, ISSN: 0163-1829. DOI: 10.1103/PhysRevB.40.2682. [Online]. Available: https://link.aps.org/doi/10.1103/PhysRevB.40.2682.

[80] C. Renner, B. Revaz, K. Kadowaki, I. Maggio-Aprile, and Fischer, "Observation of the low temperature pseudogap in the vortex cores of Bi2Sr2CaCu2O8+δ," *Physical Review Letters*, vol. 80, no. 16, pp. 3606–3609, 1998, ISSN: 10797114. DOI: 10.1103/PhysRevLett.80.3606.

[81] A. Sugimoto, T. Ekino, and H. Eisaki, "Nanoscale modulation of local barrier height on Bi-based cuprate superconductors observed by scanning tunneling microscopy/spectroscopy," *Journal of the Physical Society of Japan*, vol. 77, no. 4, pp. 2–5, 2008, ISSN: 00319015. DOI: 10.1143/JPSJ.77.043705.

[82] Y. F. Lv, W. L. Wang, J. P. Peng, H. Ding, Y. Wang, L. Wang, K. He, S. H. Ji, R. Zhong, J. Schneeloch, G. D. Gu, C. L. Song, X. C. Ma, and Q. K. Xue, "Mapping the Electronic Structure of Each Ingredient Oxide Layer of High-Tc Cuprate Superconductor Bi2Sr2CaCu2 O8+δ," *Physical Review Letters*, vol. 115, no. 23, pp. 1–5, 2015, ISSN: 10797114. DOI: 10.1103/PhysRevLett.115.237002.

[83] D. W. Pashley, M. J. Stowell, and T. J. Law, "The Crystal Structure of Evaporated Gold Films," *Physica Status Solidi (B)*, vol. 10, no. 1, pp. 153–163, 1965, ISSN: 15213951. DOI: 10.1002/pssb.19650100115.

[84] B. Yan, B. Stadtmüller, N. Haag, S. Jakobs, J. Seidel, D. Jungkenn, S. Mathias, M. Cinchetti, M. Aeschlimann, and C. Felser, "Topological states on the gold surface," *Nature Communications*, vol. 6, no. 1, p. 10 167, 2015, ISSN: 2041-1723. DOI: 10.1038/ncomms10167. arXiv: 1504.01971. [Online]. Available: http://www.nature.com/articles/ncomms10167.

[85] V. M. Hallmark, S. Chiang, J. F. Rabolt, J. D. Swalen, and R. J. Wilson, "Observation of atomic corrugation on Au(111) by scanning tunneling microscopy," *Physical Review Letters*, vol. 59, no. 25, pp. 2879–2882, 1987, ISSN: 00319007. DOI: 10.1103/PhysRevLett.59.2879.

[86] J. Inukai, W. Mizutani, K. Saito, H. Shimizu, and Y. Iwasawa, "Gold substrates for scanning tunneling microscopy of adsorbed species," *Japanese Journal of Applied Physics*, vol. 30, no. 12 R, pp. 3496–3502, 1991, ISSN: 13474065. DOI: 10.1143/JJAP.30.3496.

[87] R. Wiesendanger, *Scanning Probe Microscopy and Spectroscopy*. Cambridge, UK: Cambridge University Press, 1994, pp. 358–362.

[88] J. V. Barth, R. J. Behm, H. Brune, and G. Ertl, "Scanning tunneling microscopy observations on the reconstructed Au(111) surface: Atomic structure, long-range superstructure, rotational domains, and surface defects," *Physical Review B*, vol. 42, no. 15, pp. 9307–9318, 1990, ISSN: 01631829. [Online]. Available: https://journals.aps.org/prb/pdf/10.1103/PhysRevB.42.9307.

[89] C. Wöll, S. Chiang, R. J. Wilson, and P. H. Lippel, "Determination of atom positions at stacking-fault dislocations on Au(111) by scanning tunneling microscopy," *Physical Review B*, vol. 39, no. 11, pp. 7988–7991, 1989. DOI: 10.1007/978-94-011-1812-5_15.

[90] F. Hanke and J. Björk, "Structure and local reactivity of the Au(111) surface reconstruction," *Physical Review B - Condensed Matter and Materials Physics*, vol. 87, no. 23, pp. 1–6, 2013, ISSN: 10980121. DOI: 10.1103/PhysRevB.87.235422.

[91] H. Bulou and C. Goyhenex, "Local strain analysis of the herringbone reconstruction of Au(111) through atomistic simulations," *Physical Review B - Condensed Matter and Materials Physics*, vol. 65, no. 4, pp. 1–10, 2002, ISSN: 1550235X. DOI: 10.1103/PhysRevB.65.045407.

[92] Y. Hasegawa and P. Avouris, "Manipulation of the reconstruction of the Au(111) surface with the STM," *Science*, vol. 258, no. 5089, pp. 1763–1765, 1993, ISSN: 00368075. DOI: 10.1126/science.258.5089.1763.

[93] L. C. Davis, M. P. Everson, R. C. Jaklevic, and W. Shen, "Theory of the local density of surface states on a metal: Comparison with scanning tunneling spectroscopy of a Au(111) surface," *Physical Review B*, vol. 43, no. 5, pp. 3821–3830, 1991, ISSN: 0163-1829. DOI: 10.1103/PhysRevB.43.3821. [Online]. Available: https://link.aps.org/doi/10.1103/PhysRevB.43.3821.

[94] M. P. Everson, R. C. Jaklevic, and W. Shen, "Measurement of the local density of states on a metal surface: Scanning tunneling spectroscopic imaging of Au(111)," *Journal of Vacuum Science & Technology A: Vacuum, Surfaces, and Films*, vol. 8, no. 5, pp. 3662–3665, 1990, ISSN: 0734-2101. DOI: 10.1116/1.576476.

[95] S. Kurokawa, Y. Yamashita, A. Sakai, and Y. Hasegawa, "Scanning tunneling microscopy barrier-height imaging of Shockley dislocations on a Au(111) reconstructed surface," *Japanese Journal of Applied Physics, Part 1: Regular Papers and Short Notes and Review Papers*, vol. 40, no. 6 B, pp. 4277–4280, 2001, ISSN: 00214922. DOI: 10.1143/jjap.40.4277.

[96] W Mizutani, T Ishida, N Choi, T Uchihashi, and H Tokumoto, "Electric-dipole layer on Au(111) surfaces," *Applied Physics A Materials Science & Processing*, vol. 72, no. S2, S181–S184, 2001, ISSN: 0947-8396. DOI: 10.1007/s003390100675. [Online]. Available: http://link.springer.com/10.1007/s003390100675.

[97] W. P. Davey, "Precision measurements of the lattice constants of twelve common metals," *Physical Review*, vol. 25, no. 6, pp. 753–761, 1925, ISSN: 0031899X. DOI: 10.1103/PhysRev.25.753.

[98] D. L. Fay, "Copper, Silver and Gold," in *Chemistry of the Elements*, Elsevier, 1997, pp. 1173–1200. DOI: 10.1016/B978-0-7506-3365-9.50034-1. [Online]. Available: https://linkinghub.elsevier.com/retrieve/pii/B9780750633659500341.

[99] P. Fojtík, K. Perronet, I. Pelant, J. Chval, and F. Charra, "Photon emission from polycrystalline Ag induced by scanning tunneling microscopy: comparison of different tip materials," *Surface Science*, vol. 531, no. 2, pp. 113–122, 2003, ISSN: 00396028. DOI: 10.1016/S0039-6028(03)00510-7. [Online]. Available: https://linkinghub.elsevier.com/retrieve/pii/S0039602803005107.

[100] R. Berndt, J. K. Gimzewski, and P. Johansson, "Electromagnetic interactions of metallic objects in nanometer proximity," *Physical Review Letters*, vol. 71, no. 21, pp. 3493–3496, 1993, ISSN: 0031-9007. DOI: 10.1103/PhysRevLett.71.3493. [Online]. Available: https://link.aps.org/doi/10.1103/PhysRevLett.71.3493.